On the evolution of
massive close binary systems

Front cover: Belgrade (Serbia), designed by J.M.Krijger

On the evolution of massive close binary systems

Over de evolutie van massieve dichte dubbelster systemen

(met een samenvatting in het Nederlands)

PROEFSCHRIFT

DOOR

Jelena Petrović

geboren op 24 maart 1974, te Priština, Servië & Montenegro

Contents

4 The impact of radiation and wind momenta on mass transfer in massive close binary systems   **69**

authors: Luc Dessart, Norbert Langer, Jelena Petrovic; published in A&A

5 Which Massive stars are Gamma-Ray Burst Progenitors?   **81**

authors: Jelena Petrovic, Norbert Langer, Sung-Chul Yoon, Alexander Heger ; Submitted to A&A

6 Masivne zvezde u bliskim dvojnim sistemima   **115**

7 Over de evolutie van massieve dichte dubbelster systemen   **119**

Chapter 1

Introduction

1.1 Introduction

Stars begin their life by condensing out of a dense cloud of interstellar medium. As the cloud collapses under the force of gravity the matter becomes hotter. If the initial mass is larger than about 0.1 Solar masses (further $M_\odot$), the core temperature will rise to about $10^7 K$ and nuclear reactions will start, converting hydrogen into helium. This phase of every star's life is called main sequence evolution. Depending on the initial mass, stars have different properties during their main sequence. Main sequence stars like our Sun are yellow, moderately warm with surface temperature of ~6000 K and they live 10 billions of years. Stars less massive than the Sun are cool, red and live even longer, while more massive stars are blue, warm and can end their lives in only few million years. Depending on their temperature and brightness (luminosity), stars on the main sequence are classified in spectral classes: O, B, A, F, G, K and M. O stars are the most massive, blue and hot stars (surface temperature >25000 K) and M stars are the least massive, cold (surface temperature <3500 K) and red stars.

After core hydrogen burning is finished, the star starts contracting since there is no force to balance gravity. Due to this, the temperature in the outer layers increases enough to ignite hydrogen and the stellar envelope starts expanding. On the other side, the stellar core is contracting further and when temperature reaches ~$10^8 K$, core helium burning starts. This phase of stellar evolution is called red giant (for less massive stars) or red supergiant (for more massive stars).

Depending on their initial mass, stars will end their lives in different ways. Stars with low initial masses (less than 8 $M_\odot$) can not reach high enough temperatures in the core to ignite carbon, so their core contracts after helium core burning into a small compact star called a white dwarf, while its outer layers are shattered as a planetary nebula.

More massive stars undergo all nuclear burning stages up to a formation of an iron-nickel core. They can evolve through the phase of Wolf-Rayet star (further WR). WR stars have an extremely hot surface ($T > 50000K$), very high luminosity ($L \sim 10^{5-6}$ Solar luminosities, further $L_\odot$), high mass loss rate ($\dot{M} \sim 10^{-4-5} M_\odot yr^{-1}$) and have lost most of their hydrogen rich envelope. After all of the helium in the core is consumed, carbon and oxygen ignite. Their burning yields such products as neon, magnesium, silicon, and sulfur. Eventually, silicon and sulfur ignite in the star's core

to form an iron-nickel core. While fusion of elements lighter than iron releases energy, iron fusion consumes energy. There is no force anymore to balance gravity and the stellar core collapses. Depending on the mass of a core, it collapses into a neutron star (core masses smaller than 2.5 $M_\odot$) or a black hole. At the same time, the layers outside of the core are ejected in a supernova (SN) explosion. Since nuclear fusion reactions that make elements heavier than iron require more energy than they give off, such reactions do not occur in stellar cores, but only in supernovae explosions. In addition to making elements, supernovae scatter the elements (made by both the star and supernova) out into the interstellar medium. These are the elements that make up stars, planets and everything on Earth – including ourselves.

Supernova explosions of massive fast rotating stars might be connected with gamma-ray burst events. Gamma ray bursts (GRBs) are flashes of gamma-ray photons (energy $E > 10^5$eV), that appear all over the sky several times per day at very large distances from Earth. Gamma ray bursts release extremely large amount of energy, approximatelly 10^{52}-10^{53}erg. This is the amount of energy released by 1000 stars like Sun over their entire lifetime.

The evolution of a star in a binary system can differ significantly from a single isolated one with the same mass and chemical composition. The physical processes that enter binary evolution are the modified gravitational and radiation field from the companion, as well as the centrifugal force contribution arising from the rotation of the system. But, most important, it is the evolution of the more massive component that will influence dramatically the evolution of the system. Indeed, in certain evolutionary phases, mass transfer from one star (the primary, mass donor) to the other (the secondary, mass accretor) can occur, changing present properties like the luminosity, radius, effective temperature, abundances etc. of both stars, as well as their future evolution. Close binary system that consist initially of two massive O stars eventually enters mass transfer. During this process mass donor will lose a significant amount of hydrogen from its envelope and this system will evolve into a WR+O bynary system. Furthermore, a lot of astrophysical phenomena occur because of the specifics of binary evolution, related to mass transfer (X-ray binaries, Chevalier & Ilovaisky (1998), supernovae Ib and Ic, Podsiadlowski et al. (1992), γ ray bursts, Fryer et al. (1999)).

The motivation for this thesis is to improve the knowledge of the evolution of massive stars, binary as well as single. We investigate several topics connected with the evolution of massive stars and present them in the following way:

- Chapter 2: Influence of metallicity and mass loss rate on WR stars radii

- Chapter 3: Progenitor evolution of WR+O binary systems and influence of rotation on accretion efficiency

- Chapter 4: Influence of stellar wind on accretion efficiency

- Chapter 5: Progenitor of collapsars and gamma ray burst

In the next sections of the first chapter we discuss general properties of WR stars, binary systems and collapsars in more details. We also present an overview of research done in this areas, together with the main results from this thesis.

1.2   Wolf-Rayet stars

WR stars are massive stars which have evolved from main sequence O stars (single or binary) and lost most or all of their hydrogen-rich envelope during their evolution (Chiosi & Maeder 1986; Maeder & Conti 1994). Material from the stellar envelope can be lost through stellar wind mass loss or through a mass transfer process in binary systems. Single stars should be more massive than $\sim 25 M_\odot$ to evolve into a WR star, because only then the mass loss rate is high enough to decrease the abundance of hydrogen in the outer layers (Massey et al. 2001). If an O star is in a close binary system, the loss of the hydrogen rich envelope does not depend only on the initial stellar mass but also on mass loss during the mass transfer process (Wellstein et al. 2001). As we already mentioned, WR stars have an extremely hot surface ($T_{\rm eff} > 50000$K) and a very high luminosity ($L \sim 10^{5-6} L_\odot$). They are characterized by high mass loss rate ($\sim 10^{-4-5} M_\odot {\rm yr}^{-1}$), however, the origin of this strong stellar winds is still not well understood (Gräfener et al. 2002). In hydrogen-free WR stars, which are in the focus of our research, the stellar wind is optically thick, preventing a direct determination of radii of WR stars, even when bolometric luminosities and effective temperatures are determined (Hamann et al. 1995; Moffat & Marchenko 1996).

As we already explained, the surface composition of WR stars is dominated by helium rather than hydrogen, and with spectra typically showing broad wind emission lines of elements like nitrogen (WN type), carbon (WC type), or oxygen (WO type): the products of core nucleosynthesis. Vanbeveren & Conti (1980) introduced WNE and WNL notation, meaning respectively stars without hydrogen (early types, more evolved) and stars with hydrogen (late types, least evolved) in their spectra. WC and WO stars (most evolved) do not have any hydrogen or nitrogen in their atmospheres, but carbon and oxygen are present on the stellar surface. All WR stars are further subdivided ranging from WN2 to WN9 and WC4 to WC9 depending on the relative strength of their nitrogen and carbon spectral lines (Smith et al. 1996).

The determination of radii of WR stars is important for different issues. First, the WR radius determines the height of the potential well which has to be overcomed by the wind. That is why in order to understand the strong wind of a WR star of given mass, its radius is a key quantity. The winds of hydrogen-free WR stars might be explained in terms of radiative driving if the radius at the base of the wind — i.e., the radius of the sonic point — is a factor of 2...3 larger (Nugis & Lamers 2002;
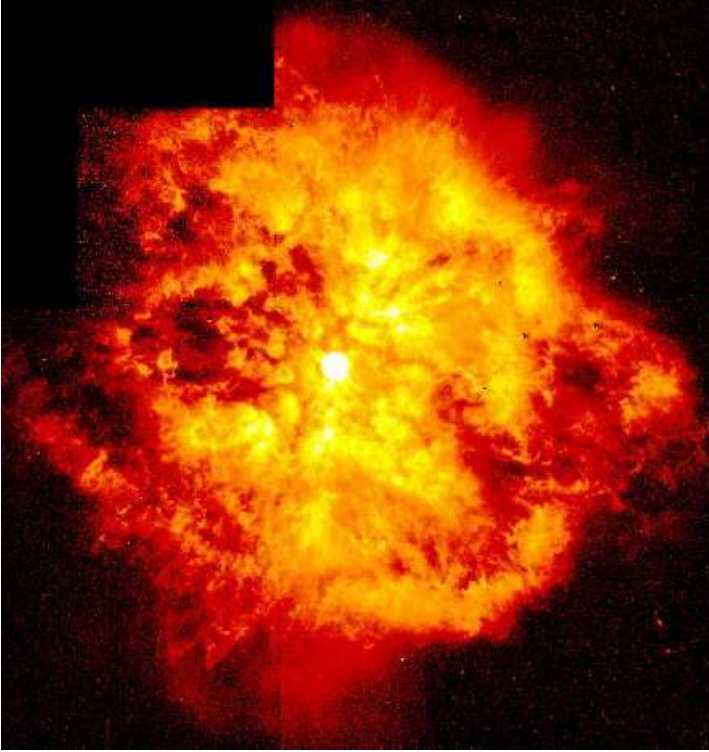
Figure 1.1: Wolf-Rayet star WR124, visible near the image center, is creating the surrounding nebula known as M1-67 (HST).

Gräfener et al. 2002) than what is predicted by WR stellar structure and evolution models (Langer 1989; Mowlavi et al. 1998; Heger & Langer 1996; Meynet & Maeder 2003). Second, WR star radii are important for the evolution of close binaries with a WR star component, in particular for initially wide binaries, where the hydrogen-rich envelope of the WR progenitor is removed in a so called common envelope evolution, resulting in a very close system (Taam & Sandquist 2000). Interesting examples where the WR radius may have influenced the evolution of the binary systems are the massive X-ray binaries Cyg X-3 (van Kerkwijk et al. 1996) and Cyg X-1 (Brown et al. 2001). Finally, the radii particularly of the most massive WR stars are relevant for the understanding of gamma-ray bursts (GRBs), which, according to the collapsar model (MacFadyen et al. 2001), have their origin in those WR stars which are massive enough to form a black hole at the end of their evolution (Heger et al. 2003a). The prediction of this scenario that GRBs are associated with so

called Type Ic supernovae — which are interpreted as supernovae originating from hydrogen-free WR stars (Woosley et al. 1993, 1995)— appears to be supported by recent GRB afterglow observations (Hjorth et al. 2003).

In Chapter 2, we investigate the radii of massive, chemically homogeneous helium star models, which have been shown to represent evolutionary models of hydrogen-free WN stars very accurately (Langer 1989). The radii of hydrogen-free WN stars in the mass range 10...30 $M_\odot$ are usually found to be in the range 1...2 $R_\odot$ (Langer 1989; Schaerer & Maeder 1992). However, it was found by Ishii et al. (1999) that there is a strong radius inflation for WR stars with solar metallicity and with masses larger than 15 $M_\odot$. Their 30 $M_\odot$ model has a radius of 8.6 $R_\odot$, and at 100 $M_\odot$ they find a helium star radius of 670 $R_\odot$. We find that solar metallicity helium stars above $\sim$15$M_\odot$ develop an extended envelope structure if mass loss is neglected, which is in agreement with the result of Ishii et al. (1999). Consequently, their effective temperature decreases and the helium zero age main sequence (further ZAMS) bends towards the red in the H-R diagram (diagram of effective temperatures and luminosities of stars). At low metallicity this feature is shifted to much higher masses.

We conclude that inflation of the envelope in massive stars with solar metallicity is related to the proximity of the stellar luminosity to the effective Eddington luminosity, i.e. to a high luminosity-to-mass ratio or a high envelope opacity. In other words, massive and metal-rich stars are prone to inflation. While the iron opacity peak in the OPAL tables (Iglesias & Rogers 1996) greatly increased the occurrence of inflated envelopes, the phenomenon itself is not dependent only on it. However, we showed that even in massive, metal-rich stars, inflation of the envelope is avoided if the stellar wind mass loss rate exceeds a certain critical value. Observationally derived mass loss rates of WR stars are at or above the critical value. As furthermore the surfaces of WR stars are not directly observable, it remains possible that inflated envelopes are not present in any of them. On the other hand, inflated envelopes may be unstable and lead to enhanced mass loss. It is remarkable in this context that the critical WR mass loss rate for inflation is close to the observed one (Nugis & Lamers 2000), and that few hydrogen-free stars, if any, can be found above the critical mass for inflation, which is about 15$M_\odot$ for solar metallicity.

1.3 Evolution of binary systems

The primary star in a binary system, the component with the greater mass, evolves faster than the secondary and through envelope expansion may reach the radius of its Roche lobe and start transferring mass onto the secondary star through the first Lagrangian point. This process is also called Roche lobe overflow, further denoted as RLOF).

The Roche lobe surface is a gravitational equipotential surface around two stars.
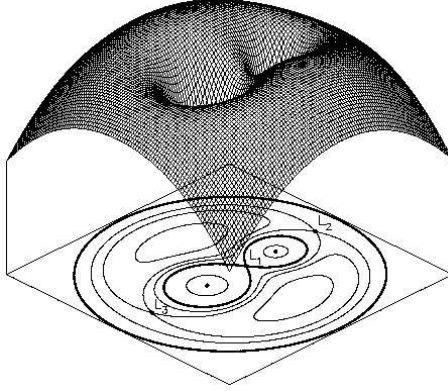
Figure 1.2: Three-dimensional representation of the potential (gravitational and centrifugal) of a binary system with mass ratio q=2 and equipotential contours in the orbital plane. L_1, L_2 and L_3 are Lagrangian points: points where acceleration vanishes (courtesy Martin Heemskerk).

The Roche lobe is a volume around each star in a binary system, inside which material is bound to that star. If the star expands past its Roche lobe, then the material outside of the lobe will fall into the other star. The potential energy is calculated in a frame of reference that corotates with the binary system. Because this frame of reference is a non-inertial frame, the gravitational potentials due to the masses of each of the two stellar nuclei (which vary inversely with distance from the center of each star) must be supplemented by a pseudo-potential corresponding to the centrifugal force.

Close to each stellar center the equipotential surfaces are approximately spherical and concentric with the nearer star. Far from the stellar system, the equipotentials are approximately ellipsoidal and elongated parallel to the axis joining the stellar centers. A critical equipotential intersects itself at the center of mass of the system. It is this equipotential which defines the Roche lobes (see Fig.1.2).

The critical Roche radius is defined as the radius equal to the radius of a sphere with the same volume as the Roche lobe. It depends on the masses of the stars M_1 and M_2 and on the orbital separation a (Eggleton 1983):

$$R_l = \frac{0.49a}{0.6 + q^{-2/3}\ln(1 + q^{1/3})} \tag{1.1}$$

where $q = M_1/M_2$ is the mass ratio of the system.

When both stars are smaller than their corresponding Roche lobes, the binary system is called a detached system. When only one star fills its Roche lobe, the system is called semi-detached and when both stars have filled their Roche lobes, the system is called a contact binary system. A star in a binary can overflow its Roche

radius during different phases of evolution: core hydrogen burning, shell hydrogen burning or shell helium burning phase, corresponding respectively to Case A, B and C of mass transfer (Kippenhahn et al. 1967). RLOF occurs because of the expansion of the stellar envelope which can occur on three different time scales: nuclear, thermal (Kelvin-Helmholtz) and dynamical in order of decreasing length. The thermal time scale is the ratio of the gravitational energy of the star and its luminosity and can be estimated as: $\tau \approx M^2/RL$, where M, R and L are mass, radius and luminosity of a star, respectively. For a more extended star, thermal time scale is shorter. For systems with large periods the critical radius necessary for RLOF is greater, so if mass transfer occurs it will happen on a small thermal time scale. Quantitatively, the thermal time scale is in the range of 10^4yr to 10^7yr and mass transfer which takes place on this scale is in the order of $\sim 10^{-3}$-10^{-4} $M_\odot$yr^{-1}. The nuclear time scale is the time required for a star to convert all available hydrogen to helium and depending on a stellar mass has values in order of 10^8yr to 10^{10}yr. Mass transfer which takes place on this scale is in the order of $\sim 10^{-6}$ $M_\odot$yr^{-1}. The intensity of the mass transfer rate is set by the amount of mass available in the stellar envelope and the characteristic time scale for envelope growth, i.e:

$$\dot{M}_{tr} = M/\tau \tag{1.2}$$

Depending of the value of the initial period of a binary system, the primary will fill its critical radius during different phases of evolution, and mass transfer will take place on a different time scales. If the initial binary system is very close i.e. the initial orbital period is in the order of days, RLOF will occur while the primary is still a main sequence star. This is Case A of mass transfer and it has two phases: fast and slow. The fast part of mass transfer takes place on the thermal time scale of the envelope. After this phase, the primary is still a core hydrogen burning star and still expanding, but now on nuclear time scale. That is why the primary will fill its Roche lobe again and the slow phase of mass transfer will start. After mass transfer, if there was no contact, the primary is a less massive star which finished core hydrogen burning and if there were accretion, the secondary is rejuvenated, which means that it is still a main sequence star, but more massive.

When initial binary period is in order of one or a few weeks, Case B mass transfer takes place. The helium core of the primary is contracting and the shell hydrogen burning envelope is expanding. Since the envelope of the primary is very extended, the thermal time scale is shorter, and the mass transfer rate is higher then in Case A. It has a value in the order of $\sim 10^{-3}$ $M_\odot$yr^{-1}. If there is no contact, the primary will lose its envelope and become a helium star and the secondary will be a rejuvenated (increased abundance of hydrogen in the core due to mass transfer), more massive star in the system.

Case C of mass transfer occurs when the initial period is in the order of years. The primary fills its Roche lobe during helium shell burning and mass transfer takes
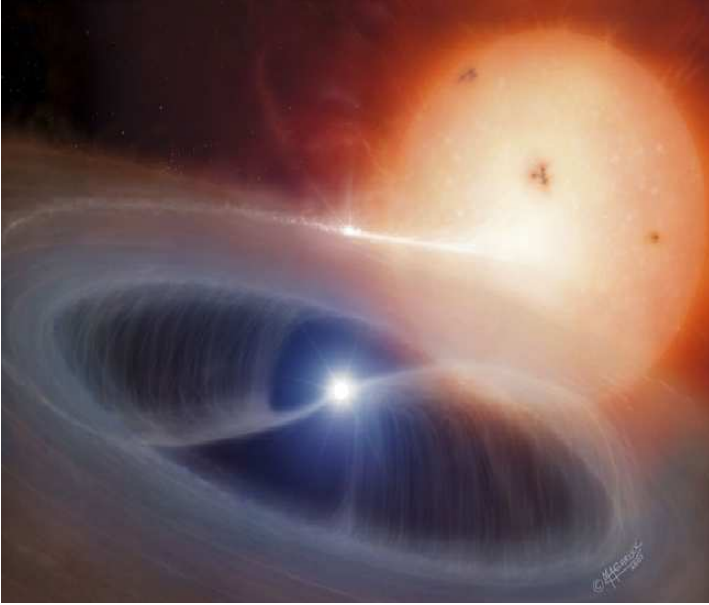
Figure 1.3: An artistic image of a binary system that undergoes a mass transfer process: A giant star is transfering matter onto a compact companion.

place on the dynamical time scale.

Evolutionary calculations of massive close binaries were done by various authors. General ideas about the formation of WR+O binary systems were given by Paczyński (1967), Kippenhahn et al. (1967), van den Heuvel & Heise (1972). Vanbeveren et al. (1979) modelled evolution of massive close Case B binaries with different assumptions for mass and angular momentum loss from the binary system. Vanbeveren (1982) made evolutionary models of massive close Case B binaries with primary masses between $20M_\odot$ and $160M_\odot$. He concluded that most of the WR primaries are remnants of stars initialy larger than $40M_\odot$ and that accretion efficiency (ratio of mass lost by the primary and mass accreted by the secondary) in these systems should be very low (β<0.3) in order to fit the observations. de Loore & de Greve (1992) made detailed calculations of massive Case B binary systems ranging in initial masses from $9M_\odot$ to $40M_\odot$ and mass ratio from 0.6 to 0.9. They made nonconservative models assuming that accretion efficiency is β=0.5. Wellstein & Langer (1999) and Wellstein et al. (2001) modelled massive binary systems with mass range 12..$60M_\odot$ and Wellstein (2001) presented rotating models for masses for initial masses $\sim15M_\odot$, both for Case A and Case B and initial mass ratio $q\sim1$.

Different values of β are used in modelling by different authors. So far, most

popular options in modelling of binary evolution are β=1 which corresponds to a conservative evolution (Refsdal & Weigert 1969; Kippenhahn 1969; Paczyński 1971; Wellstein 2001) and β=0.5 (de Loore & de Greve 1992; de Greve & de Loore 1992). However, these are just assumptions and any value of β between 0 and 1 is *a prori* possible. It has been proposed by Vanbeveren (1991) that β depends on mass ratio of the system.

It is not yet known what are the processes that can expel matter out of a binary system. Vanbeveren (1991) proposed that if a binary component is more massive then $\sim$40-50$M_\odot$ it will go through an luminous blue variable star (LBV) phase of enhanced mass loss, which will prevent the occurrence of RLOF.

It is shown in Chapter 3 that the mass accretion rate can be significantly decreased due to rotation of the secondary close to the critical value. There, we investigate the possibility that the progenitor evolution of WR+O systems (HD186943, HD90657 and HD211853) was through Case A mass transfer with β≈0.1. For non-rotating models we assume β=0.1 based on the estimate from the simplified approach. For rotating models accretion efficiency decreases when the secondary star is spinning up close to critical rotation. Primary mass range for non-rotating models is 41..75$M_\odot$ and for rotating models 41..65$M_\odot$. In Chapter 4 we investigate the possibility that radiation pressure from the secondary prevents accretion. We find that even for a moderate mass transfer rate ($5\cdot10^{-6}M_\odot\mathrm{yr}^{-1}$) the wind and radiative momenta do not alter the dynamics of the accretion stream.

Furthermore, there are other possibilities in binary evolution, which are so far, not known and explained in details: common envelope and ring structure. In the case of very violent mass transfer, the secondary can expand and fill its Roche lobe, and common envelope evolution will occur. Due to the friction of stars moving in an envelope, angular momentum will be decreased and the system will end up in a merger or as a system with very small period (de Kool 1990). Also, a stem can go through a ring phase. After the secondary fills its Roche lobe, in the case of not extremely high mass transfer rate, the system will start losing mass through the second Lagrangian point. Lost matter will form a ring around system and remove some of the angular momentum. The system will end up similar as in the case of common envelope evolution (Vanbeveren et al. 1998).

The central focus of Chapters 3 and 4 is to investigate the fate of mass lost from the primary during mass transfer process: is this material lost to the interstellar medium? Is it accreted onto the secondary and if so, to what extent? What are the physical processes that can expel matter from the binary system and prevent the secondary from accreting?
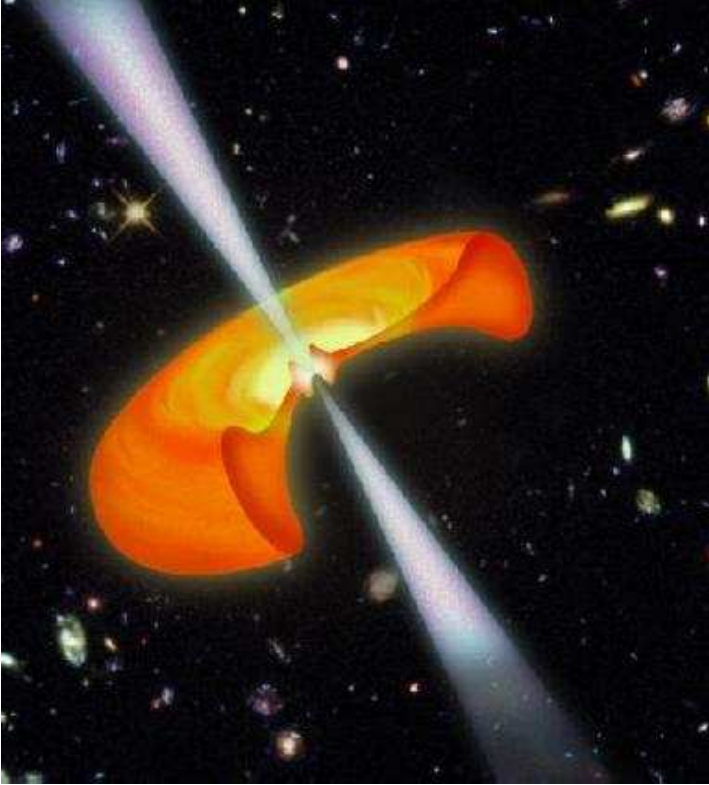
Figure 1.4: An artistic image of a collapsar. The black hole is accreting the rest of the core material. The heated gas at the poles expands in a highly relativistic jet which tunnels through the star. This jet, and the shock wave which accompanies it, may produce gamma-ray burst accompanied by a Type Ib/c supernova.

1.3.1 Progenitor evolution of WR+O binaries and influence of rotation on accretion efficiency

In Chapter 3, we investigate those binaries that contain a Wolf-Rayet and a main sequence O star. We have chosen three WN+O systems (HD186943, HD90657 and HD211853) with similar mass ratios (∼0.5) and orbital periods (6..10 days). As clearly the two stars in these systems must have undergone a strong interaction in the past, an understanding of their progenitor evolution may be the key to constrain the mass transfer efficiency in massive binaries: which fraction of the mass leaving the primary star is accumulated by the secondary star during a mass transfer event? Orbital periods of these systems are short enough to indicate that there was an interaction between components during previous evolution, but also long enough that

these systems can be the result of stable mass transfer evolution.

We calculate evolution of nonconservative rotating Case A binary systems with primaries M_1=41..65M$_\odot$ until the WR+O stage. We find that Case A rotating binaries can evolve highly nonconservative. During fast Case A mass transfer in a very massive rotating binaries (M_1>40M$_\odot$) and with mass ratios $q\leq$1.7-2.0, even 90% of the matter can be expelled from the system, due to the fact that accretion rate can be limited by critical rotational velocity of the secondary after spinning up during accretion. Wellstein found the same for less massive, Case B, $q\approx$1 binary systems. We find possible ways to produce short period WR+O binaries HD1869443 and HD90657:

- Non-rotating Case A models with primaries M_1=41..56M$_\odot$, initial mass ratios $q\approx$1.7..2.0, initial orbital periods 3 and 6 days and adopted accretion efficiency $\beta\leq$0.1.

- Rotating Case A models (for which the physics is well determined) with primaries M_1=41..65M$_\odot$, initial mass ratios $q\approx$1.7..2.0 and initial orbital period 6 days.

1.3.2 Influence of stellar wind on mass accretion efficiency

In Chapter 4 we investigate to what extent the radiation and stellar wind momenta in a massive close binary system can remove part of the matter flowing from one towards another star during a mass transfer phase. In other words, can stellar wind radiation pressure change dynamics and behaviour of accretion stream produced by Roche lobe overflow. We perform radiation-hydrodynamics simulations in the co-rotating frame of a binary system made-up of two main sequence stars of 27M$_\odot$ and 26M$_\odot$ in a 4 day orbit. We calculated radiation force and wind properties for each component and studied the interaction of the winds of both stars with the accretion stream originating from the Roche-lobe filling component. For our simulation, we adopted a mass transfer rate of $5\cdot10^{-6}$M$_\odot$yr^{-1}, a mid-point in the range of values during massive binary star evolution. Our simulations show that even for such moderate mass transfer rates, the wind and radiative momenta do not alter the dynamics of the accretion stream which is observed to follow essentially ballistic trajectories. The central result of our calculation is that the dynamics of mass transfer in massive close binary stars is not affected in any noticeable way by the radiation and wind momenta from each luminous component. We conclude that those mechanisms cannot be the origin of the non-conservative mass transfer required to explain the observed mass ratios of many Wolf-Rayet binaries.

1.4 Massive stars as collapsar progenitors

A collapsar is a massive ($M_{in} \sim$35-40M$_\odot$, Fryer (1999)) rotating star whose core collapses to form a black hole (Woosley 1993b; MacFadyen & Woosley 1999). If a star has enough angular momentum in the equator ($j \geq 3 \cdot 10^{16}$cm^{2}s^{-1}), an accretion disk will be formed around the black hole. The accretion of the rest of the core at accretion rates up to 0.1-10M$_\odot$ s^{-1} in the newly-formed black hole releases large amounts of energy ($\sim 10^{51}$erg s^{-1}) some of which is deposited along the low density rotation axis of the star. The heated gas at the poles expands in a highly relativistic jet which tunnels through the star. This jet, and the shock wave which accompanies it, may produce a gamma-ray burst accompanied by a Type Ib/c supernova.

Heger et al. (2000b) have calculated models of a 25M$_\odot$ star that could form a black hole by fallback, which means that a SN explosion occurs while core forms neutron star, but so much matter fails to escape and falls back onto the neutron star that it turns into a black hole. This star ends its life as a red supergiant with an iron core of 1.9M$_\odot$, a helium core of 8.06M$_\odot$, and a low density envelope of 6.57M$_\odot$. They found that this star has sufficient angular momentum to form an accretion disk around a black hole which may lead to an asymmetric, jet-driven supernovae, or in the case that the star lost its hydrogen envelope, even a GRB can result.

These calculations left out the influence of a magnetic field that can significantly influence the angular momentum transport processes in the star, for example slowing down the helium core of the star during red supergiant phase (Spruit & Phinney 1998), but also spinning-up the core if the star accretes mass from a binary companion.

It is shown in Chapter 3 of this thesis and by Wellstein (2001) that during the mass transfer phase in a binary system, the secondary (accreting) star can spin up to close to the critical rotation, i.e. the surface layers of this star can gain large amount of angular momentum. This angular momentum can be transported inwards and increase the rotation velocity of the stellar core.

Heger et al. (2000a) showed that the specific angular momentum of the stellar core depends significantly on the inhibiting effect of the μ-gradient (chemical profile) on rotational mixing processes. If μ-gradients represent a barrier for rotational mixing and transport of angular momentum, the core does not lose large amount of angular momentum during the evolution.

In Chapter 5 we show that a single rotating 42M$_\odot$ star (v_{surf}=200 km s^{-1}) evolves into a red supergiant with the core having a specific angular momentum of 10^{17}cm^{2}s^{-1}. This star loses angular momentum during its evolution due to stellar wind mass loss. However, since rotational mixing processes are suppressed by the μ-gradients, the core does not lose a significant amount of angular momentum. Angular momentum loss from the stellar core during helium burning is not significant. We estimate that the core has a specific angular momentum of $\sim 3.5 \cdot 10^{16}$cm^{2}s^{-1}

at the end of the evolution, so we can conclude that this star has enough angular momentum to form an accretion disk around the black hole that forms in supernova explosion (MacFadyen & Woosley 1999, limit for formation of accretion disk is $j \geq 3 \cdot 10^{16} \mathrm{cm}^2 \mathrm{s}^{-1}$) i.e. it might produce a collapsar and in the case that the hydrogen envelope is lost during the red supergiant phase, a gamma-ray burst can be the result.

We also model the evolution of a $56 \mathrm{M}_\odot + 33 \mathrm{M}_\odot$ rotating binary system with an initial orbital period of 6 days. In this case, the secondary star loses significant amounts of angular momentum due to initial synchronization. However, matter that is being accreted during mass transfer processes increase the angular momentum of the star. After the primary explodes in a SN, the secondary evolves into a red supergiant with a core that has specific angular momentum of $j \sim 10^{17} \mathrm{cm}^2 \mathrm{s}^{-1}$. In the same way as for the single star, we can conclude that this star might evolve into a collapsar, producing a gamma-ray burst.

If magnetic fields are included in the calculations, the stellar core loses more angular momentum during the main sequence phase and between hydrogen exhaustion and helium ignition, because the magnetic field torques try to keep the star in solid body rotation. The result is that stars with magnetic field end up with lower specific angular momentum in the core, in the order of magnitude $j \sim 10^{15} \mathrm{cm}^2 \mathrm{s}^{-1}$ at the beginning of helium core burning, which is a lower value than needed to produce a collapsar and a gamma-ray burst. During further evolution through the red supergiant phase, the core will be slowed down even more by the very slowly rotating envelope.

Chapter 2

Are luminous and metal-rich Wolf-Rayet stars inflated?

Abstract. We have calculated chemically homogeneous models of Wolf-Rayet stars of 10 to 200 $M_\odot$ for two metallicities (Z=0.02 and Z=0.001), using OPAL opacities. We confirm the radius extension for luminous, metal-rich Wolf-Rayet stars reported previously by Ishii et al. (1999), i.e. the inflation of the hydrostatic core radius. We also investigate the influence of a stellar wind on the radius extension. For that purpose we constructed theoretical helium main sequences for 15, 18, 24 and 30 $M_\odot$ with stellar wind mass loss rates of $10^{-5} M_\odot \mathrm{yr}^{-1}$ and $10^{-4} M_\odot \mathrm{yr}^{-1}$ and models for a 24$M_\odot$ star for a few intermediate values of mass loss rate. We show that for small values of the stellar wind mass loss rate, an extended envelope structure is still present. However, for mass loss rates above a critical value, for which we derive an expression, Wolf-Rayet radii decrease and the stellar structure becomes compact. We briefly discuss possible evolutionary and observational consequences of an inflated envelope for a mass losing Wolf-Rayet star.

authors: Jelena Petrovic, Onno Pols, Norbert Langer
Submitted to A&A

2.1   Introduction

Wolf-Rayet (WR) stars are the bare cores of massive stars which have lost most or all of their hydrogen-rich envelope (Chiosi & Maeder 1986; Maeder & Conti 1994). While in close binary systems, the loss of the envelope does not depend only on the initial stellar mass (Wellstein et al. 2001), single stars need to be more massive than $\sim 25 M_{\odot}$ to evolve into a WR star (Massey et al. 2001, e.g.). WR stars are characterized by strong stellar winds, whose origin is still not well understood (Gräfener et al. 2002). In particular in hydrogen-free WR stars, which are in the focus of our study, the stellar wind is optically thick, preventing a direct determination of radii of WR stars, even when bolometric luminosities and effective temperatures are determined (Hamann et al. 1995; Moffat & Marchenko 1996).

The knowledge of the radii of WR stars is essential for the following problems. In order to understand the strong wind of a WR star of given mass, its radius is a key quantity, as it determines the height of the potential well which has to be overcome by the wind. The winds of hydrogen-free WR stars might be explained in terms of radiative driving if the radius at the base of the wind — i.e., the radius of the sonic point — is a factor of 2...3 larger (Nugis & Lamers 2002; Gräfener et al. 2002) than what is predicted by WR stellar structure and evolution models (Langer 1989; Mowlavi et al. 1998; Heger & Langer 1996; Meynet & Maeder 2003).

WR star radii are also important for the evolution of close binaries with a WR star component, in particular
for initially wide binaries, where the hydrogen-rich envelope of the WR progenitor is removed in a so called common envelope evolution, resulting in a very close system Taam & Sandquist (2000). Interesting examples where the WR radius may have influenced the evolution of the binary systems are the massive X-ray binaries Cyg X-3 (van Kerkwijk et al. 1996) and Cyg X-1 (Brown et al. 2001).

Finally, the radii particularly of the most massive WR stars are relevant for the understanding of gamma-ray bursts (GRBs), which, according to the collapsar model MacFadyen et al. (2001), have their origin in those WR stars which are massive enough to form a black hole at the end of their evolution (Heger et al. 2003a). The prediction of this scenario that GRBs are associated with so called Type Ic supernovae — which are interpreted as supernovae originating from hydrogen-free WR stars (Woosley et al. 1993, 1995) — appears to be supported by recent GRB afterglow observations (Hjorth et al. 2003).

In this paper, we investigate the radii of massive, chemically homogeneous helium star models, which have been shown to represent evolutionary models of hydrogen-free WN stars very accurately Langer (1989). The radii of such models in the mass range 10...30 $M_{\odot}$ are usually found to be in the range 1...2 $R_{\odot}$ (Langer 1989; Schaerer & Maeder 1992). However, while the helium star models of Ishii et al. (1999) predict radii in agreement with previous results up to 15 $M_{\odot}$, they find a

strong radius inflation for larger masses. I.e., at solar metallicity, their $30\,\mathrm{M}_\odot$ model has a radius of $8.6\,R_\odot$, and at $100\,\mathrm{M}_\odot$ they find a helium star radius of $670\,R_\odot$.

Here, we construct massive helium star models using OPAL opacities, which have been identified by Ishii et al. (1999) as a key model ingredient to find such large helium star radii. In Sect. 2.2, we describe the details of the way our models are constructed. In Sect. 2.3 and Sect. 2.4, we then describe the dependence of the radii of our helium stars on the metallicity and on the adopted stellar wind mass loss rate, respectively. Sect. 2.5 gives a general discussion of the effect of increased helium star radii, and Sect. 2.6 summarizes our results.

2.2   Computational method and input physics

We modelled the structure of chemically homogeneous zero age helium main sequence stars with the hydrodynamic stellar evolution code described in Langer et al. (1988) and Langer (1989). The OPAL opacities of Iglesias & Rogers (1996) are implemented. We produced models at two different metallicities, Z=0.02 and Z=0.001, with an abundance distribution which is typical for hydrogen burning ashes, and for 10, 12, 15, 18, 24 and $30\mathrm{M}_\odot$. We constructed models without mass loss for both metallicities, and additional models with mass loss rates of $10^{-5}\mathrm{M}_\odot\mathrm{yr}^{-1}$ and $10^{-4}\mathrm{M}_\odot\mathrm{yr}^{-1}$ for Z=0.02. We also constructed a series of models for a star of $24\mathrm{M}_\odot$, with five intermediate values of the mass loss rate. Nuclear energy production in our models comes from the 3α reaction, while that of the $^{14}\mathrm{N}(\alpha,\gamma)$ reaction is neglected (see below).

The models without mass loss are set in complete hydrostatic and thermal equilibrium. For the models with mass loss this is not possible, first of all since mass loss implies non-stationarity, and second — as explained in detail in Sect. 2.4 — the mass loss rates considered here imply outflow velocities and, more importantly, inertia terms which are significant. I.e., our models with mass loss are not in hydrostatic equilibrium. However, as the mass loss time scale is longer than both the dynamical and the thermal time scale of the star, our mass-losing models are characterized by quasi-stationarity and by thermal equilibrium. For both types of models, the radius R of our WR models is defined by an optical depth $\tau(R) = 2/3$, as determined from a gray plane-parallel atmosphere integration. While for the models without mass loss, this is the simplest consistent choice, the influence of this assumption on the mass losing models is discussed in Sect. 2.5.

In order to obtain an independent consistency check on our results for constant masses and on those of Ishii et al. (1999), we also computed the structure of helium star models in hydrostatic and thermal equilibrium with the stellar evolution code of Eggleton (1971) and Eggleton (1972). We used the version described by Pols et al. (1995), with the OPAL 1996 opacities implemented as described by Eldridge

& Tout (2003). Because this code code can only deal with nearly hydrostatic stars (the inertial terms are neglected) we did not consider mass loss in these calculations. The models were computed for the same two metallicities as above, on a fine grid of masses between 1 and $200\,\mathrm{M_\odot}$ (spaced by 0.002 in $\log M$). The abundance distribution is homogeneous except that $^{14}\mathrm{N}$ from the hydrogen ashes was assumed to be already consumed inside the convective core[1].

2.3   Results: $\dot{M} = 0$; $Z = 0.02$ and $Z = 0.001$

Fig. 2.1 shows the theoretical helium zero-age main sequences as obtained from our models without mass loss, for the metallicities Z=0.001 and Z=0.02. Models with the same mass and different metallicities have roughly the same luminosity, but the effective temperature is lower for higher metal content. The influence of the metallicity becomes significant for stellar masses larger than $\sim 15\mathrm{M_\odot}$ and then increases with increasing stellar mass. For masses above $\sim 15\mathrm{M_\odot}$, the surface temperature of the metal-rich models decreases with increasing mass, i.e., the upper part of the helium ZAMS in the H-R diagram is bent towards the red.

Consequently, the helium stars more massive than $\sim 15\mathrm{M_\odot}$ with solar metallicity have significantly larger radii than the corresponding stars with a metallicity of Z=0.001 (cf. Table 2.1). For M<$15\mathrm{M_\odot}$, the radii of equal-mass models differ by less than 10%. The radius of a $15\mathrm{M_\odot}$ star is $\sim 15\%$ larger at Z=0.02 compared to Z=0.001. This difference increases with stellar mass, e.g. a $30\mathrm{M_\odot}$ star is ~ 3.6 times larger due to higher metal content.

The results obtained with the Langer and Eggleton codes correspond very well, as is demonstrated in Fig. 2.1 and Table 2.1. In spite of quantitative differences of order 10% between the model radii for masses larger than $24\mathrm{M_\odot}$, the qualitative behaviour is very similar and furthermore confirms the findings of Ishii et al. (1999), as can be seen by comparing our Fig. 2.1 with their Fig. 7. For masses greater than $100\mathrm{M_\odot}$ we find a giant structure with radii of several $100\mathrm{R_\odot}$, as did Ishii et al. This demonstrates that inflation is a common feature of massive helium star models and not the result of numerical artifact. The models for Z=0.001 remain compact up to $100\mathrm{M_\odot}$, but for larger masses they are also inflated.

The inflated massive, metal-rich models have a peculiar envelope structure. Fig. 2.2 compares the density profiles of our metal-rich $15\mathrm{M_\odot}$ and $24\mathrm{M_\odot}$ (as computed with the Langer code) stars with their metal-poor counterparts. An extended envelope structure and a density inversion are present in the outer layers for both masses

---

[1]Without this assumption the main energy production comes from $^{14}\mathrm{N}(\alpha, \gamma)$ rather than the 3α reaction, and we find radii that are 5...10 per cent larger than the results presented here. In actual WR stars nitrogen burns very quickly before any substantial 3α fusion has taken place, so that models in which core nitrogen is already consumed more closely represent 'zero-age' helium stars.

Table 2.1: Radii of zero age helium star models for masses in the range 10...30 $M_\odot$, for two metal-licities, Z=0.02 and Z=0.001, as indicated by the upper index, and for various mass loss rates, i.e. $\dot{M} = 0, 10^{-4}, 10^{-5} M_\odot \, \mathrm{yr}^{-1}$, as indicated by the lower index. The subscript "E" refers to models calculated with the Eggleton code. The last two column lists results of Ishii et al. (1999) and Langer (1998).

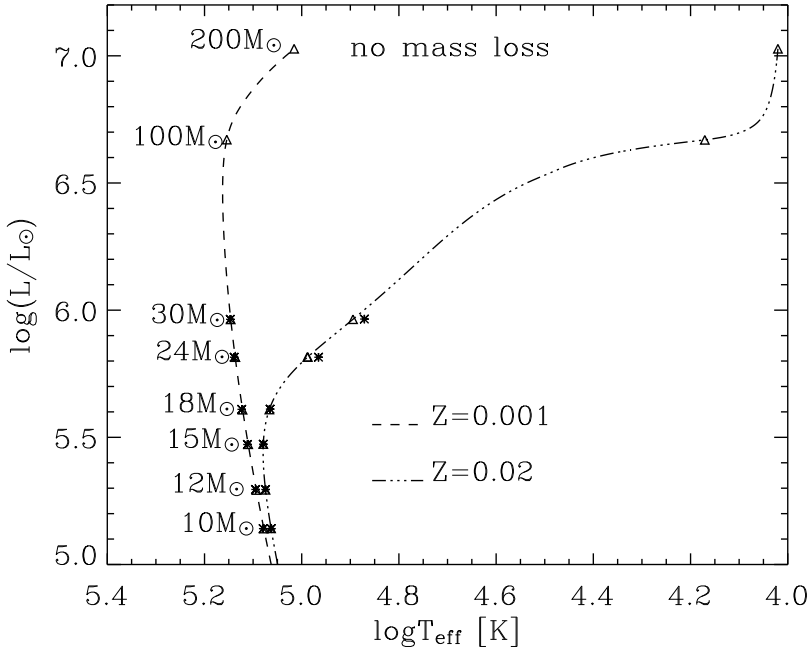| M	$R_0^{.001}$	$R_{0,E}^{.001}$	$R_0^{.02}$	$R_{-5}^{.02}$	$R_{-4}^{.02}$	$R_{0,E}^{.02}$	$R_{0,I}^{.02}$	$R_{0,L}^{.02}$
$M_\odot$	$R_\odot$	$R_\odot$	$R_\odot$	$R_\odot$	$R_\odot$	$R_\odot$	$R_\odot$	$R_\odot$
10	0.86	0.87	0.93	-	-	0.93	-	0.92
12	0.95	0.96	1.05	-	-	1.05	1.1	-
15	1.08	1.09	1.26	1.26	1.16	1.26	1.3	1.16
18	1.20	1.22	1.58	1.58	1.34	1.57	-	-
24	1.42	1.43	3.16	3.11	1.61	2.85	-	-
30	1.61	1.63	5.79	5.78	1.88	5.20	8.3	1.73

Figure 2.1: Theoretical helium zero age main sequences for metallicities Z=0.001 and Z=0.02 without mass loss calculated with the Eggleton's code. Triangles indicate models for a particular mass. Stars indicate corresponding models computed with the Langer code.
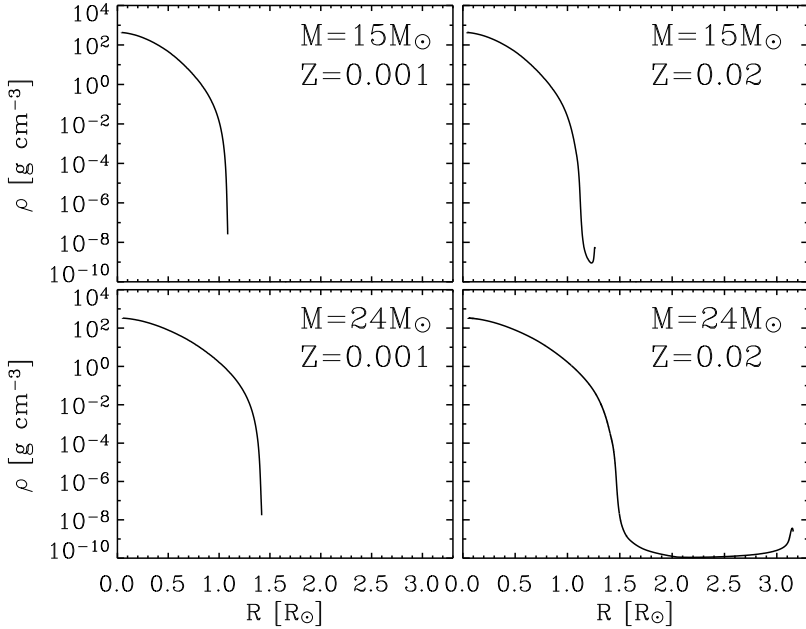
Figure 2.2: Density profiles for helium stars of $15M_\odot$ and $24M_\odot$. Models with higher metallicity have extended envelopes and a density inversion near the surface.

at the higher value of the metallicity. For $15M_\odot$ at Z=0.02, there is a narrow layer with low density ($\sim 10^{-9}$ g cm^{-3}) beneath the stellar surface, where the density reaches a value of $\sim 10^{-8}$ g cm^{-3}. For the $24M_\odot$ star with solar metallicity, the envelope is significantly more extended and there is a broad layer ($\sim 1R_\odot$) with a density of $\sim 10^{-10}$ g cm^{-3} beneath the surface, where the density is almost two orders of magnitude higher. The extended envelope contains only about 10^{-10} of the total stellar mass. Models with a metallicity of Z=0.001 exhibit no extended envelope structure, and the density decreases monotonously from the stellar interior to the surface.

In Fig. 2.3 and Fig. 2.4, we compare the opacity and luminosity structure of our $10M_\odot$ models — for which the metal content has almost no effect on the structure — with our $24M_\odot$ stars, which show a significant inflation at Z=0.02. The upper panel of both figures show the opacity profiles for both values of metallicity. For the model with higher metal content, the opacity is larger due to the iron opacity peak at $T \sim 2.5 \times 10^5$K in the OPAL tables, which increases with metallicity. While in the $10M_\odot$ models the achieved opacity is larger than at $24M_\odot$, the radius range for which the opacity is high is large only in the metal-rich $24M_\odot$ star.
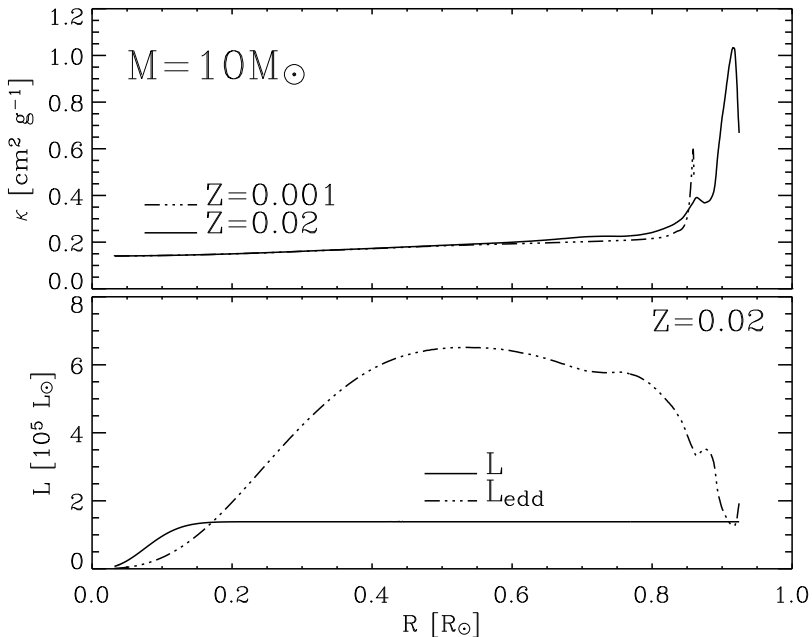
Figure 2.3: Upper plot: Opacity as a function of radius for $10\mathrm{M}_\odot$ helium stars of Z=0.001 and Z=0.02. Lower plot: Luminosity and Eddington luminosity as a function of radius for $10\mathrm{M}_\odot$ helium star of solar metallicity.

To understand the effect of the iron opacity peak on the stellar radius, it is useful to compare the local luminosity L with the local Eddington luminosity

$$L_{\mathrm{Edd}} = 4\pi cGM(r)/\kappa, \qquad (2.1)$$

where $M(r)$ is the Lagrangian mass coordinate and κ the opacity coefficient. The lower plot of Fig. 2.3 shows profiles of the luminosity and the local Eddington luminosity for the metal-rich $10\mathrm{M}_\odot$ model. The Eddington luminosity is significantly higher than local stellar luminosity throughout the star, except in a narrow convective layer close to the surface. In the $24\mathrm{M}_\odot$ model, the local stellar luminosity almost equals the Eddington luminosity in the extended outer radiative parts (between points 1 and 2 in Fig. 2.4), while it exceeds the Eddington value in an extended convective layer above (between points 2 and 3).

We interpret this behavior as follows. The WR models considered here follow a mass-luminosity relation as $L_\star \propto M_\star^{1.35}$ (Langer 1989). Therefore, for a fixed opacity, more massive stars are generally closer to their Eddington limit. Secondly, like for hydrogen-rich main sequence stars, the density of helium stars decreases with
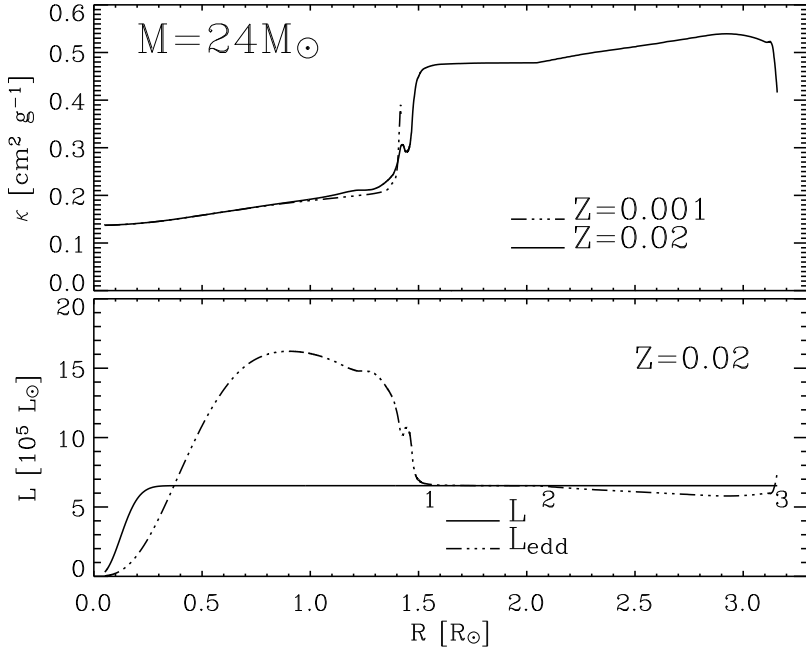
Figure 2.4: Upper plot: Opacity as a function of radius for a $24M_\odot$ helium stars of $Z=0.001$ and $Z=0.02$. Lower plot: Luminosity and Eddington luminosity as a function of radius for a $24M_\odot$ helium star of solar metallicity. 1-2 Radiative layers with luminosity close to Eddington limit; 2-3 Convectively unstable layers.

increasing stellar mass. This has the consequence that the convection zone due to the iron opacity peak — which is present in all considered models — transports energy less efficiently in more massive helium stars.

   Our results indicate that, while for stars below $\sim M>15M_\odot$ any small super-Eddington flux can be transported by convection without structural consequences, for stars above $\sim M>15M_\odot$ at $Z=0.02$, a compact hydrostatic structure is impossible as it would require $L>L_{\mathrm{Edd}}$ in part of the envelope where even convection can not carry the excess luminosity. Thus, a compact structure would give rise to an outward acceleration, i.e. to an inflation of the envelope. The reduced density due to the expansion has two consequences, a further reduced convective energy transport efficiency, and a reduction of the opacity as the iron peak decreases towards lower densities. While the first effect is limited as the convective flux in the outermost convective layers is already negligible before the expansion, the second effect allows that a hydrostatic solution is one with an extended envelope. Throughout this envelope the luminosity remains very close to the Eddington limit. At low Z, the
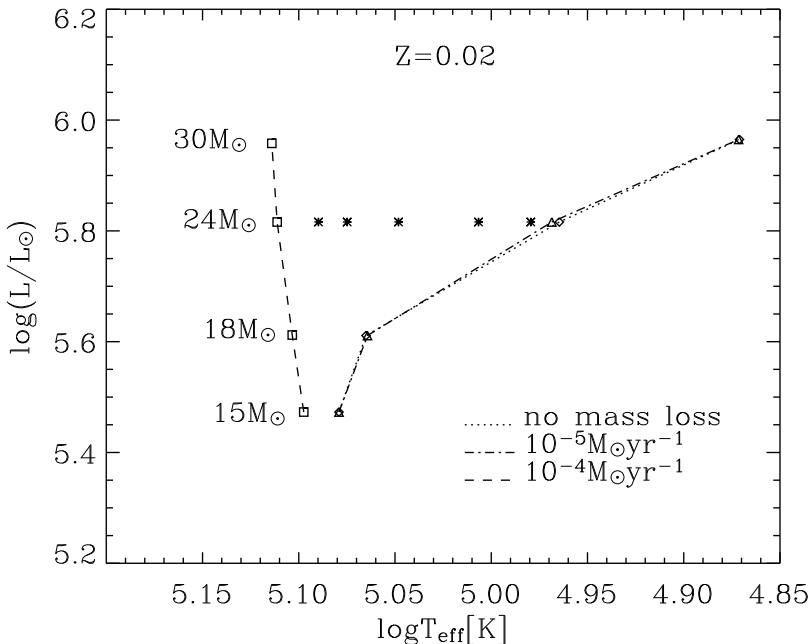
Figure 2.5: Theoretical helium zero age main sequences for mass loss rates 0, $10^{-5}\mathrm{M_\odot yr^{-1}}$ and $10^{-4}\mathrm{M_\odot yr^{-1}}$. Models have been calculated for 15, 18, 24 and 30$\mathrm{M_\odot}$. Star symbols indicate 24$\mathrm{M_\odot}$ models for intermediate mass loss rates (see Fig. 2.6).

envelope opacity is lower and L_{Edd} larger, so that a compact hydrostatic structure remains possible up to a larger mass. Hence, the increase of the envelope opacity with Z, and the increase in L/M with mass, are the prime causes for the extended envelopes and large radii of massive high-metallicity WR stars.

2.4 Results: $\dot{M} > 0$; $Z = 0.02$

In this section, we investigate the influence of stellar wind mass loss on the extended envelope structure obtained for massive, metal-rich hydrostatic helium star models. For Z=0.02, we calculated hydrodynamic, mass losing models for 15, 18, 24 and 30$\mathrm{M_\odot}$ for two different mass loss rates: $10^{-5}\mathrm{M_\odot yr^{-1}}$ and $10^{-4}\mathrm{M_\odot yr^{-1}}$. For 24$\mathrm{M_\odot}$, we constructed additional models for intermediate mass loss rates. Fig. 2.5 compares the location of these models in the HR-diagram to the location of the models without mass loss.

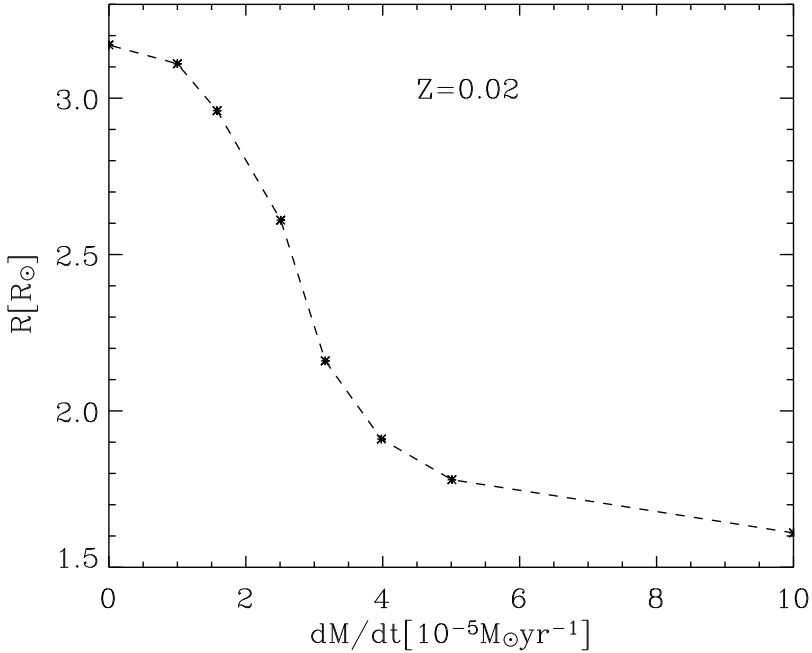We notice that a mass loss rate of $10^{-5}\mathrm{M_\odot yr^{-1}}$ has almost no effect on the po-

Figure 2.6: Radii of eight $24M_\odot$ helium star models at $Z=0.02$ as a function of the adopted mass loss rate. These models are also indicated in the HR diagram (Fig. 2.5).

sitions of the stars in the H-R diagram. The envelopes of stars more massive than $\sim15M_\odot$ are still extended and their effective temperatures are relatively low. However, a mass loss rate of $10^{-4}M_\odot yr^{-1}$ significantly changes the envelope structure: The stars are compact with high effective temperatures, and indeed follow closely the mass-radius relation for helium stars of Langer (1989). For $24M_\odot$, we have computed models with intermediate mass loss rates, whose radii are plotted in Fig. 2.6. It shows that the radii of our models are not bimodal, as might be suggested by Fig. 2.5, but change continuously and monotonously as function of the adopted mass loss rate.

Fig. 2.7 shows the density profiles of a $24M_\odot$ star for four different mass loss rates. With a mass loss rate of $2.5\times10^{-5}M_\odot yr^{-1}$, the radius is smaller than that of a constant-mass model. With even higher mass loss rates the envelope becomes more and more compact. On the other hand, the structure in the core is unaffected by mass loss: the density profiles for $R<1.5R_\odot$ are identical for each adopted mass loss rate. The core remains in hydrostatic equilibrium, unlike the extended envelope, as we discuss below.

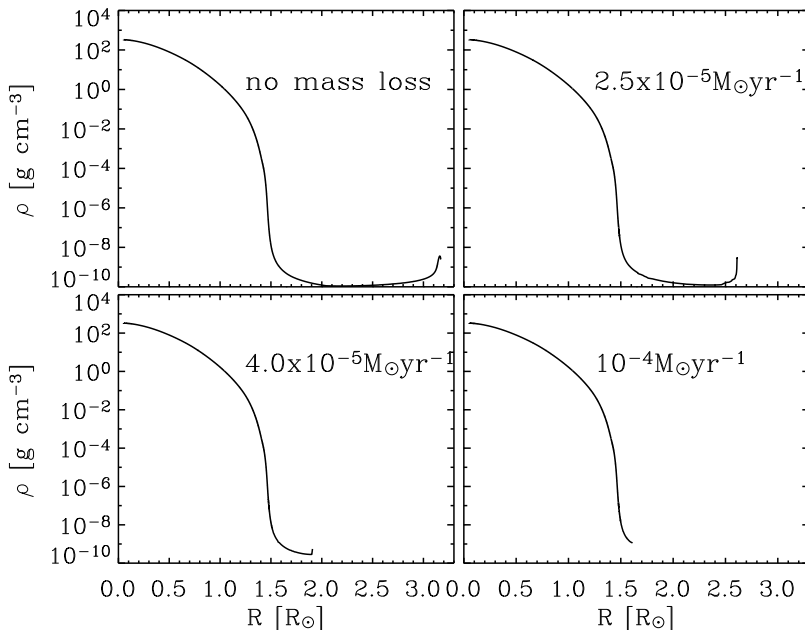Fig. 2.8 shows the velocity profiles in the outer stellar layers for our $24M_\odot$ star

Figure 2.7: Density profiles for helium star models of $24M_\odot$ for four different values of the mass loss rate: $0, 2.5\times10^{-5}M_\odot\mathrm{yr}^{-1}, 4.0\times10^{-5}M_\odot\mathrm{yr}^{-1}, 10^{-4}M_\odot\mathrm{yr}^{-1}$.

for three different values of the mass loss rate. The stellar mass loss implies an outward mass flux through the envelope. Mass conservation and quasi-stationarity imposes that the lower the density the faster the matter has to move:

$$v = \dot{M}/\left(4\pi r^2 \rho\right).\tag{2.2}$$

For the adopted mass loss rates, the low densities in the extended envelopes of our models ($\sim 10^{-10}$ g cm^{-3}; cf. Fig. 2.7) imply velocities of several hundred kilometers per second. This can be compared to the isothermal sound speed in the stellar envelope,

$$v_s = \sqrt{RT/\mu},\tag{2.3}$$

where T is the temperature, R is the gas constant and μ is the mean molecular weight. Both are plotted in Fig. 2.8, which shows that the implied flow velocities in the extended envelopes of our models are highly supersonic.

In the hydrostatic model, the acceleration due to the pressure gradient is balanced by gravity. In the models with mass loss, the sum of these two accelerations is not zero. Instead, there is an accelerated radial motion and the inertial acceleration becomes important, and more so for larger mass loss rates.
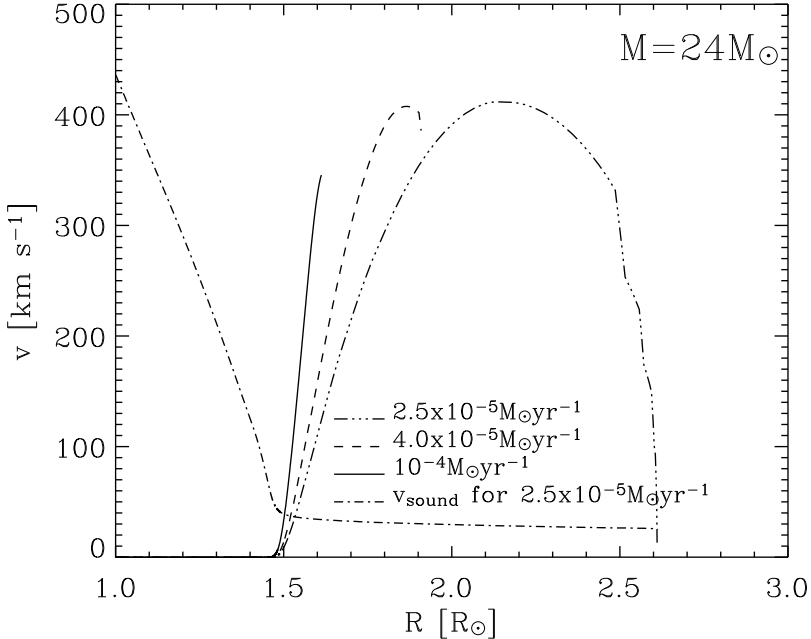
Figure 2.8: Velocity profiles for $24M_\odot$ helium star models, for three different mass loss rates: $2.5\times10^{-5}M_\odot\mathrm{yr}^{-1}$, $4.0\times10^{-5}M_\odot\mathrm{yr}^{-1}$, $10^{-4}M_\odot\mathrm{yr}^{-1}$, compared with the sound speed for $2.5\times10^{-5}M_\odot\mathrm{yr}^{-1}$.

For a mass loss rate of $\sim10^{-5}M_\odot\mathrm{yr}^{-1}$, the inertia term is still rather negligible, but it is of the order of the gravitational acceleration in the outer envelope for $\dot{M}=10^{-4}M_\odot\mathrm{yr}^{-1}$. This explains why the envelope structure is not affected for the lower mass loss rates considered here.

More quantitatively, approximating the inertia term as $dv/dt = vdv/dr \simeq v^2/R_\star$, and requiring it to be smaller than the gravitational acceleration, $GM_\star/R_\star^2$, constrains the outflow velocity v to $v < \sqrt{GM_\star/R_\star}$, i.e., to values below the escape velocity. For a given density ρ in the region of the density inversion, this constrains the mass loss rate to

$$\dot{M} < 4\pi R_\star^2 \rho \sqrt{\frac{GM_\star}{R_\star}} \tag{2.4}$$

for an extended envelope structure not to be affected by mass loss. For $R_\star=R_\odot$, $M_\star=15M_\odot$ and $\rho=10^{-10}$ g cm^{-3}, we get $\dot{M}< 1.6\times10^{-5}M_\odot\mathrm{yr}^{-1}$.

2.5   Discussion

We confirm the findings of Ishii et al. that hydrostatic models of massive and metal-rich helium stars are inflated when mass loss is neglected. In particular, we find the bending of the helium star ZAMS (Z=0.02) towards cooler surface temperatures to occur at the same mass ($15M_\odot$) as Ishii et al. Al lower metallicity (Z=0.001) bending also occurs, but at much higher mass ($100M_\odot$).

This ZAMS bending, which is clearly connected with the inflation phenomenon, has indeed been found earlier. Glatzel et al. (1993), using OPAL opacities, noted this phenomenon in their helium star models. Langer (1989) calculated models of chemically uniform hydrogen-free core helium burning stars using Los Alamos radiative opacities. His helium ZAMS for Z=0.02 indicated bending at about $60M_\odot$, which shows that the inflation phenomenon does not depend only on the iron peak in the OPAL opacities, but that it may also occur for smaller envelope opacities, though only for stars with a larger luminosity-to-mass ratio. The chemically homogeneous, extremely CO-enriched models of Langer (1989) — corresponding to the helium burning terminal age main sequence — showed a bending around $15M_\odot$, likely due to the increase of the Los Alamos opacities with carbon and oxygen abundance. We note further that the inflation phenomenon is not restricted to hydrogen-free stars but occurs also for normal metal-rich ZAMS stars (Schaerer et al. 1993; Glatzel & Kiriakidis 1993; Mowlavi et al. 1998; Stothers & Chin 1999; Ishii et al. 1999).

However, the mass loss rates of luminous, hydrogen-free stars are very high, of the order of $10^{-5}...10^{-4}M_\odot\mathrm{yr}^{-1}$ for the helium stars in mass range considered here (e.g., Nugis & Lamers (2000)). In Sect. 2.4 we showed that mass loss with rates above a critical level (Eq. 3) leads to a reduction or even vanishing of the envelope extension. It is therefore doubtful if, for the case of hydrogen-free stars, the effect of inflation is ever realized in nature. One might argue that an increased metallicity leads to a lower critical mass for the onset of inflation in models without mass loss. But on the other hand, a higher metallicity may also lead to increased mass loss rates (Crowther et al. 2002) which would counteract the effect of a lower critical mass for inflation.

One may also speculate on the effect which the inflation may have on the evolution of the star. Models with an inflated envelope have a very peculiar structure: a hot stellar core covered by an extended, very dilute and almost transparent region which is covered by a rather thin and relatively dense shell. One may wonder about the stability of such a configuration. Glatzel et al. (1993) found that such objects are pulsationally unstable, i.e. even without mass loss, large scale velocity fields may be induced. On the other hand, even moderate radiation induced outflows lead to large velocity gradients due to the low densities obtained in the extended envelopes. This may give rise to large accelerations due to line driving in the CAK model (Castor et al. 1975), which is proportional to the velocity gradient. I.e., an extended

envelope may lead to an increased mass loss, which steepens the velocity gradient (Fig. 2.8) and may enhance the mass loss further. This way, a mass loss instability may be induced. Consequently, the evolutionary time scale of inflated stars may be very short, which could correspond to the fact solar metallicity hydrogen-rich and hydrogen-free stars with masses above the predicted inflation limit (i.e., $\sim 120 M_\odot$ cf. Glatzel & Kiriakidis (1993) and $\sim 15 M_\odot$, Ishii et al. (1999), respectively) are practically absent in our Galaxy.

2.6 Conclusions

Solar metallicity helium stars above $\sim 15 M_\odot$ develop an extended envelope structure if mass loss is neglected. Consequently, their effective temperature decreases and the helium ZAMS bends towards the red in the H-R diagram. At low metallicity this feature does not occur or is shifted to much higher masses.

The occurrence of inflated envelopes is related to the proximity of the stellar luminosity to its effective Eddington luminosity, i.e. to a high luminosity-to-mass ratio or a high envelope opacity. I.e., massive and metal-rich stars are prone to inflation. While the iron opacity peak in the OPAL tables greatly increased the occurrence of inflated envelopes, the phenomenon itself is not dependent only on it.

However, we showed that even in massive, metal-rich stars, inflation is avoided if the stellar wind mass loss rate exceeds a critical value (Eq. 3). Observationally derived mass loss rates of WR stars are at or above the critical value. As furthermore the surfaces of WR stars are not directly observable, it remains possible that inflated envelopes are not present in any of them. On the other hand, inflated envelopes may be unstable and lead to enhanced mass loss. It is remarkable in this context that the critical WR mass loss rate for inflation is close to the observed one (Nugis & Lamers 2000), and that few hydrogen-free stars, if any, can be found above the critical mass for inflation, which is about $15 M_\odot$ for solar metallicity.

Chapter 3

Constraining the mass transfer in massive binaries through progenitor evolution models of Wolf-Rayet+O binaries.

Abstract. Since close WR+O binaries are the result of a strong interaction of both stars in massive close binary systems, they can be used to constrain the highly uncertain mass and angular momentum budget during the major mass transfer phase. We explore the progenitor evolution of the three best suited WR+O binaries HD186943, HD90657 and HD211853, which are characterized by a WR/O mass ratio of $\sim$0.5 and periods of 6..10 days. We are doing so at three different levels of approximation: predicting the massive binary evolution through simple mass loss and angular momentum loss estimates, through full binary evolution models with parametrized mass transfer efficiency, and through binary evolution models including rotation of both components and a physical model which allows to compute mass and angular momentum loss from the binary system as function of time during the mass transfer process. All three methods give consistently the same answers. Our results show that, if these systems formed through stable mass transfer, their initial periods were smaller than their current ones, which implies that mass transfer has started during the core hydrogen burning phase of the initially more massive star. Furthermore, the mass transfer in all three cases must have been highly non-conservative, with on average only $\sim$10% of the transferred mass being retained by the mass receiving star. This result gives support to our system mass and angular momentum loss model, which predicts that, in the considered systems, about 90% of the overflowing matter is expelled by the rapid rotation of the mass receiver close to the Ω-limit, which is reached through the accretion of the remaining 10%.

authors: Jelena Petrovic, Norbert Langer, Karel van der Hucht
Submitted to A&A

3.1 Introduction

The evolution of a star in a binary system can differ significantly from that of an isolated one with the same mass and chemical composition. The physical processes that enter binary evolution are the gravitational and radiation field from the companion, as well as the centrifugal force arising from the rotation of the system. But, most important, it is the evolution of the more massive component that will influence dramatically the evolution of the system. In certain evolutionary phases, mass transfer from one star to another can occur, changing the fundamental properties of both stars as well as their future evolution.

The rotational properties of binary components may play a key role in this respect. The evolution of massive single stars can be strongly influenced by rotation (Heger & Langer 2000; Meynet & Maeder 2000), and evolutionary models of rotating stars are now available for many masses and metallicities. While the treatment of the rotational processes in these models is not yet in a final stage (magnetic dynamo processes are just being included Heger et al. 2004; Maeder & Meynet 2003), they provide first ideas of what rotation can really do to a star. Effects of rotation, as important they are in single stars, can be much stronger in the components of close binary systems: Estimates of the angular momentum gain of the accreting star in mass transferring binaries show that critical rotation may be reached quickly (Packet 1981; Langer et al. 2000; Yoon & Langer 2004b). In order to investigate this, we need binary evolution models which include a detailed treatment of rotation in the stellar interior, as in recent single star models. However, in binaries, tidal processes as well as angular momentum and accretion need to be considered at the same time. Some first such models are now available and are discussed below.

Angular momentum accretion and the subsequent rapid rotation of the mass gainer may be essential for some of the most exciting cosmic phenomena, which may occur exclusively in binaries: Type Ia supernovae, the main producers of iron and cosmic yardstick to measure the accelerated expansion of the universe (Yoon & Langer 2004a,b), and gamma-ray bursts from collapsars, which the most recent stellar models with rotation and magnetic fields preclude to occur in single stars (Petrovic et al. 2004b; Heger et al. 2004; Woosley 2004). For both, the Type Ia supernova progenitors and the gamma-ray burst progenitors, it is essential to understand how efficient the mass transfer process is and on which physical properties it depends. Further exciting astrophysical objects whose understanding is affected by our understanding of mass transfer comprise X-ray binaries (Chevalier & Ilovaisky 1998) and Type Ib and Ic supernovae (Podsiadlowski et al. 1992).

How much matter can stars accrete from a binary companion? As mentioned above, non-magnetic accretion, i.e. accretion via a viscous disk or via ballistic impact, transports angular momentum and can lead to a strong spin-up of the mass gaining star. For disk accretion, it appears plausible that the specific angular momentum

of the accreted matter corresponds to Kepler-rotation at the stellar equator; this leads to a spin-up of the whole star to critical rotation when its initial mass is increased by about 20% (Packet 1981). It appears possible that mass accretion continues in this situation, as viscous processes may transport angular momentum outward through the star, the boundary layer, and the accretion disk (Paczynski 1991). However, as the star is rotating very rapidly, its wind mass loss may dramatically increase (Langer 1997, 1998), which may render the mass transfer process inefficient.

Observations of massive post-mass transfer binary systems constrain this effect. Langer et al. (2003) and Langer et al. (2004) points out that there is evidence for both extremes occurring in massive close binaries, i.e. for quasi-conservative evolution as well as for highly non-conservative evolution. In the present study, we are interested in those binaries that contain a Wolf-Rayet and a main sequence O star. We have chosen to focus on three WN+O systems (HD186943, HD90657 and HD211853) which have similar mass ratios ($\sim$0.5) and orbital periods (6..10 days). As clearly the two stars in these systems must have undergone a strong interaction in the past, an understanding of their progenitor evolution may be the key to constrain the mass transfer efficiency in massive binaries: which fraction of the mass leaving the primary star is accumulated by the secondary star during a mass transfer event?

Evolutionary calculations of massive close binaries were performed by various authors. General ideas about the formation of WR+O binary systems were given by Paczyński (1967), Kippenhahn et al. (1967), van den Heuvel & Heise (1972). Vanbeveren et al. (1979) modelled the evolution of massive Case B binaries with different assumptions for mass and angular momentum loss from the binary system. Vanbeveren (1982) computed evolutionary models of massive close Case B binaries with primary masses between $20M_\odot$ and $160M_\odot$. He concluded that most of the WR primaries are remnants of stars initially larger than $40M_\odot$ and that the accretion efficiency in these systems should be very below 0.3 in order to fit the observations. de Loore & de Greve (1992) computed detailed models of massive Case B binary systems for initial mass ratios of 0.6 and 0.9, assuming an accretion efficiency of 0.5. Wellstein & Langer (1999) and Wellstein et al. (2001) modelled massive binary systems mass range 12..$60M_\odot$ assuming conservative evolution, and Wellstein (2001) presented the first rotating binary evolution models for initial masses of $\sim$15$M_\odot$ and initial mass ratios $q\sim$1.

While it was realized through these models that different mass accretion may be needed to explain different observations, these efforts did not have the potential to explore the physical reasons for non-conservative evolution. I.e., there is no reason to expect that the mass transfer efficiency remains constant during the mass transfer process in a given binary system, nor that its time-averaged value is constant for whole binary populations.

It is not yet known which physical processes can expel matter from a binary system. Vanbeveren (1991) proposed that if a binary component is more massive

then $\sim$40-50$M_\odot$ it will go through an LBV phase of enhanced mass loss, which will prevent the occurrence of RLOF. Dessart et al. (2003) investigated the possibility that radiation pressure from the secondary prevents the accretion. They found that even for moderate mass transfer rates ($5 \cdot 10^{-6} M_\odot \mathrm{yr}^{-1}$) the wind and photon momenta which emerge from the accretion star can not alter the dynamics of the accretion stream. Here, we follow the suggestion that the effective mass accretion rate can be significantly decreased due to the spin-up of the mass receiving star (Wellstein 2001; Langer et al. 2003, 2004; Petrovic & Langer 2004).

The remainder of this paper is organized as follows. In Sect. 3.2 we briefly discuss the observational data available for WR+O binary systems. In Sect. 3.3 we derive estimates for the masses of both stars in WR+O systems for given initial masses and accretion efficiencies. In Sect. 3.4 we present the physics used to compute our detailed evolutionary models. Non-rotating binary evolution models with an adopted constant mass accretion efficiency are presented in Sect. 3.5. Our rotating models in which the mass accretion efficiency is obtained selfconsistently are discussed in Sect. 3.6. We briefly compare our models with observations in Sect. 3.7 and discuss the further evolution of WR+O systems in Sect.˜further. Conclusions are given in Sect. 3.8.

3.2 Observational data

There are about 20 observed Wolf-Rayet+O binary systems with known masses of components in the catalogue of van der Hucht (2001). We have chosen to model three spectroscopic double-lined systems: HD186943 (WN3), HD90657 (WN5) and GP Cep (WN6/WCE)have, since they have similar mass ratios $q = M_{\mathrm{WR}}/M_{\mathrm{O}} \simeq 0.5$ and orbital periods (6..10 days).

WN+O systems that also have short orbital periods are V444 Cyg, CX Cep, CQ Cep, HD94546, HD320102 and HD311884. V444 Cyg has period of 4.2 days and can be result of stable mass transfer evolution, but since mass ratio of this system is $\sim$0.3 we did not include it in this paper. Orbital periods of CX Cep and CQ Cep are very short ($\sim$2 days) and these systems are probably the result of a contact evolution. HD94546 and HD320102 are systems with very low masses of WR and O components ($4M_\odot$+$9M_\odot$ and $2.3M_\odot$+$4.1M_\odot$ respectively) and HD311884 is extremely massive WR+O binary system ($51M_\odot$+$60M_\odot$).

The mass ratio of a binary system is determined from its radial velocity solution, with an error of 5-10%. However, to determine the exact value of the masses of the binary components, the value of the inclination of the system has to be known. Without knowledge of the inclination, only minimum masses of the components can be determined, i.e., $M \sin^3 i$. Massey (1981) determined the minimum mass for the WR star in HD186943 to be 9-11$M_\odot$. Niemela & Moffat (1982) determined the

Table 3.1: Basic parameters of selected WN+O SB2 binaries

	WR 21	WR 127	WR153 [b]
WR number	WR 21	WR 127	WR153 [b]
HD number	HD 90657	HD 186943	HD 211853
spectral type	WN5+O4-6	WN3+O9.5V	WN6/WCE+O3-6I
p (days)	8.2546 ± 0.0001	9.5550	6.6887
e	0.04 ± 0.03	0.07 ± 0.04	$0 + 0$
q	0.52	0.47	0.54
$a \sin i$ ($R_\odot$)	37 ± 3	39 ± 6	> 35.2
$M \sin^3 i$ ($M_\odot$)	8.4	9.3	
i (°)	50 ± 4	55 ± 8	73
M_{WR} ($M_\odot$)	19	17	> 6
M_O ($M_\odot$)	37	36	> 21

Notes:
a: all parameters from compilation of van der Hucht (2001), unless noted otherwise.
b: Demers et al. (2002).

masses of the components of HD90657 in the range 11-14$M_\odot$ for the WN4 component and 21-28$M_\odot$ for the O-type component. The masses of the WR components in HD186943 and HD90657 given in Table 3.1 have been determined by Lamontagne et al. (1996) on the basis of improved values for the inclination of these systems. Demers et al. (2002) determined minimum masses of the components of the system GP Cep. Previously, Lamontagne et al. (1996) suggested values of M_{WR}=15$M_\odot$ and M_O=27$M_\odot$ for this system.

There is no obvious hydrogen contribution in the WR spectrum in any of these systems (Massey 1981; Niemela & Moffat 1982). Massey (1981) showed that hydrogen absorption lines are fairly broad in the spectrum of HD186943, equivalent to vsini$\simeq$250 km s^{-1}, thus the O-type star is rotating much faster then synchronously.

Beside the fact that the binary system GP Cep has a similar mass ratio and period as the other two systems, it has some very different properties as well. The spectral type of the WR component in GP Cep is combination of WN and WC (WN6/WCE Demers et al. 2002). Also, Massey (1981) showed that, next to the main period of ~6.69 days of the binary system GP Cep, radial velocities of absorption lines vary also with a period of 3.4698 days. He proposed that GP Cep is a quadruple system, consisting of two pairs of stars, WR+O and O+O. Panov & Seggewiss (1990) suggested that in both pairs one component is a WR star. However, Demers et al. (2002) showed that there is only one WR star in this quadruple system.

3.3 The simple approach

If the initial binary system is very close (an initial period is of the order of few days), RLOF occurs while the primary is still in the core hydrogen burning phase and Case A mass transfer takes place (fast and slow phase). When the primary expands due to shell hydrogen burning, it fills its Roche lobe and Case AB mass transfer starts. During this mass transfer the primary star loses the major part of its hydrogen envelope. After Case AB mass transfer, the primary is a helium core burning Wolf-Rayet star. During all this time, the secondary is still a main sequence star, but with an increased mass due to mass transfer. When the initial binary period is of the order of one to few weeks, the primary fills its Roche lobe for the first time during shell hydrogen burning and Case B mass transfer takes place. The primary loses most of its hydrogen envelope, becomes a WR star and the secondary is an O star with an increased mass. Case C mass transfer occurs when initial period is of the order of years. The primary fills its Roche lobe during helium shell burning and mass transfer takes place on the dynamical time scale. This scenario is not likely for chosen systems, since some of the secondary stars in WR+O systems have been observed to rotate faster than synchronously. This means that they have accreted some matter which increased their spin angular momentum.

We constructed a simple method to quickly estimate the post-mass transfer parameters for a large number of binary systems for a given accretion efficiency β. This allows us to narrow the space of possible initial parameters (primary mass, secondary mass and orbital period) that allows the evolution into a specific observed WR+O systems.

We considered binary systems with initial primary masses $M_{1,\mathrm{in}}$=25..100M$_\odot$ and secondaries masses $M_{2,\mathrm{in}}$=25/1.7..100M$_\odot$ with an initial period of 3 days. We assumed that the primary is transferring matter to the secondary until it reaches the mass of its initial helium core (Eq. 3.1 below).

Matter that is not accreted on the secondary leaves the system with the specific angular momentum which corresponds to the secondary's orbital angular momentum (King et al. 2001), which is consistent with our approach for mass loss from the binary system (cf. Sect. 3.4). Stellar wind mass loss in neglected.

More massive initial primaries produce more massive WR stars (helium cores) in general, but if the star is in a binary system that goes through mass transfer during hydrogen core burning of the primary (Case A), this depends also on other parameters:
-If the initial period is longer, mass transfer starts later in the primary evolution and the initial helium core of the primary is more massive.
-If the initial mass ratio is further from unity, the mass transfer rate from the primary reaches higher values and the initial helium core mass is smaller.

We initially want to restrict ourselves to systems that undergo stable mass trans-

fer, i.e. avoid contact situations. Wellstein et al. (2001) found that the limiting initial mass ratio for conservative Case A binary system is $M_{1,\text{in}}/M_{2,\text{in}} \sim 1.55$ and for conservative Case B systems ~ 1.25. Since we allow non-conservative evolution, we consider initial mass ratio $q \leq 1.7$ for Case A and $q \leq 1.4$ for Case B. The observed WR+O systems (HD186943, HD90657 and HD211853) all have very short orbital periods, between 6 and 10 days. Since, the net effect of the Case A+Case AB, or Case B is a widening of the orbit (if there is no contact), we have to assume that the initial periods need to be shorter than, or approximatively equal to the observed ones. We adopted a minimum initial orbital period of 3 days to avoid that the primary fills its Roche lobe on the ZAMS.

We estimated the minimum initial helium core masses, which are obtained by the earliest Case A systems, for systems with a mass ratio of $M_{1,\text{in}}/M_{2,\text{in}}=1.7$ and an initial period of 3 days ($M_{1,\text{in}} \gtrsim 41 M_\odot$) from the detailed evolutionary models shown later in this paper (Sect. 3.5):

$$M_{\text{WR,in}} = 0.24 * M_{1,\text{in}} + 0.27. \qquad (3.1)$$

In this linear approximation, we neglected the influence of the initial mass ratio on the initial WR mass. It is shown in Sect. 3.5.2 that this dependence becomes important only for initial mass ratios above $q \simeq 2$.

For Case B binaries, the initial WR mass does not depend on the initial period and the initial mass ratio of the system, since during core hydrogen burning, the primary evolves as a single star, without any interaction with the secondary. We estimated the relation between initial main sequence mass and initial WR mass as a linear fit from the Case B binary systems with initial primaries $M_{1,\text{in}} \gtrsim 18 M_\odot$ (Wellstein & Langer 1999):

$$M_{\text{WR,in}} = 0.53 * M_{1,\text{in}} - 4.92. \qquad (3.2)$$

The minimum initial period for a system to evolve through Case B mass transfer depends on the initial primary mass and the mass ratio. We can estimate, based on the radii of the primaries at the end of the main sequence evolution, what would be the initial orbital separation necessary to avoid the primary filling its Roche lobe before shell hydrogen burning. From Kepler's law follows that the orbital separation is proportional to the mass ratio $a \sim q^{-1/3}$ and the initial primary mass $a \sim M_1^{1/3}$. Since $q \sim 1$ we can neglect this dependence and estimate the initial period for which the radius of the primary at the end of MS is equal to its Roche radius. For this estimate we do not take into account stellar wind that will widen the orbit and decrease the masses. We conclude that the Case B limiting initial orbital period for $40 M_\odot$ is ~ 10 days, for $45 M_\odot \sim 15$ days and for $75 M_\odot \sim 30$ days. Since the result of stable Case B mass transfer is widening of the orbit, it follows that (stable mass transfer) Case B binary systems can not be progenitors of the observed systems HD186943, HD90657 and HD211853 whose orbital periods are shorter than 10 days. However, WR star

masses resulting from Case B evolution are practically the same as those from very late Case A evolution, which is still considered in our analysis.

We calculate binary systems for early Case A (p_{in}=3 days) and for late Case A ($p_{in} \approx p_{limit}$).

The results are shown in Fig. 3.1 for four different accretion efficiencies (β=0.0, 0.1, 0.5, 1.0 respectively) for early Case A evolution (p=3 days). Fig. 3.2 shows the results for early Case A systems (p=3 days) for all values of β=0..1 and for Case B/late Case A, also for all β.

We notice from Fig. 3.1, that when the assumed β is larger, the resulting WR+O systems lie further from the line defined by q=0.5. The reason is clear: if the accretion efficiency is higher, the secondary will become more massive while the initial mass of the WR star stays the same. Conservative evolution (Fig. 3.1d) produces WR+O systems that have small mass ratios, q=1/5..1/6.

We conclude that if the considered three observed WR+O binary systems evolved through a stable mass transfer, a large amount of matter must have left the system. On the other hand, since some of the secondary stars in WR+O binaries have been observed to rotate faster than synchronously (Massey 1981; Underhill et al. 1988), a certain amount of accretion may be required.

Fig. 3.2 shows the resulting WR+O masses in Case A and Case B (latest Case A) for accretion efficiency β=0..1. If the primary star does not lose mass in a mass transfer during core hydrogen burning ($p_{in} \geq p_{limit}$), it will form a more massive WR star, as we already explained. There will be less mass to transfer from the primary to the secondary, and for fixed β the corresponding O star will become less massive. However, since the observed periods of HD186943, HD90657 and HD211853 are shorter than 10 days and Case A+Case AB widens the binary orbit, the initial orbital period should be shorter than observed, so we can conclude roughly that p_{in} is between 3 and 10 days.

The orbital period of WR+O systems depend on their initial orbital period, their initial mass ratio and on the parameter β. If the initial period increases and there is no contact during the evolution, the orbital period in the WR+O stage will also increase. However, the orbital period of WR+O systems will be shorter if the initial mass ratio is larger. If the initial masses are very similar, the primary will become less massive than the secondary very early during the mass transfer, and afterward matter is transferred from the less to the more massive star, which results in a widening of the orbit. Conversely, the final period is shorter for a larger difference in initial masses in the binary system.

We can draw the following conclusions:

-The accretion efficiency during the major mass transfer phase in the progenitor evolution of the three observed WR+O binaries is small, i.e. β=0..0.1, as for larger β the O stars during the WR+O phase are more massive and the WR/O-mass rations smaller than observed. However, we note that it is unlikely that the secondaries
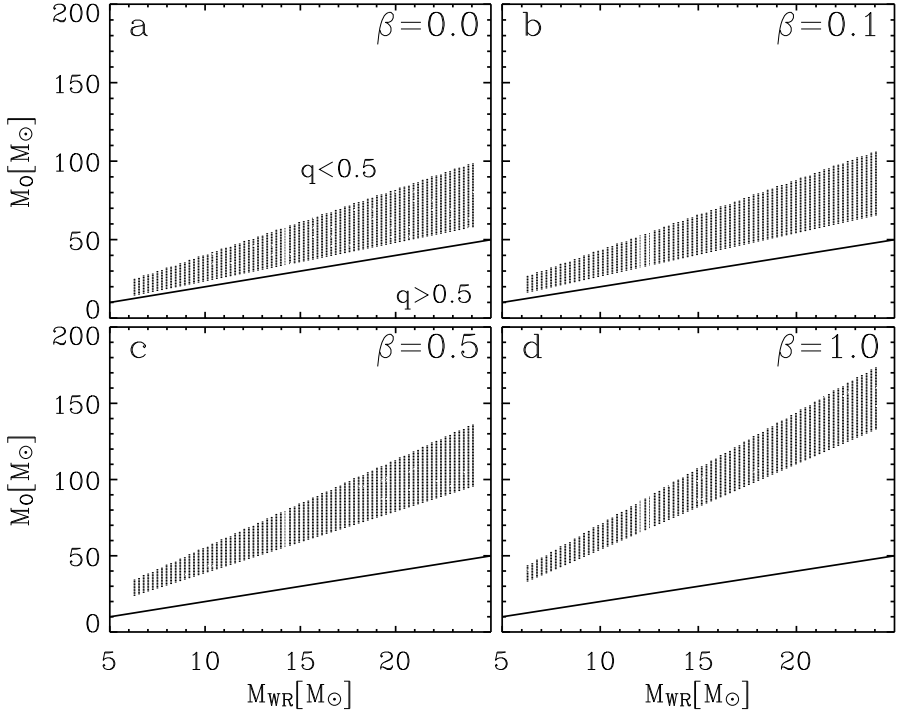
Figure 3.1: Masses of both components of post-Case A mass transfer WR+O binary systems resulting from our simple approach, for initial primary masses in the range 25..100$M_\odot$ and an initial period of p_{in}=3 days, for four different assumed accretion efficiencies β (a-d). The solid line represents a mass ratio of $q=M_{WR}/M_O$=0.5. For an increasing β, the O stars in WR+O systems become more massive and the WR/O-mass ratio decreases.

did not accrete at all (β=0), since some O stars are found to rotate faster than synchronously.

-The initial orbital period needs to be larger than $\sim$3 days, to avoid contact at the beginning of hydrogen burning.

-The initial orbital period should be larger than $\sim$3 days, in order to obtain massive enough WR stars.

-The initial orbital periods should be shorter than the observed orbital periods in the three WR+O systems, i.e. shorter than $\sim$10 days. This excludes Case B mass transfer.

-While the initial mass ratio $M_{1,in}/M_{2,in}$ should not be too far from unity so contact is avoided, it should be close to the contact limit, since this leads to the shortest orbital periods and largest WR/O mass ratios in WR+O systems, as needed for the
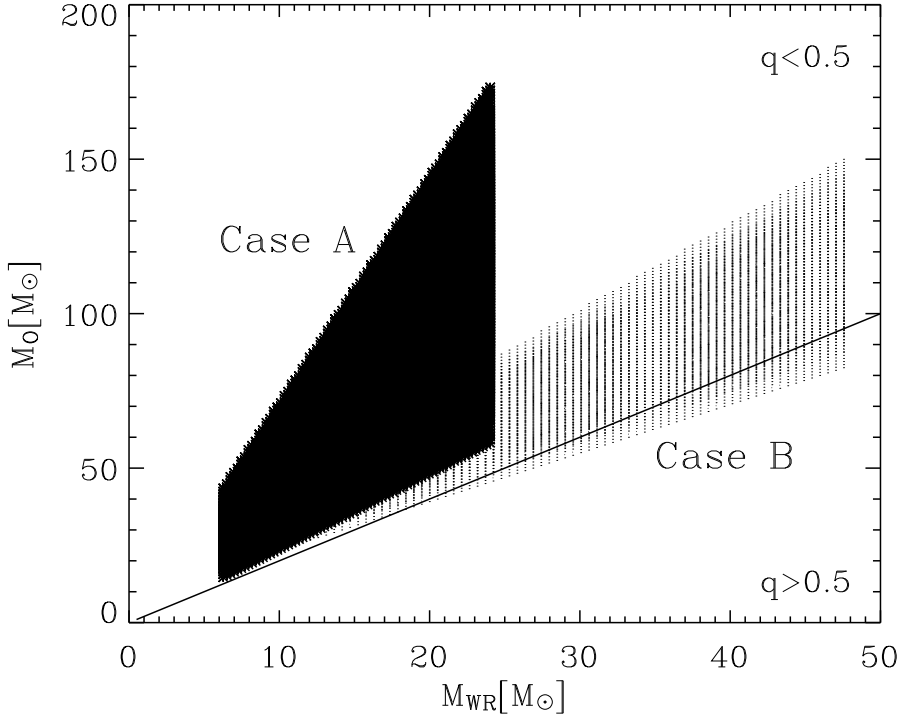
Figure 3.2: Masses of both components of post-Case A mass transfer WR+O binary systems resulting from our simple approach, for initial primary masses in the range 25..100$M_\odot$ and for early (p_{in}=3 days) Case A and late Case A respective Case B evolution. The assumed accretion efficiency is β=0..1. The solid line represents a mass ratio of $q=M_{\mathrm{WR}}/M_{\mathrm{O}}$=0.5.

three observed systems.

3.4   Numerical code and physical assumptions

We showed in Sect. 3.3 that we can roughly estimate the parameters of the progenitor systems of observed WR+O binaries HD186943, HD90657 and HD211853. However, detailed numerical models are required in order to verify that the assumption of contact-free evolution can in fact be justified. And finally, we want to check whether the required mass and angular momentum loss can be reproduced by our detailed selfconsistent approach.

We are using a binary evolutionary code which was originally developed by Braun (1998) on the basis of an implicit hydrodynamic stellar evolution code for

single stars (Langer 1991, 1998). It calculates simultaneous evolution of the two stellar components of a binary system in a circular orbit and the mass transfer within the Roche approximation (Kopal 1978). Mass loss from the Roche lobe filling component through the first Lagrangian point is given by Ritter (1988) as:

$$\dot{M} = \dot{M}_0 \exp(R - R_l)/H_p \qquad (3.3)$$

with $\dot{M}_0 = \rho v_s Q/\sqrt{e}$, where H_p is the photospheric pressure scale height, ρ is the density, v_s the velocity of sound and Q the effective cross-section of the stream through the first Lagrangian point according to Meyer & Meyer-Hofmeister (1983).

Stellar wind mass loss for O stars on the main sequence is calculated according to Kudritzki et al. (1989). For hydrogen-poor stars ($X_s < 0.4$) we assume mass loss based on the empirical mass loss rates for Wolf-Rayet stars derived by Hamann et al. (1995):

$$\log(\dot{M}_{WR}/M_\odot yr^{-1}) = -11.95 + 1.5 \log L/L_\odot - 2.85 X_s. \qquad (3.4)$$

Since Hamann & Koesterke (1998) suggested that these mass loss rates may be overestimated, we calculated evolutionary models with mass loss rate given by Eq. 3.4 multiplied by factors 1/2, 1/3 and 1/6.

The treatment of a convection and a semiconvection which is applied here is described in Langer (1991) and Braun & Langer (1995). Changes in chemical composition are computed using a nuclear network including pp chains, the CNO-cycle, and the major helium, carbon, neon and oxygen burning reactions. More details are given in Wellstein & Langer (1999) and Wellstein et al. (2001). We use the OPAL Rosseland-mean opacities of (Iglesias & Rogers 1996). For all models, a metallicity of $Z = 0.02$ is adopted. The abundance ratios of the isotopes for a given element are chosen to have the solar meteoritic abundance ratios according to Grevesse & Noels (1993). The change of the orbital period (orbital angular momentum loss) due to the mass transfer and stellar wind mass loss is computed according to Podsiadlowski et al. (1992), with the specific angular momentum of the stellar wind material calculated by Brookshaw & Tavani (1993).

The influence of the centrifugal force in the rotating models is implemented according to Kippenhahn & Thomas (1970). The stellar spin vectors are assumed to be perpendicular to the orbital plane. Synchronization due to tidal spin-orbit coupling is included with a time scale given by Zahn (1977). Rotationally enhanced mass loss is included as follows:

$$\dot{M}/\dot{M}(v_{rot} = 0) = 1/(1 - \Omega)^\xi, \qquad (3.5)$$

where $\Omega = v_{rot}/v_{crit}$ and $v_{crit}^2 = GM(1 - \Gamma)/R$ with $\Gamma = L/L_{Edd} = \kappa L/(4\pi cGM)$ is Eddington factor, G is gravitational constant, M is mass, R radius, κ opacity, v_{rot} rotating velocity and v_{crit} critical rotational velocity (Langer 1998). The specific

angular momentum of the accreted matter is determined by integrating the equation of motion of a test particle in the Roche potential in case the accretion stream impacts directly on the secondary star, and is assumed Keplerian otherwise Wellstein (2001). Rotationally induced mixing processes and angular momentum transport through stellar interior are described by Heger et al. (2000a). Magnetic fields generated due to differential rotation in the stellar interior (Spruit 2002) are not included here (however, see Petrovic et al. 2004b).

We calculated the evolution of the binary systems in detail until Case AB mass transfer starts. Then we estimated the outcome of this mass transfer by assuming that it ends when WR star has $\sim$5% of the hydrogen left at the surface. For this purpose we calculate the Kelvin-Helmholtz time scale of the primary:

$$t_{\mathrm{KH}} = 2 \cdot 10^7 M_1{}^2 / (L_1 R_{\mathrm{l1}}) yr \qquad (3.6)$$

where M_1, L_1 and R_{l1} are mass, luminosity and Roche radius (in Solar units) of the primary star at the onset of Case AB mass transfer. The Mass transfer rate is then assumed as:

$$\dot{M}_{\mathrm{tr}} = (M_1 - M_{\mathrm{WR,in}}) / t_{\mathrm{KH}} \qquad (3.7)$$

where $M_{\mathrm{WR,in}}$ is the mass of the WR star that has a hydrogen surface abundance of 5%; all quantities are taken at the beginning of the mass transfer. We calculate the change of the orbital period orbit using constant value of β=0.1 for non-rotating and β=0.0 for rotating models (Wellstein 2001). Matter that is not retained by the secondary is assumed to leave the system with a specific angular momentum which corresponds to the secondary's orbital angular momentum (King et al. 2001).

3.5 Non-rotating models

We concluded in Sect. 3.3 that massive O+O binaries can result in WR+O systems similar to observed the (HD186943, HD90657 and HD211853) if accretion efficiency β is low. Since some O stars in WR+O binaries have been observed to rotate faster than synchronously, we concluded that β>0.0 and assumed a constant value of β=0.1 in our detailed evolutionary models. We already mentioned that the orbital periods of the observed systems are between 6 and 10 days. Since the net effect of Case A+Case AB mass transfer is a widening of the orbit, the initial periods should be shorter than the observed ones, so we modelled binary systems with initial orbital periods of 3 and 6 days.

We chose initial primary masses to be in the range 41..75M$_\odot$. The masses of the secondaries are chosen so that the initial mass ratio ($M_{1,\mathrm{in}}/M_{2,\mathrm{in}}$) is $q\approx$1.7-2.0. An initial mass ratio of $\sim$1.55 is estimated to be the limiting value for the occurrence of contact between the components in Case A systems by Wellstein et al. (2001) for conservative mass transfer. Contact occurs when the accretion time scale of the

Table 3.2: Non-rotating WR+O progenitor models for β=0.1. N is the number of the model, $M_{1,\text{in}}$ and $M_{2,\text{in}}$ are initial masses of the primary and the secondary, p_{in} is the initial orbital period and q_{in} is the initial mass ratio of the binary system. t_A is time when Case A mass transfer starts, Δt_f is the duration of the fast phase of Case A mass transfer, $\dot{M}_{\text{tr}}^{\max}$ is the maximum mass transfer rate, $\Delta M_{1,f}$ and $\Delta M_{2,f}$ are mass loss of the primary and mass gain of the secondary (respectively) during fast Case A, Δt_s is the duration of slow Case A mass transfer, $\Delta M_{1,s}$ and $\Delta M_{2,s}$ are mass loss of the primary and mass gain of the secondary (respectively) during the slow Case A, p_{AB} is the orbital period at the onset of Case AB, $\Delta M_{1,\text{AB}}$ is the mass loss of the primary during Case AB (mass gain of the secondary is 1/10 of this, see Sect. 3.4), $M_{\text{WR},5}$ is the WR mass when the hydrogen surface abundance is X_s=0.05, the WR mass at $X_s \leq 0.01$ is given in brackets, M_O is the mass of the corresponding O star, q is the mass ratio M_{WR}/M_O, and p is the orbital period of the WR+O system. The models are computed with a stellar wind mass loss of Hamann/6, except * Hamann/3,** Hamann/2. ^{c} indicates a contact phase that occurs for low masses due to a mass ratio too far from unity, for high masses due to the secondary expansion during slow phase of Case A.

Nr	$M_{1,\text{in}}$	$M_{2,\text{in}}$	p_{in}	q_{in}	t_A	Δt_f	$\dot{M}_{\text{tr}}^{\max}$	$\Delta M_{1,f}$	$\Delta M_{2,f}$	Δt_s	$\Delta M_{1,s}$	$\Delta M_{2,s}$	p_{AB}	$\Delta M_{1,\text{AB}}$	$M_{\text{WR},5}(1)$	M_O	q	p
	$M_\odot$	$M_\odot$	d		10^6yr	10^4yr	$M_\odot$/yr	$M_\odot$	$M_\odot$	10^6yr	$M_\odot$	$M_\odot$	d	$M_\odot$	$M_\odot$	$M_\odot$		d
$N1$	41	20	3	2.05	2.8	c	—	—	—	—	—	—	—	—	—	—	—	—
$N2$	41	20	6	2.05	3.6	3.9	5.4	18.82	1.85	0.39	0.97	0.06	5.9	7.1	11.8(11.2)	22.5	0.52	12.6
$N3$	41	20.5	3	2.00	2.8	2.2	18.0	21.13	2.11	—	—	—	2.85	8.17	7.7(7.2)	23.2	0.33	12.5
$N4$	41	24	3	1.71	2.8	3.1	3.6	15.18	1.51	1.51	5.13	0.20	3.87	9.05	10.1(9.3)	26.4	0.38	13.5
$N5$	41	24	6	1.71	3.6	4.3	3.2	17.31	1.72	0.42	1.88	0.09	8.92	7.53	12.1(11.4)	26.3	0.46	21.5
$N6$	41	27	3	1.52	2.75	5.8	1.9	13.82	1.37	1.51	5.86	0.17	4.38	9.59	10.3(9.8)	29.1	0.35	16.6
$N7$	41	30	3	1.37	2.7	6.7	1.1	12.60	1.24	1.51	6.72	0.08	5.20	9.76	10.5(10.0)	31.8	0.33	20.8
$N8$	45	27	3	1.67	2.5	3.6	3.3	15.41	1.53	1.57	7.48	0.25	3.88	8.81	11.5(10.7)	29.4	0.39	12.0
$N9$	56	33	3	1.70	1.9	5.0	4.1	17.2	1.70	1.86	15.66	0.44	4.07	7.14	13.6(12.7)	35.4	0.38	9.8
$N10$	56	33	6	1.70	2.8	5.8	3.1	19.35	1.9	0.60	4.77	0.02	7.77	9.18	18.6(17.5)	35.1	0.53	15.2
$N11^*$	56	33	6	1.70	2.8	5.8	3.1	19.35	1.9	0.46	3.63	0.06	7.91	7.15	18.6(17.2)	34.9	0.53	13.8
$N12^{**}$	56	33	6	1.70	2.8	5.8	3.1	19.35	1.9	0.43	3.43	0.07	8.89	3.5	18.3(16.4)	34.5	0.53	12.1
$N13$	65	37	3	1.76	1.6	3.2	4.7	18.81	1.87	c	—	—	—	—	16.2(14.8)	—	—	—
$N14$	75	45	3	1.67	1.3	4.2	3.1	18.57	1.79	c	—	—	—	—	18.5(16.9)	—	—	—

secondary ($\dot{M}_{2,\text{acc}}/M_2$) is much longer than the thermal (Kelvin-Helmholtz) time scale of the primary ($\dot{M}=M_1/t_{\text{KH}}$), so the secondary expands and fills its Roche lobe. In our models, only 10% of matter lost by the primary is accreted on the secondary star, so it reaches hydrostatic equilibrium faster and expands less than in the case of larger β. This is the reason why we adopted a weaker condition for contact formation and calculate models with mass ratios $q\approx1.7..2.0$.

All modelled systems (except the ones that enter contact) go through Case A and Case AB mass transfer. Details of the evolution of all calculated binary systems are given in Table 3.2. We discuss the details of the binary evolution taking the system number 11 as an example. Fig. 3.3 shows the evolutionary tracks of the primary and the secondary in the HR diagram until the onset of Case AB mass transfer. This system begins its evolution with the initial parameters $M_{1,\text{in}}=56\text{M}_\odot$, $M_{2,\text{in}}=33\text{M}_\odot$, $p_{\text{in}}=6$ days. Both stars are core hydrogen burning stars (dashed line, Fig. 3.3), but since the primary is more massive, it evolves faster and fills its Roche lobe, so the system enters Case A mass transfer (solid line, Fig. 3.3) $\sim5.6\cdot10^6$ years after the beginning of core hydrogen burning. The first phase of Case A is fast process and takes place on the Kelvin-Helmholtz (thermal) time scale ($\sim3.1\cdot10^4$ years). The primary loses matter quickly and continuously with a high mass transfer rate ($\dot{M}_{\text{tr}}^{\text{max}}\sim3.1\cdot10^{-3}\text{M}_\odot\text{yr}^{-1}$). In order to retain hydrostatic equilibrium, the envelope expands, which requires energy and causes a decrease in luminosity (Fig. 3.3). At the same time the secondary is accreting matter and is expanding. Due to this, its luminosity increases and the effective temperature decreases (Fig. 3.3). During fast phase of Case A mass transfer the primary loses $\sim19\text{M}_\odot$ and the secondary accretes 1/10 of that matter. After the fast process of mass transfer, the primary is still burning hydrogen in its core and is still expanding, so slow phase of Case A mass transfer takes place on a nuclear time scale ($0.46\cdot10^6$ years) with a mass transfer rate of $\dot{M}_{\text{tr}}\sim10^{-6}\text{M}_\odot\text{yr}^{-1}$. After this, the primary is the less massive star, with decreased hydrogen surface abundance. Stellar wind mass loss of the primary increases when its surface becomes hydrogen poor ($X_{\text{s}}<0.4$). At the end of core hydrogen burning the primary contracts (effective temperature increases) and thus RLOF stops (Fig. 3.3 dotted line). When the primary starts shell hydrogen burning it expands (dash-dotted line, Fig. 3.3), fills its Roche lobe and Case AB mass transfer starts.

Fig. 3.4 and Fig. 3.5 show the evolution of the interior of the primary and the secondary until Case AB mass transfer. The primary loses huge amounts of matter during fast Case A mass transfer and its convective core becomes less than a half of its original mass. At the same time, the secondary accretes matter from the primary and the heavier elements are being relocated by thermohaline mixing. In Fig. 3.6 and Fig. 3.7 we see the mass transfer rate and the surface abundances of hydrogen, carbon, nitrogen and oxygen. The primary is losing matter and the surface abundances of hydrogen and nitrogen decrease. On the other hand, surface abundances of carbon and oxygen increase. The secondary is accreting material from the primary and its
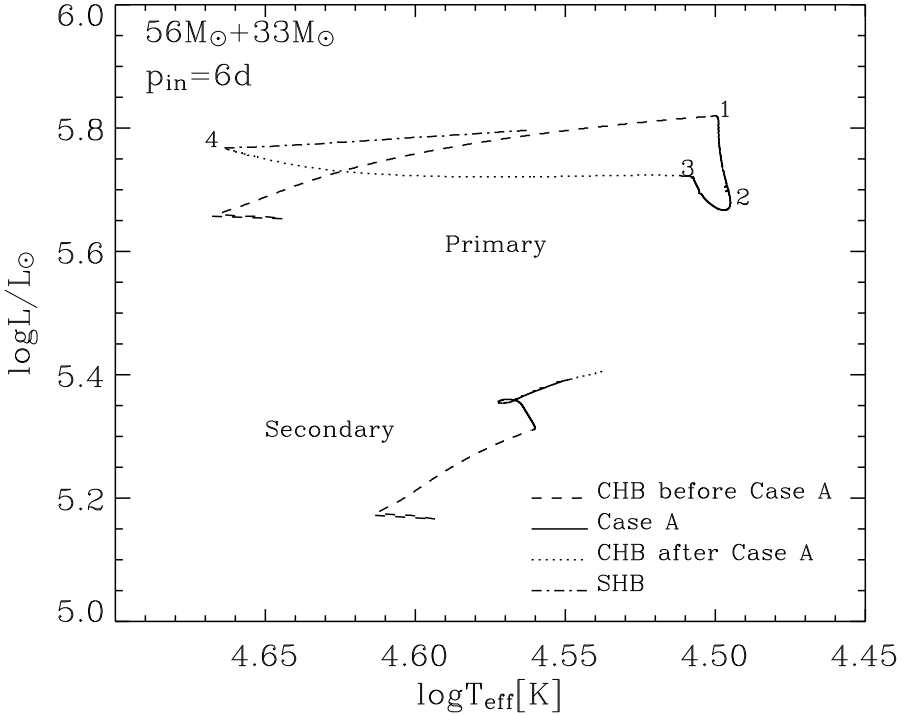
Figure 3.3: HR diagram of the initial system $M_{1,in}$=56M$_\odot$, $M_{2,in}$=33M$_\odot$, p_{in}=6 days. Both stars are core hydrogen burning (dashed line) until Case A mass transfer starts (solid line). The primary is losing mass and its luminosity and effective temperature decrease. At the same time the secondary is accreting matter and expanding, becoming more luminous and cooler. After Case A mass transfer is finished, the primary is losing mass by stellar wind and contracting at the end of core hydrogen burning (dotted line). After this the primary starts with shell hydrogen burning and expands (dash-dotted line).

surface abundances of hydrogen, carbon and oxygen decrease, while the nitrogen abundance increases.

During Case AB mass transfer the primary star loses the major part of its hydrogen envelope. After Case AB mass transfer, the primary is a helium core burning star (WR) and the secondary is still a core hydrogen burning O star. The masses of the modelled WR stars are in the range from ∼8..18.5M$_\odot$ The orbital periods of the modelled WR+O systems vary from ∼9.5 to ∼20 days, and the mass ratios are between 0.33 and 0.53.
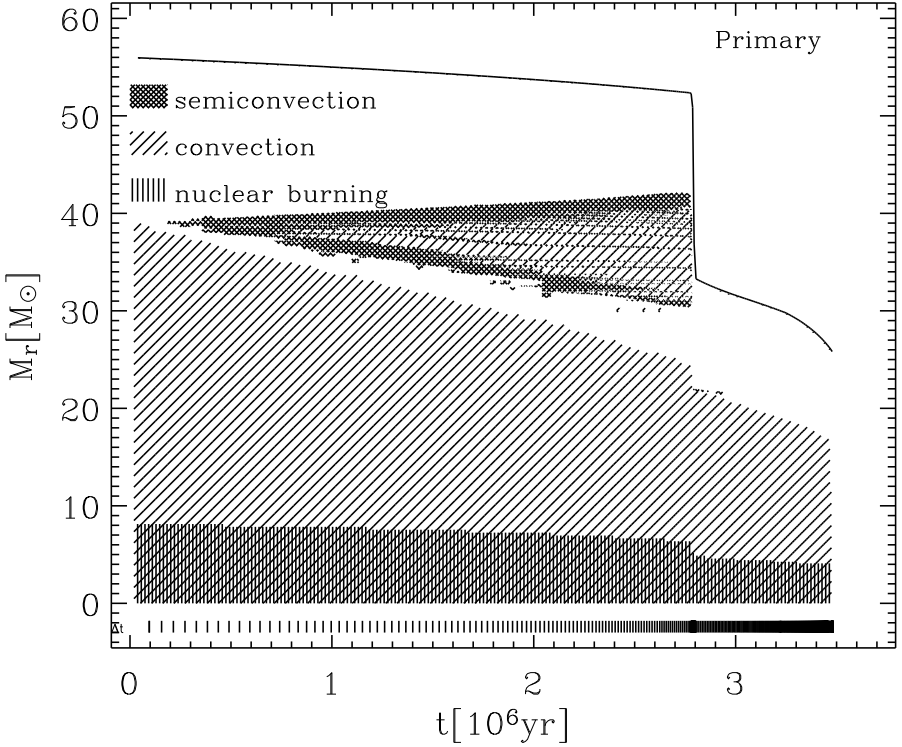
Figure 3.4: The evolution of the internal structure of the $56M_\odot$ primary during the core hydrogen burning. Convection is indicated with diagonal hatching and semiconvection with crossed hatching. The hatched area at the bottom indicates nuclear burning. The topmost solid line corresponds to the surface of the star.

3.5.1 Relation between initial and WR mass

The initial mass of helium core of the primary in the binary system depends on a few parameters: initial primary mass, initial period, initial mass ratio and stellar wind mass loss rate. If the primary loses matter due to the mass transfer or stellar wind during core hydrogen burning, it will form a helium core that is less massive than if there was no mass loss. If the initial period is very short, Case A mass transfer will take place very early in the evolution of the primary, so the star will not have time to develop a larger core before it starts losing mass due to Roche lobe overflow. If the initial mass ratio ($q=M_{1,in}/M_{2,in}$) increases, the mass transfer rate from the primary star increases too and this results in less massive primaries that will evolve into less massive WR stars.

In our models the primary starts losing mass by stellar wind as WR star when its
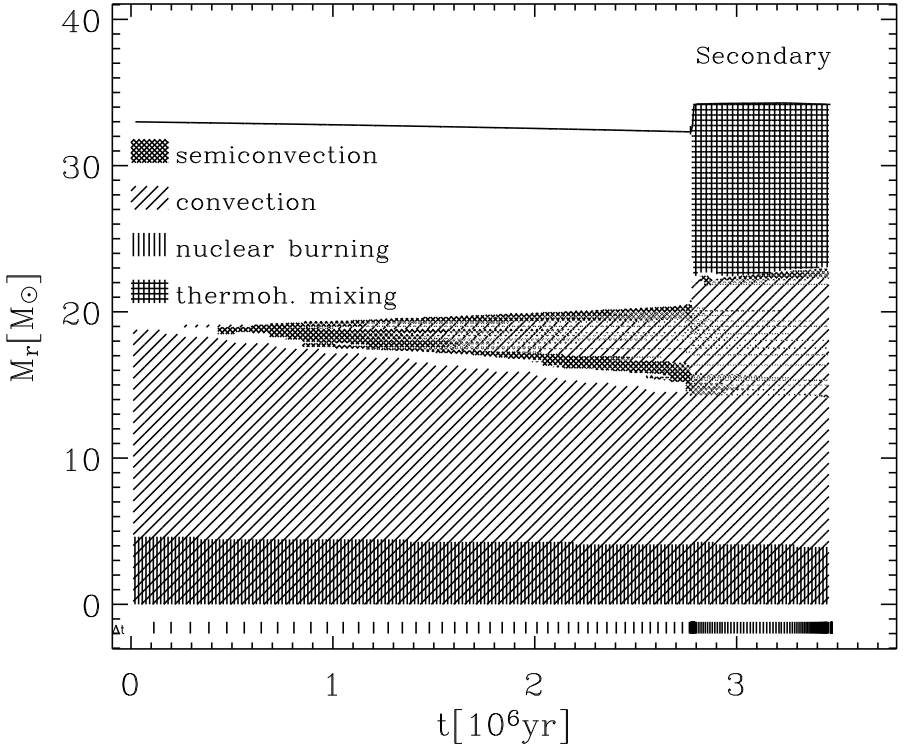
Figure 3.5: The evolution of the internal structure of the $33M_\odot$ secondary during core hydrogen burning of the primary. Convection is indicated with diagonal hatching, semiconvection with crossed hatching and thermohaline mixing with straight crossed hatching. The hatched area at the bottom indicates nuclear burning. The topmost solid line corresponds to the surface of the star.

hydrogen surface abundance goes below X_s=0.4. However, the observed WR stars in HD186943, HD90657 and HD211853 do not have obvious hydrogen on the surface, so we assume that these WR stars are the result of Case AB mass transfer, with a hydrogen surface abundance of $X_s \approx 0.05$. We also calculated the corresponding WR masses with $X_s \leq 0.01$. We plotted in Fig. 3.8 the initial WR masses (X_s=0.05 and $X_s \leq 0.01$) versus the initial primary (progenitor) masses. With 'star' symbols we indicated WR stars that originate from binary systems with an initial mass ratio of $q \approx 1.7$ and an initial period $p = 3$ days (Table 3.2: N 4, 8, 9, 13, 14). Large 'star' symbols represent WR stars with 5% of hydrogen at the surface and small symbols indicate WR stars that have a hydrogen surface abundance of less than 1%.

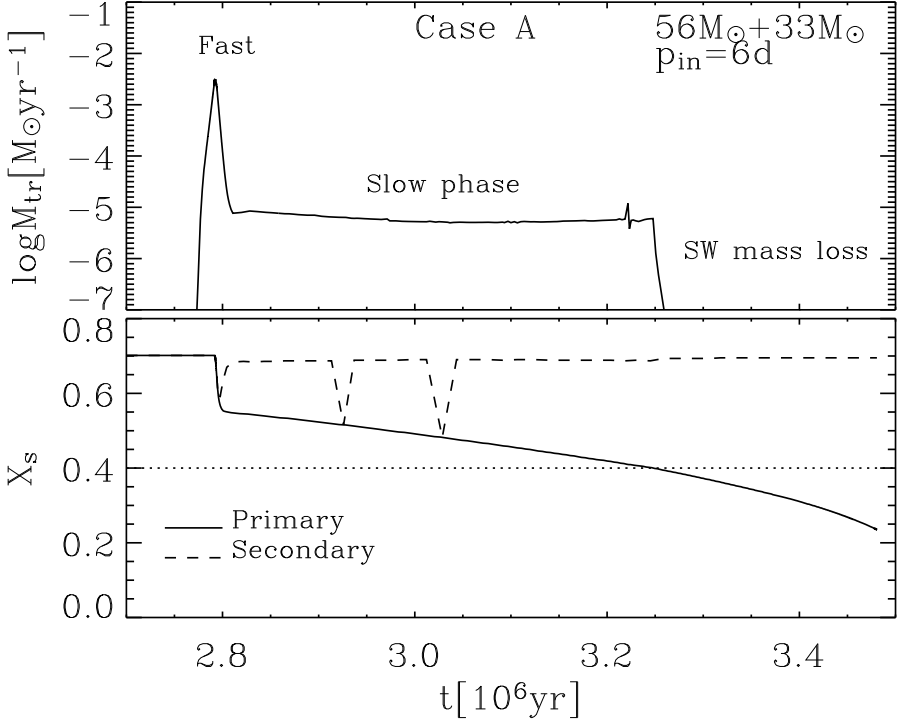We derive a relation between the initial primary mass and the initial WR mass

Figure 3.6: Upper plot: Mass transfer rate during Case A mass transfer in the binary system with $M_{1,in}$=56M⊙, $M_{2,in}$=33M⊙, p_{in}=6days. Lower plot: The hydrogen surface abundance of the primary (solid line) is decreasing during mass transfer and further due to stellar wind mass loss. The secondary (dashed line) recovered its original surface hydrogen abundance through thermohaline mixing. The primary starts losing mass with WR stellar wind mass loss when its hydrogen surface abundance falls beneath X_s=0.4, represented by the dotted line.

(derived as a linear fit) for p=3 days and $q \approx 1.7$, (X_s=0.05):

$$M_{WR} = 0.24 * M_{1,in} + 0.27. \tag{3.8}$$

We use this relation to estimate the initial parameters of the possible progenitors of the observed WR+O binary systems, as already explained in Sect. 3.3. In the same way, the relation between the initial primary mass and the initial WR mass (X_s<0.01) for the same systems is:

$$M_{WR} = 0.22 * M_{1,in} + 0.56. \tag{3.9}$$

We also show in Fig. 3.8 the initial WR masses (X_s=0.05 for binary systems N 5, 10, 11, 12, Table 3.2) for an initial mass ratio of ∼1.7 and an initial orbital period
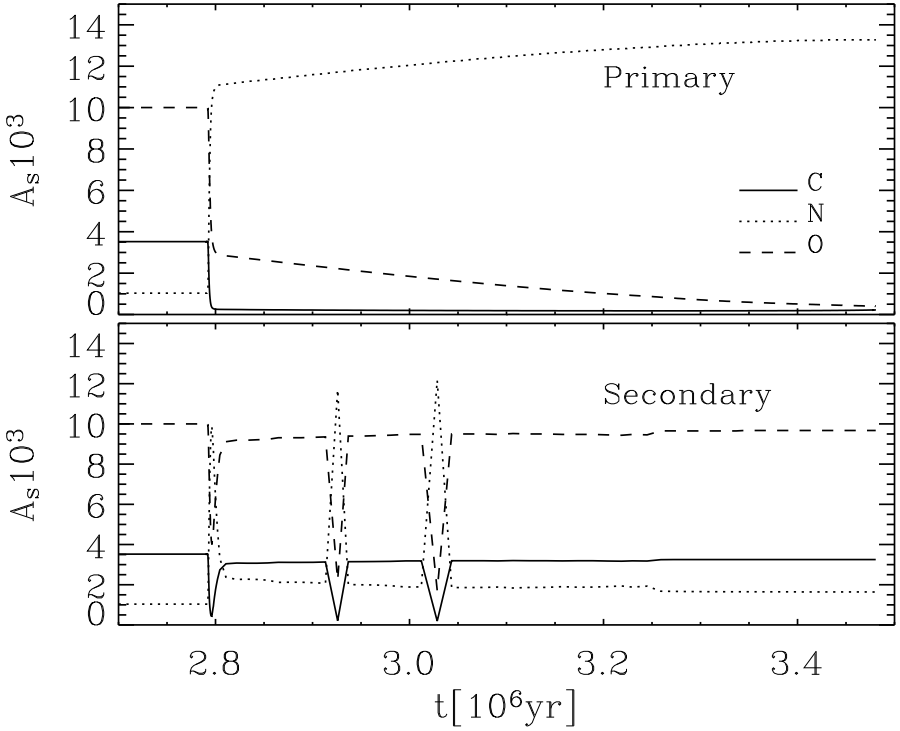
Figure 3.7: Surface abundance of carbon (solid line), nitrogen (dotted line) and oxygen (dashed line) of the primary (upper plot) and the secondary (lower plot) in the system with $M_{1,in}=56M_\odot$, $M_{2,in}=33M_\odot$, $p_{in}=6$ days.

of 6 days (diamond symbols). We notice that the resulting WR masses are higher than the ones that come out from systems with an initial orbital period of 3 days (see Sect. 3.5.3). Different 'diamond' symbols for the initial primary $56M_\odot$ are for different mass loss rates (see Sect. 3.5.4). Triangle symbols in Fig. 3.8 show the initial WR masses for constant initial primary mass, $M_{1,in}=41M_\odot$, but for different initial mass ratios (see Sect. 3.5.2)

Note that the WR masses that are the result of early Case A progenitor evolution are significantly lower than ones that are the result of Case B evolution (Wellstein & Langer 1999), because of the mass transfer from the primary during the core hydrogen burning phase.
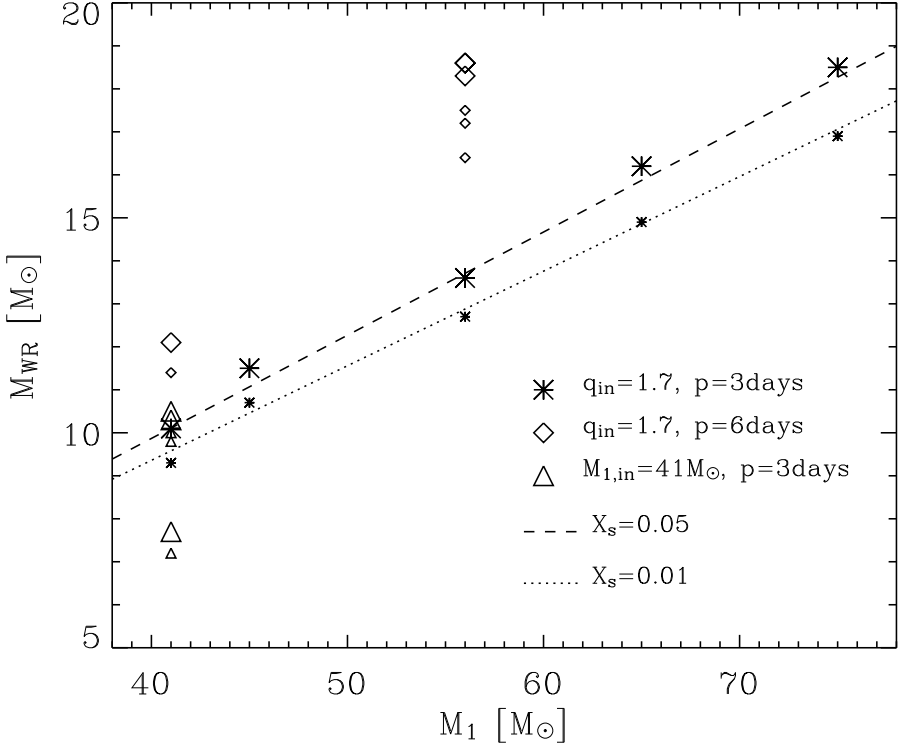
Figure 3.8: Initial WR mass as a function of initial (progenitor) mass. Large and small symbols indicate WR stars with hydrogen surface abundance of X_s=0.05 and $X_s \leq$0.01, respectively. Systems with an initial orbital period of p_{in}=3 days and a mass ratio of $q \sim$1.7 are indicated with star symbols, systems with an initial period of 6 days and $q \sim$1.7 with diamond symbols, systems with an initial primary 41$M_\odot$ and initial period of 3 days with triangle symbols. The dashed line represents a linear fit for systems with an initial period of 3 days and with X_s=0.05, and the dotted line represents linear fit for systems with an initial period of 3 days and $X_s \leq$0.01.

3.5.2   Influence of the initial mass ratio on the WR mass and orbital period

During the mass transfer phase, the mass transfer rate increases roughly until the masses of both components are equal. The maximum mass transfer rate during Case A increases with the increase of the initial mass ratio ($M_{1,in}/M_{2,in}$) and the resulting WR star is less massive. To analyse the influence of the initial mass ratio on the evolution of the binary system, we compared systems with an initial primary mass of $M_{1,in}$=41$M_\odot$, an initial orbital period of p_{in}=3 days for five different initial mass ratios: 2.05, 2.00, 1.71, 1.52 and 1.37. (Table 3.2 N 1, 3, 4, 6, 7, Fig. 3.9).

The system with q_{in}=2.05 enters contact during fast Case A mass transfer. The mass transfer rate in this case is very high ($\dot{M}\approx6\cdot10^{-2}M_\odot yr^{-1}$), the secondary expands, fills its Roche lobe and the system enters a contact phase. The system with an initial mass ratio of q_{in}=2.00 loses $\sim$21$M_\odot$ during the fast phase of Case A. The maximum mass transfer rate of this system is $\dot{M}\approx1.8\cdot10^{-2}M_\odot yr^{-1}$. The helium surface abundance of the primary after this mass transfer is 65%, so the primary shrinks, loses mass through a WR stellar wind and there is no slow phase of Case A mass transfer (R_1<9$R_\odot$). For the other three models q =1.71,1.52,1.37, the primaries lose less mass ($\sim$15,14,13$M_\odot$ respectively) during the fast phase of Case A mass transfer. The helium surface abundances in these systems after fast Case A mass transfer are $\sim$30-35%. The primaries expand ($R\approx$12-15$R_\odot$) on a nuclear time scale and transfer mass to the secondaries (slow phase of Case A).

We can conclude the following: First, if the initial mass ratio is larger, the mass transfer rate from the primary during fast phase Case A mass transfer is higher. Second, if the mass transfer rate is higher, the helium surface abundance of the star increases faster and if it reaches $\approx$58%, the primary starts losing mass with a higher (WR) mass loss rate and slow Case A mass transfer can be avoided.

We also show in Fig. 3.9 (lower plot) how the period changes during Case A mass transfer for binary systems N 3, 4, 6, 7. Roughly, when the mass is transferred from the more to the less massive star, the binary orbit shrinks, and when the mass is transferred from the less to the more massive star, the orbit widens. If the initial period is close to unity, the absolute difference between stellar masses is small, and more mass is transferred from the less to the more massive star during the evolution of the system. This results in a longer final period after Case A mass transfer. Systems with initial mass ratios of 2.00, 1.71, 1.52 and 1.37 enter Case AB mass transfer with orbital periods of 2.9, 3.9, 4.4 and 5.2 days respectively. However, the final period is also (more significantly) influenced by the stellar wind mass loss rate and the amount of matter lost from the primary during Case AB mass transfer (see Section 3.5.4).

3.5.3 Influence of the initial period on the WR mass

Depending on the initial orbital period of a binary system, Case A mass transfer phase will start earlier or later in the evolution. If the period is larger, the primary will develop a larger core, before it starts transferring mass onto the secondary, and the resulting WR star will be more massive. To investigate the influence of the initial period, we compare binary systems 41$M_\odot$+24$M_\odot$ and 56$M_\odot$+33$M_\odot$ with p=3 days and p=6 days (Table 3.2: N 4, 5, 9, 10).

If the initial orbital period increases for 3 days, a 41$M_\odot$ star will enter Case A mass transfer $\sim$8$\cdot10^5$yr later and a 56$M_\odot$ star $\sim$9$\cdot10^5$yr later. So, there are two things to point out: first, the more massive star (56$M_\odot$) evolves faster, and second, a 3 days longer initial period postpones Case A mass transfer, for this star, by about
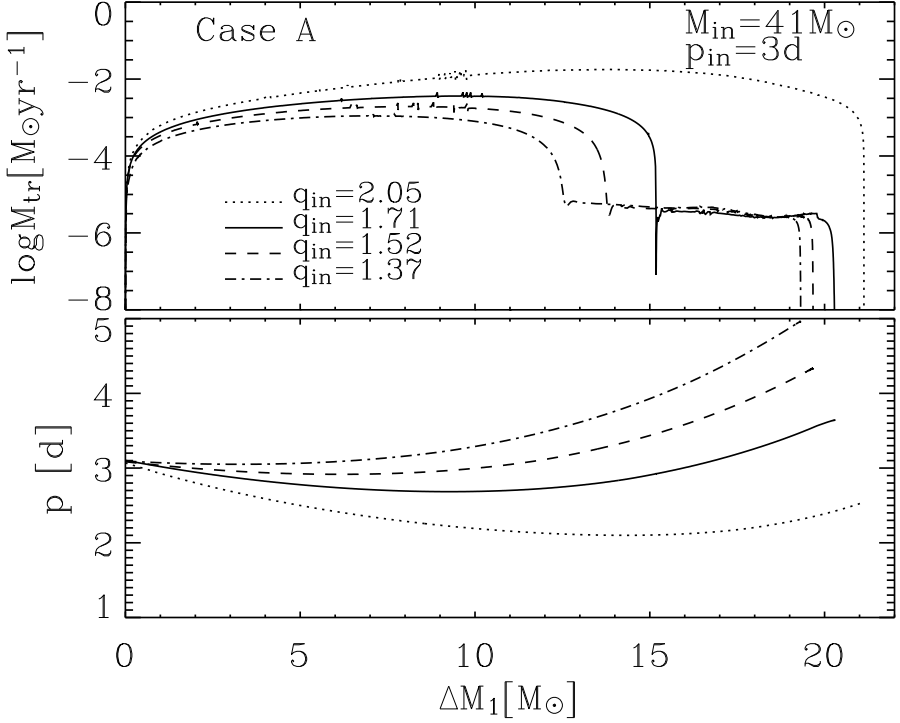
Figure 3.9: Mass transfer rate (upper plot) and orbital period (lower plot) during Case A mass transfer as a function of the change of the primary mass for systems with the initial primary $M_{1,in}$=41$M_{\odot}$, initial orbital period p_{in}=3 days and four different initial mass ratios: 2.00 (dotted line), 1.71 (solid line), 1.52 (dashed line) and 1.37 (dash-dotted line). (Table 3.2 N 3, 4, 6, 7)

10^5yr more than for a 41$M_{\odot}$ star. The net effect is a more significant increase of the convective core (i.e. initial helium core, i.e initial WR mass), for more massive star, due to the initial orbit widening.

3.5.4 Influence of WR mass loss rate on masses and final period

In our models, we assume that when the star has less than 40% of hydrogen at the surface, it starts losing mass according to the Hamann et al. (1995) WR mass loss rate, multiplied by factors: 1/6, 1/3 and 1/2 (Table 3.2: N 10, 11, 12). If the primary is losing more mass by stellar wind during core hydrogen burning, it will develop a less massive helium core. At the same time there will be less matter to be transferred during Roche lobe overflow, so the secondary will accrete less.

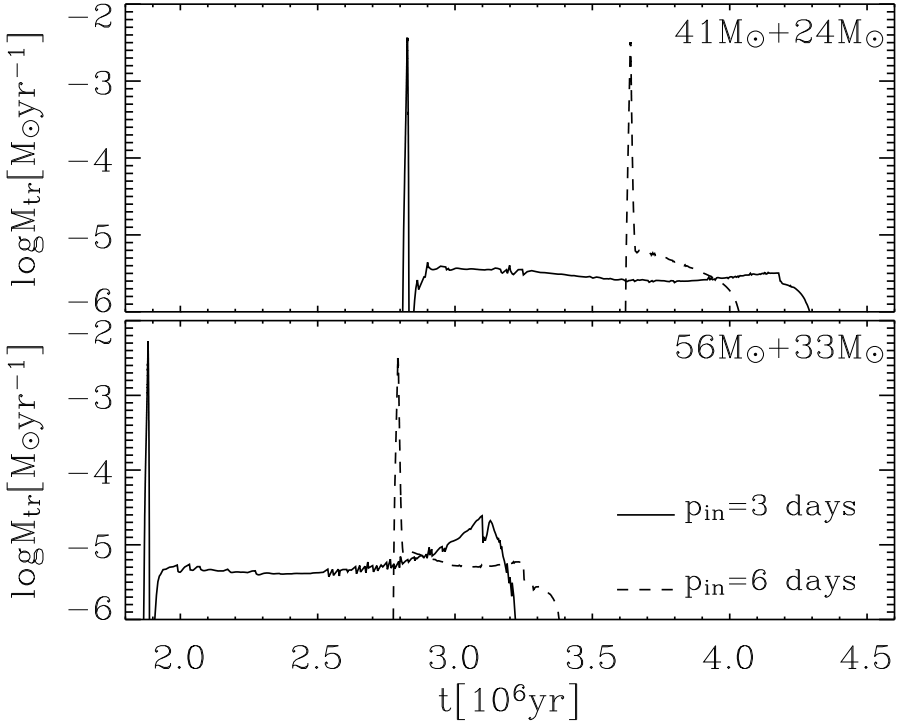We show in Fig. 3.11 the influence of the stellar wind mass loss (Plot c) on the

Figure 3.10: Mass transfer rate during Case A mass transfer for systems $41M_\odot + 24M_\odot$ (upper plot) and $56M_\odot + 33M_\odot$ (lower plot) and an initial orbital period of $p_{in}=3$ days(solid line) and $p_{in}=6$ days (dashed line). Case A mass transfer starts later in initially wider binary systems, the primary has more time to increase mass of its core and the initial WR star is more massive (Table 3.2: N 4, 5, 9, 10).

primary mass (Plot a) and mass transfer rate (Plot b) of systems with $M_{1,in}=56M_\odot$, $M_{2,in}=33M_\odot$, $p_{in}=3$ and three different stellar wind mass loss rates (from $X_s \leq 0.4$): 1/6 (solid line), 1/3 (dotted line) and 1/2 (dashed line) of the mass loss proposed by Hamann et al. (1995). We notice that for higher mass loss rates, the slow phase of Case A stops earlier, due to the decrease of the stellar radius. The orbit is widening due to the stellar wind mass loss and the final period increases with the increasing mass loss rate. However, the orbit is more significantly widening during Case AB mass transfer. The more mass there is to transfer from the primary to the secondary during Case AB mass transfer, the larger the final orbital period. So, if the stellar wind removes most of the hydrogen envelope of the primary, there will be less mass to transfer during Case AB and the net effect of a higher mass loss rate is a shorter orbital period of the WR+O system.
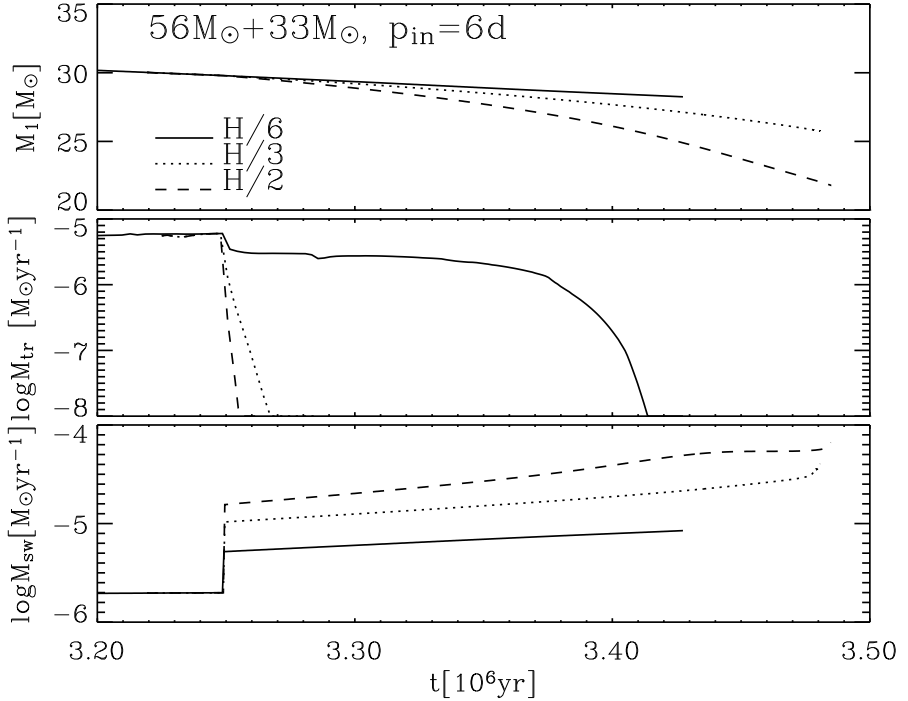
Figure 3.11: Primary mass (first plot), mass transfer rate (second plot) and stellar wind mass loss rate from the primary (third plot) until the onset of Case AB mass transfer for the system $M_{1,in}$=56M$_\odot$, $M_{2,in}$ =33M$_\odot$, p_{in}=6 days and three different stellar wind mass loss rates (from $X_s \leq 0.4$): 1/6 (solid line), 1/3 (dotted line) and 1/2 (dashed line) of mass loss rate proposed by Hamann et al. (1995) (Table 3.2: N 10, 11, 12).

3.6   Rotating models

When mass transfer in a binary system starts, the primary loses matter through the first Lagrangian point (L_1). This matter carries a certain angular momentum that will be transferred to the secondary. If there is an accretion disk, the angular momentum of the transfered matter is assumed to be Keplerian. If there is a direct impact accretion, like in our models, we calculate the angular momentum following a test particle moving through L_1. This angular momentum spins up the top layers of the secondary star, and angular momentum is transfered further into the star due to rotationally induced mixing processes. Every time the secondary spins up to close to critical rotation it starts losing more mass due to the influence of centrifugal force (Eq. 5). High mass loss decreases the net accretion efficiency and also removes angular momentum from the secondary star. The secondary star is also spun

down by tidal forces that tend to synchronize it with the orbital motion. Wellstein (2001) investigated these processes in binary systems with initial mass ratios close to unity and concluded that the accretion efficiency does not decrease significantly for Case A mass transfer, but in the Case B the parameter β can be significantly decreased by rotation. We present Case A rotating models with larger mass ratio $q=M_{1,in}/M_{2,in}=1.7..2$ and find that accretion can be significantly decreased during Case A transfer. The reason is the following: if the initial mass ratio increases, so does the maximum mass transfer rate ($\dot{M}_{mtr}$ increases roughly until the masses in binary system are equal). If there is more mass transferred from the primary to the secondary, the rotational velocity of the secondary is higher as well as its mass loss, which leads to a smaller accretion efficiency.

We compare the evolution of non-rotating and rotating binary systems on the example $M_{1,in}=56M_\odot$ $M_{2,in}=33M_\odot$, an initial orbital period of $p=6$ days, and Hamann/3 WR mass loss stellar wind rate (Table 3.3: N 6). The rotating binary system is synchronized as it starts core hydrogen burning and it stays that way until mass transfer starts. The radius of the primary increases during the main sequence phase (from ~10 to $\sim25R_\odot$, Fig. 3.19b), but the rotation of the primary stays synchronized with the orbital period. This is why the rotational velocity of the primary also increases from ~100 to ~200 k ms^{-1} (Fig. 3.19d). The radius of the rotating primary increases faster than the radius of the non-rotating primary due to the influence of the centrifugal force. The result is that Case A mass transfer starts earlier for the rotating binary system ($X_{c,non}\approx80\%$) then for the corresponding non-rotating one($X_{c,rot}\approx71\%$, Fig. 3.15).

When the fast phase of Case A starts, the secondary spins up (Fig. 3.20d) and stellar wind mass loss rapidly increases ($\dot{M}_{sw}\sim10^{-3}M_\odot yr^{-1}$, Fig. 3.20c). The accretion efficiency during this phase in the rotating system is $\beta=0.15$ (Table 3.3). We see in Fig. 3.15 that the orbital period after Case A mass transfer of the rotating binary system is shorter than for the non-rotating system (4.5 compared with 6.6 days). The orbital angular momentum of the binary is changing due to mass transfer, mass loss from the system and spin-orbit coupling. The rotating binary system loses more angular momentum and the final orbital period is shorter than in the corresponding non-rotating system. Angular momentum loss in our systems is calculated according to Podsiadlowski et al. (1992) as already mentioned in Sect 3.4, and parameter α that determines the efficiency of angular momentum loss is calculated according to Brookshaw & Tavani (1993). It increases with the mass ratio M_2/M_1 and the ratio between the secondary radius and its Roche radius R_2/R_{l2}. In rotating system the secondary accretes slightly more matter ($\bar{\beta}=0.15$) compared to $\beta=0.1$ in non-rotating systems, so the mass ratio M_2/M_1 is larger in the rotating system. Second, the secondary is spinning fast and its radius is larger than in the non-rotating case, and so is the ratio R_2/R_{l2}. The result is that the angular momentum is more efficiently removed from the system in the rotating binary system. After the fast phase of Case A

Table 3.3: Rotating WR+O progenitor models. N is the number of the model, $M_{1,\text{in}}$ and $M_{2,\text{in}}$ are initial masses of the primary and the secondary, p_{in} is the initial orbital period and q_{in} is the initial mass ratio of the binary system. t_A is the time when Case A mass transfer starts, Δt_f is the duration of the the fast phase of Case A mass transfer, $\dot{M}_{\text{tr}}^{\max}$ is the maximum mass transfer rate, $\Delta M_{1,f}$ and $\Delta M_{2,f}$ are mass loss of the primary and mass gain of the secondary (respectively) during the fast Case A, Δt_s is the duration of slow Case A mass transfer, $\Delta M_{1,s}$ and $\Delta M_{2,s}$ are mass loss of the primary and mass gain of the secondary (respectively) during the slow Case A, p_{AB} is the orbital period at the onset of Case AB, $\Delta M_{1,\text{AB}}$ is the mass loss of the primary during Case AB (mass gain of the secondary is $1/10$ of this, see Sect. 3.4), $M_{\text{WR},5}$ is the WR mass when the hydrogen surface abundance is $X_s = 0.05$, M_O is the mass of the corresponding O star, q is the mass ratio M_{WR}/M_O, p is the orbital period of the WR+O system and $M_{\text{WR},1}$ is WR mass with $X_s \leq 0.01$. The models are computed with a stellar wind mass loss of Hamann/6 except :* Hamann/3,** Hamann/2. ^{c} indicates a contact phase

| Nr	$M_{1,\text{in}},$ $M_{2,\text{in}}$	p_{in}	q_{in}	t_A	Δt_f	$\dot{M}_{\text{tr}}^{\max}$	$\Delta M_{1,f},$ $\Delta M_{2,f}$	Δt_s	$\Delta M_{1,s},$ $\Delta M_{2,s}$	p_{AB}	$\Delta M_{1,\text{AB}}$	$M_{\text{WR},5}(1),$ M_O	q	p
	$M_\odot$	d		10^6yr	10^4yr	$M_\odot$/yr	$M_\odot$	10^6yr	$M_\odot$	d	$M_\odot$	$M_\odot$		d
$R1$	$41, 20$	6	2.05	3.4	1.5	6.5	$18.67, 3.33$	0.58	$2.38(1.37), 0.81$	3.97	6.61	$11.0(10.2), 23.98$	0.46	9.78
$R2^{**}$	$41, 20$	6	2.05	3.4	1.5	6.5	$18.67, 3.33$	0.10	$0.32(0.11), 0.20$	4.77	2.96	$10.4(9.0), 23.20$	0.45	7.92
$R3$	$41, 24$	3	1.71	2.6	1.5	3.9	$15.47, 5.04$	1.34	$9.38(1.00), 7.54$	4.27	6.32	$8.2(7.6), 36.17$	0.23	17.86
$R4$	$41, 24$	6	1.71	3.4	2.6	3.8	$17.75, 4.06$	0.68	$2.55(0.9), 1.53$	5.66	7.25	$11.2(10.5), 29.27$	0.38	16.42
$R5$	$56, 33$	6	1.70	2.4	3.7	3.2	$19.32, 2.91$	0.98	$11.93(4.13), 6.98$	6.09	4.88	$14.9(13.6), 42.09$	0.35	11.59
$R6^*$	$56, 33$	6	1.70	2.4	3.7	3.2	$19.32, 2.91$	0.90	$10.93(6.42), 3.91$	6.64	1.8	$14.8(12.8), 38.99$	0.38	8.53
$R7^{**}$	$56, 33$	6	1.70	2.4	3.7	3.2	$19.32, 2.91$	0.45	$3.24(0.65), 2.27$	8.43	0.0	$11.2(8.8), 37.04$	0.30	8.43
$R8$	$60, 35$	6	1.71	2.3	2.2	3.0	$19.97, 3.98$	0.92	$12.32(4.20), 7.21$	6.58	5.27	$15.7(14.6), 45.13$	0.35	12.75
$R9^*$	$60, 35$	6	1.71	2.3	2.2	3.0	$19.97, 3.98$	0.84	$11.42(6.26), 4.58$	7.64	0.0	$14.9(12.2), 42.43$	0.35	7.64
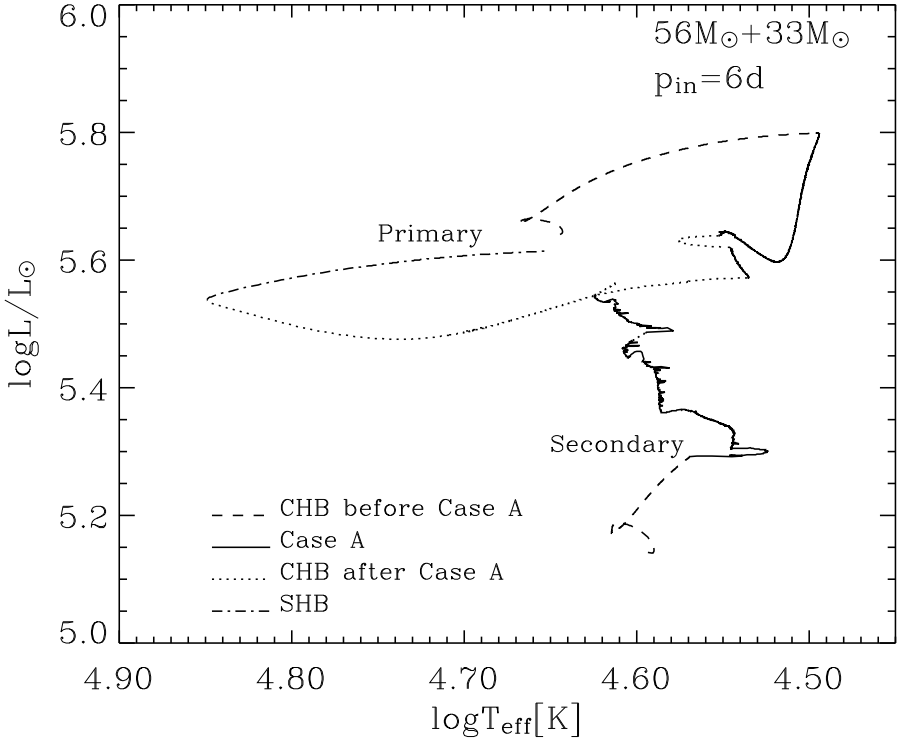
Figure 3.12: HR diagram of the initial system $M_{1,in}$=56M$_\odot$, $M_{2,in}$=33M$_\odot$, p_{in}=6 days with rotation. Both stars are core hydrogen burning (dashed line) until Case A mass transfer starts (solid line). The primary is losing mass and its luminosity decreases. At the same time the secondary is accreting matter and expanding, becoming more luminous. After Case A mass transfer is finished, the primary is losing mass by stellar wind and contracting at the end of core hydrogen burning (dotted line). After this the primary starts shell hydrogen burning and expands (dash-dotted line).

mass transfer, the two primaries, non-rotating and rotating, have almost the same mass $\sim$34M$_\odot$ and helium surface abundance $Y_s\sim$44%. However, since the orbital periods are different, so are the radii of the primaries ($\sim$18R$_\odot$ for the rotating and $\sim$23R$_\odot$ for the non-rotating case).

When the fast phase of Case A is finished, the non-rotating primary has still $\sim$20% of hydrogen to burn ($\sim$7·10^{5}yr), and the rotating primary has $\sim$10% more than that ($\sim$1.2·10^{6}yr). When the surface hydrogen abundance is less than 40%, the primaries start losing mass as WR stars, i.e., their stellar wind mass loss rate increases. Since the rotating primary has more time to spend on the main sequence, it also has more time to lose mass by WR stellar wind mass loss (7.2·10^{5}yr compared
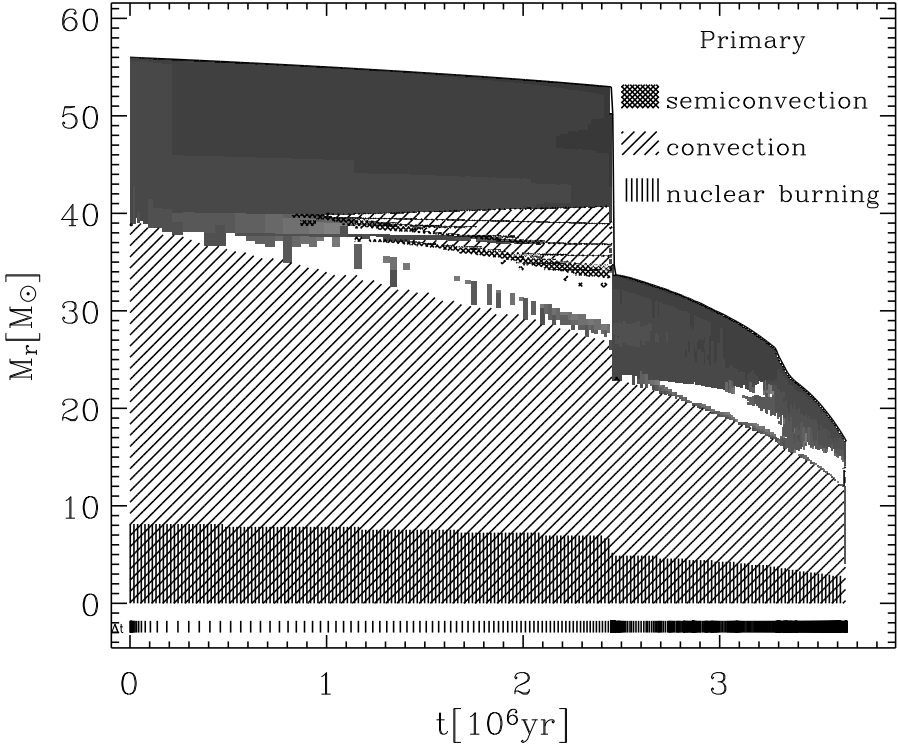
Figure 3.13: The evolution of the internal structure of the rotating 56M$_\odot$ primary during core hydrogen burning. Convection is indicated with diagonal hatching and semiconvection with crossed hatching. The hatched area at the bottom indicates nuclear burning. Gray shaded areas represent regions with rotationally induced mixing (intensity is indicated with different shades, the darker the colour, the stronger rotational mixing). The topmost solid line corresponds to the surface of the star.

with 2.5·10^{5}yr for non-rotating system).The result is that the non-rotating primary enters Case AB mass transfer as a $\sim$26M$_\odot$ star with Y_s=0.75, while the rotating one is a $\sim$17M$\odot$ star with Y_s=0.90. Clearly, the rotating primary has less hydrogen in its envelope, i.e. less mass to transfer to the secondary during Case AB mass transfer, and the orbit widens less than in the non-rotating system. We can draw the conclusion that if rotation is included in our calculations, the initial WR mass is smaller and the orbital period of the WR+O system is shorter than in the corresponding non-rotating system (Table 3.4).

We present in Fig. 3.12 the evolutionary tracks of the rotating primary and secondary in the HR diagram. Both stars are core hydrogen burning stars (dashed line, Fig. 3.12), but since the primary is more massive, it evolves faster and fills its Roche
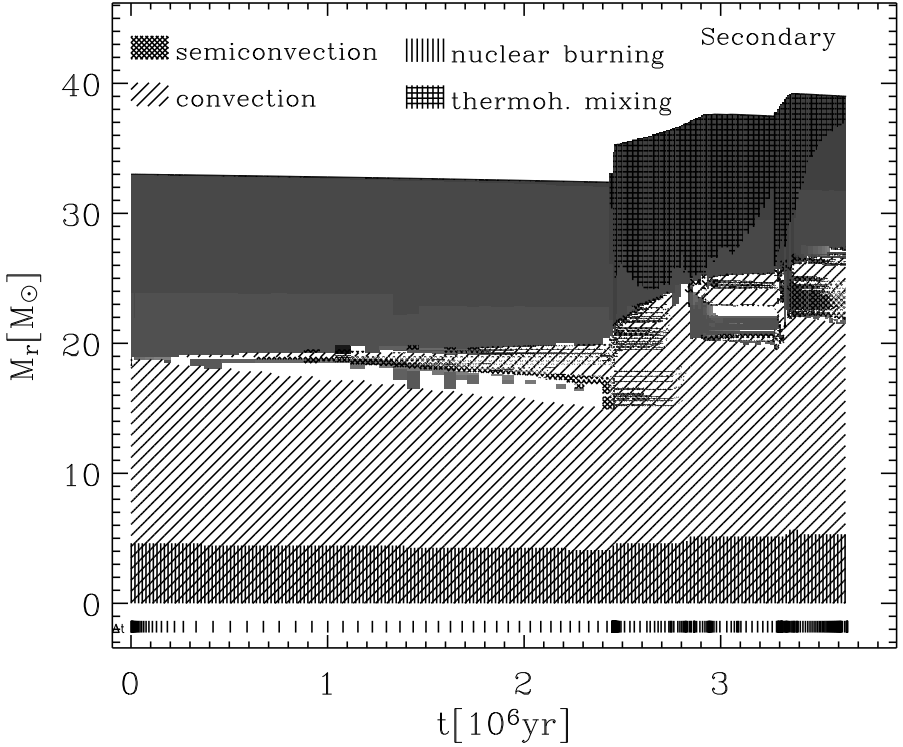
Figure 3.14: The evolution of the internal structure of the rotating $33M_\odot$ secondary during core hydrogen burning of the primary. Convection is indicated with diagonal hatching, semiconvection with crossed hatching and thermohaline mixing with straight crossed hatching. The hatched area at the bottom indicates nuclear burning. Gray shaded areas represent regions with rotationally induced mixing (intensity is indicated with different shades, the darker the colour, the stronger rotational mixing). The topmost solid line corresponds to the surface of the star.

lobe, so the system enters Case A mass transfer (solid line, Fig. 3.12). The primary loses matter quickly with a high mass transfer rate ($\dot{M}_{tr}^{max} \approx 3.2 \cdot 10^{-3} M_\odot yr^{-1}$) and its luminosity decreases (Fig. 3.12). At the same time the secondary accretes matter and its luminosity increases, but due to change in rotational velocity (Fig. 3.20d) its radius and effective temperature are changing as well (Fig. 3.12d, Fig. 3.20a,b). During fast Case A mass transfer the primary lost $\sim 19M_\odot$ and the secondary accreted 15% of that matter. After the fast mass transfer, the primary is still burning hydrogen in its core and is still expanding, so slow Case A mass transfer takes place. After the primary starts losing mass with a WR stellar wind mass loss rate ($X_s < 0.4$) its radius will decrease and the slow phase of Case A stops (Fig. 3.19c). However, the
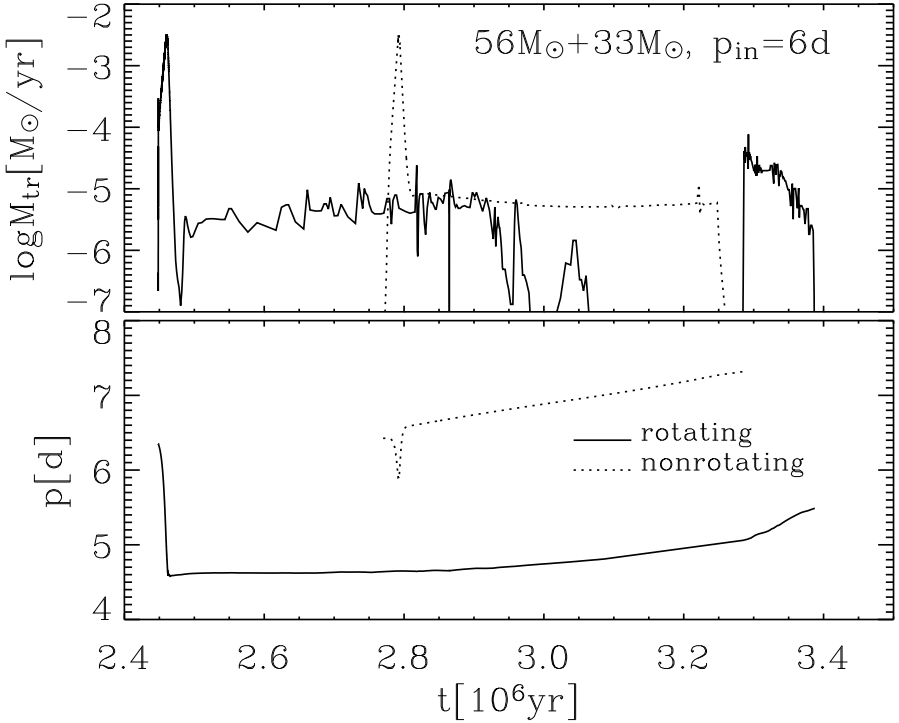
Figure 3.15: Upper plot: The mass transfer rate during Case A mass transfer in the binary systems with $M_{1,in}$=56M$_\odot$, $M_{2,in}$=33M$_\odot$, p_{in}=6 days with (solid line) and without rotation (dotted line). Lower plot: Orbital period evolution in rotating and non-rotating system.

primary continues expanding on the nuclear time scale (Fig. 3.19b) and it fills its Roche lobe once again (Fig. 3.15, upper plot). At the end of core hydrogen burning the primary contracts (effective temperature increases) and thus RLOF stops. This phase is presented in Fig. 3.12 with a dotted line. When hydrogen starts burning in a shell, the primary star expands (dash-dotted line, Fig. 3.12), fills its Roche lobe and Case AB mass transfer starts.

The initial helium core masses are 18.6M$_\odot$ for the non-rotating and 14.8M$_\odot$ for the rotating primary. When Case AB mass transfer starts, the orbital periods are 7.9 d and 6.6 d for the non-rotating and the rotating system respectively (Fig. 3.15, lower plot). The non-rotating primary loses $\sim$7M$_\odot$ and the rotating one $\sim$2M$_\odot$ during Case AB. When there is more mass to be transfered from the less to the more massive star in a binary system, the orbit widens more and the final orbital period is longer.
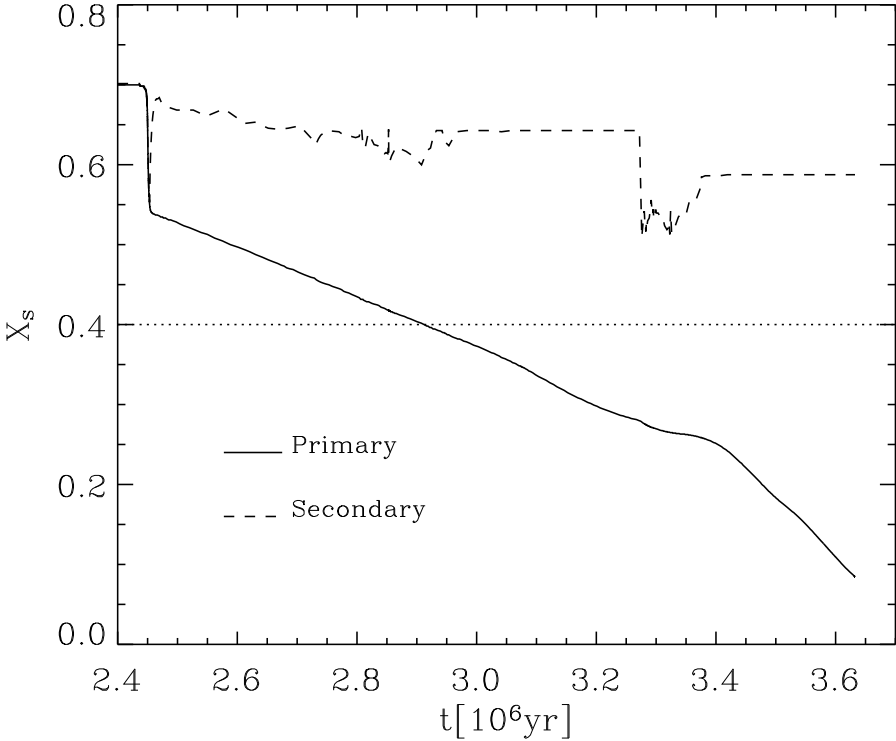
Figure 3.16: The hydrogen surface abundance (solid line) in the primary in system with $M_{1,in}$=56M$_\odot$, $M_{2,in}$=33M$_\odot$, p_{in}=6 days is decreasing during mass transfer and further due to stellar wind mass loss. The secondary (dashed line) decreases its hydrogen surface abundance due to mass transfer. The dotted line indicates a hydrogen abundance of 0.4, where the primary starts losing mass with a WR stellar wind.

Fig. 3.13 and Fig. 3.14 show the structure of the primary and the secondary before Case AB mass transfer. The primary loses large amounts of matter during the fast phase of Case A mass transfer ($\sim$20M$_\odot$), and its convective core becomes less than half of its original mass. At the same time, the secondary accretes matter from the primary and the heavier elements are being relocated by thermohaline mixing. Fig. 3.16 and Fig. 3.17 show surface abundances of the primary and the secondary. The primary is losing matter and decreases its hydrogen and nitrogen abundance on the surface, while increasing carbon and oxygen. The secondary is accreting material from the primary and its surface abundances change due to this, but also due to thermohaline and rotational mixing.

Fig. 3.18 shows the orbital angular momentum of the system and the spin periods of both components. The orbital angular momentum of the system decreases rapidly
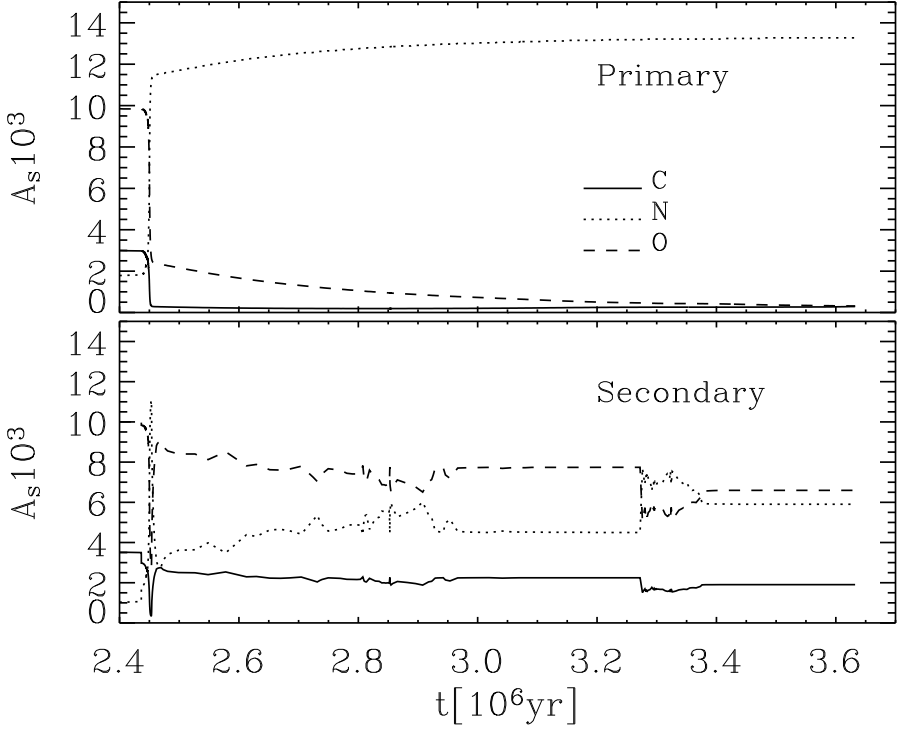
Figure 3.17: Surface abundance of carbon (solid line), nitrogen (dotted line) and oxygen (dashed line) in the primary (upper plot) and the secondary (lower plot), in the system with $M_{1,in}$=56M$_\odot$, $M_{2,in}$=33M$_\odot$, p_{in}=6 days. The secondary abundances are changed due to mass transfer of matter from the primary, thermohaline mixing and rotational mixing.

due to mass loss from the system during fast Case A mass transfer, and then further due to stellar wind mass loss. The primary slows down rapidly during fast Case A and further due to stellar wind mass loss. The secondary spins up due to the accretion from the primary during fast Case A mass transfer and then slows down due to stellar wind mass loss. It spins up again during slow Case A mass transfer.

The masses of modelled WR stars are in the range from ∼11M$_\odot$ to ∼15.7M$_\odot$. Period of modelled WR+O systems vary from ∼7.6 to ∼12.7 days and mass ratios are between 0.35 and 0.46 (Table 3.3)
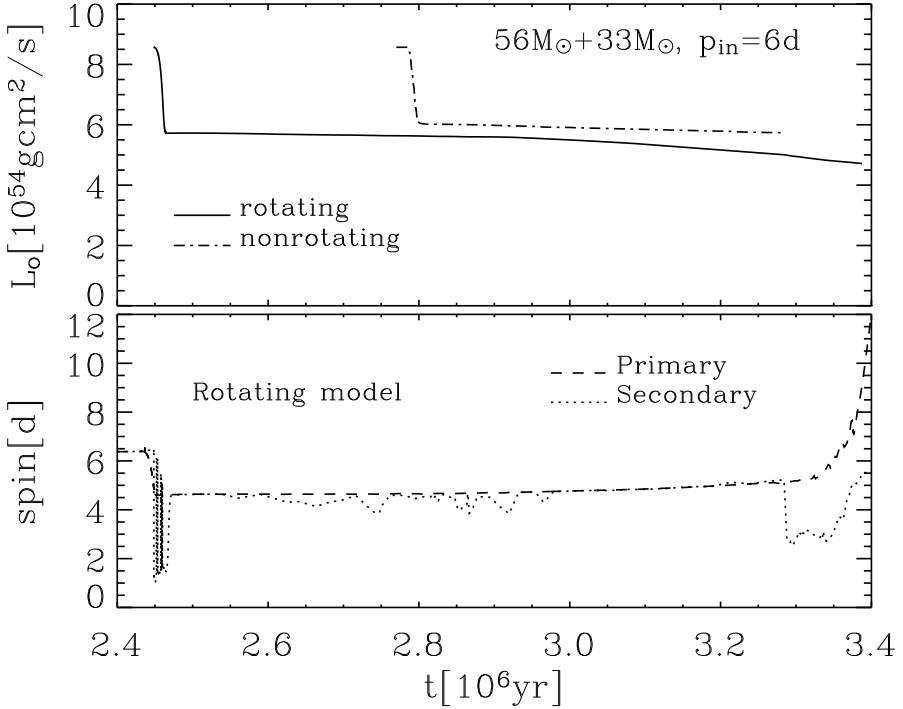
Figure 3.18: The orbital angular momentum (upper plot) of the non-rotating (dotted line) and the rotating (solid line) binary systems with $M_{1,in}$=56M$_\odot$, $M_{2,in}$=33M$_\odot$, p_{in}=6 days, decreases rapidly due to mass loss from the system during fast Case A mass transfer and then further due to stellar wind mass loss. Spin period (lower plot) of the primary (dashed line) and the secondary (dash-dotted line) in the above mentioned rotating binary system.

3.6.1 Influence of rotation on the accretion efficiency

We show in Table 3.5 average accretion efficiencies of rotating binary systems during different mass transfer phases, and total average values with and without stellar wind mass loss from the primary included. During fast Case A mass transfer, the primary stars are losing matter with very high mass transfer rates ($3..6.5 \cdot 10^{-3} M_\odot yr^{-1}$). The angular momentum of surface layers in the secondary increases fast, they spin up to close to the critical rotation and start losing mass with high mass loss rate ($\sim 10^{-3} M_\odot$). The average accretion efficiency during fast Case A in our models is 15-20%. Since this phase takes place on the thermal time scale, stellar wind mass loss from the primary is negligible during this phase.

Slow Case A mass transfer takes place on the nuclear time scale. The primary stars start losing their mass due to a WR stellar wind when their surfaces become
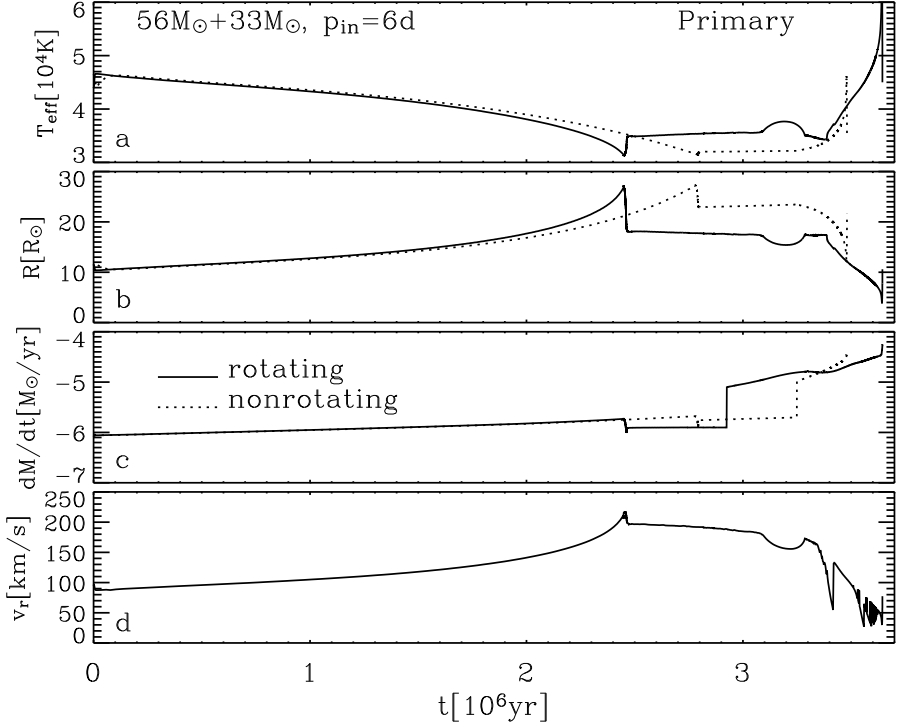
Figure 3.19: Effective temperature (plot a), stellar radius (plot b), stellar wind mass loss rate (plot c) and rotational velocity (plot d) of the primary star in the non-rotating (dotted line) and rotating (solid line) binary system with $M_{1,in}$=56M$_\odot$, $M_{2,in}$=33M$_\odot$, p_{in}=6 days.

hydrogen deficient (X_s<0.4). The WR stellar wind mass loss rates are of the order of : $\dot{M}$∼10^{-5}M$_\odot$yr^{-1}, and we have to take into account stellar wind mass loss of the primary during slow Case A. We calculate the mass loss of the primary only due to mass transfer and total mass loss including stellar wind mass loss, and the two corresponding average accretion efficiencies. If we calculate $\bar{\beta}_s$ only for mass transfer, we notice that the slow Case A is almost a conservative process. The average mass transfer rates are ∼10^{-6}M$_\odot$yr^{-1} and the secondary stars are able to accrete almost everything without spinning up to critical rotation.

Fig. 3.21 shows how mass transfer rate, accretion rate and β change in the rotating model with 56M$_\odot$+33M$_\odot$, p_{in}=6 days (WR mass loss Hamann/3) depending on the amount of matter lost by the primary. We also see in this figure the mass transfer rate from the primary in the non-rotating case. We can notice in the upper plot, what we previously discussed, that during most of the fast Case A mass transfer, the mass
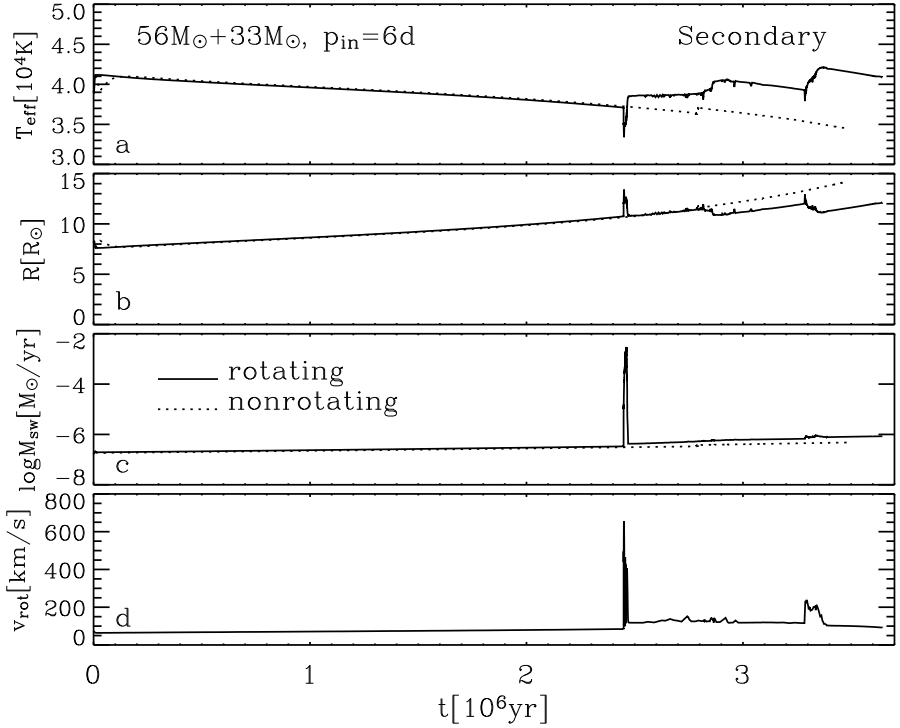
Figure 3.20: Effective temperature (plot a), stellar radius (plot b), stellar wind mass loss rate (plot c) and rotational velocity (plot d) of the secondary star in the non-rotating (dotted line) and rotating (solid line) binary system with $M_{1,\text{in}}$=56M$_\odot$, $M_{2,\text{in}}$=33M$_\odot$, p_{in}=6 days.

accretion rate of the secondary is about one order of magnitude lower than the mass loss rate of the primary. The primary loses ~19.3M$_\odot$ during the fast phase and the secondary gains ~2.9M$_\odot$, which means that on average ~15% of the mass has been accreted. However, the mass loss of the primary due to mass transfer during the slow phase is ~4.5M$_\odot$, and the secondary accretes ~3.9M$_\odot$ which means that $\bar{\beta}_s$ ~0.87. If we take into account stellar wind mass loss of the primary stars, the average accretion efficiencies are lower. For example, the total mass loss of the primary during slow Case A mass transfer, including the stellar wind, in the previous example is ~10.9M$_\odot$, which means that $\bar{\beta}_s^w$≈0.36. We neglected accretion during Case AB mass transfer since Wellstein (2001) showed that it is inefficient, and since the primary stars in the modelled systems have relatively low mass hydrogen envelopes, and masses of secondary stars will not significantly change due to this mass transfer. (However, let us not forget that even the accretion of very small amounts of matter

Table 3.4: Comparison of resulting WR masses and orbital periods from non-rotating and rotating binary systems with the same initial parameters. $M_{1,\text{in}}$, $M_{2,\text{in}}$ are initial primary and secondary mass, p_{in} is the initial orbital period, $M_{\text{WR},5}$, $M_{\text{WR},1}$ are WR masses at $X_{\text{s}} = 0.05$ and $X_{\text{s}} \leq 0.01$ respectively and p is the orbital period in the initial WR+O system where the hydrogen surface abundance of WR star is $X_{\text{s}} = 0.05$. Systems are modelled with WR stellar wind mass loss H/6 except * which are done with H/3, [R] indicates rotating models.

$M_{1,\text{in}} + M_{2,\text{in}}$ [$M_\odot$]	p_{in} [d]	$M_{\text{WR},5}$ [$M_\odot$]	$M_{\text{WR},1}$ [$M_\odot$]	p [d]
$41 + 20$	6	11.8	11.2	12.6
$41 + 20^{\text{R}}$	6	11.0	10.2	9.8
$41 + 24$	6	12.1	11.4	21.5
$41 + 24^{\text{R}}$	6	11.2	10.5	16.4
$56 + 33^{*}$	6	18.6	17.5	13.8
$56 + 33^{*,\text{R}}$	6	14.9	13.6	8.5

can be important for spinning up the secondary's surface layers and making it rotate faster than synchronously in a WR+O binary system.) Also, since this mass transfer takes place on the thermal time scale, stellar wind mass loss can be neglected.

Finally, we can estimate the total mass loss from the binary systems including stellar wind, or only due to mass transfer, and calculate corresponding values of β. In the binary systems we modelled, the primary stars lose between $30M_\odot$ and $45M_\odot$ due to mass transfer and stellar wind, until they ignite helium in their core. The amount of lost mass increases with initial mass. At the same time the secondaries accrete $3..10M_\odot$. This means that in most cases $80..90\%$ of the mass lost by the primary leaves the binary system. On the other hand, the primary stars lose $\sim 20..30M_\odot$ only due to mass transfer, so the average accretion of secondary stars in our models is between 15 and 30%.

3.7   Comparison with observations

Our rotating models give generally similar results as our non-rotating models for $\beta = 0.1$.

The rotating binary systems R6 ($56M_\odot + 33M_\odot$, p=6 days, Hamann/3 WR mass loss) and R1 and R2 ($41M_\odot + 20M_\odot$, p=6 days) agree quite well with the observed systems HD186943 and HD90657, as well as the non-rotating systems N11 and N12 ($56M_\odot + 33M_\odot$, p=6 days; WR mass loss rate Hamann/2 and Hamann/3). The system R6 evolves into a WR+O configuration with $15M_\odot + 39M_\odot$ and p=8.5 days.

Table 3.5: Mass loss from binary systems. N is number of the model corresponding to Table 3.3. $\bar{\beta}_{\mathrm{fast}}$ is the average accretion efficiency of the secondary during the fast phase of Case A mass transfer. $\bar{\beta}_{\mathrm{slow}}$ is the accretion efficiency of the secondary during the slow phase of Case A mass transfer taking into account matter lost by the primary only due to the mass transfer. $\bar{\beta}_{\mathrm{slow}}^{\mathrm{wind}}$ is the average accretion efficiency of the secondary during the slow phase of Case A mass transfer taking into account matter lost by the primary due to the mass transfer and stellar wind. $\bar{\beta}$ is the average accretion efficiency of the secondary during the progenitor evolution of WR+O binary system taking into account matter lost by the primary only due to the mass transfer and $\bar{\beta}_{\mathrm{mtr}}^{\mathrm{wind}}$ taking also into account stellar wind mass loss of the primary.

Nr	$\bar{\beta}_{\mathrm{fast}}$	$\bar{\beta}_{\mathrm{slow}}$	$\bar{\beta}_{\mathrm{slow}}^{\mathrm{wind}}$	$\bar{\beta}$	$\bar{\beta}^{wind}$
$R1$	0.18	0.80	0.35	0.15	0.13
$R2$	0.18	0.95	0.65	0.15	0.10
$R3$	0.33	0.90	0.80	0.40	0.37
$R4$	0.23	0.94	0.60	0.20	0.18
$R5$	0.15	0.90	0.58	0.28	0.22
$R6$	0.15	0.87	0.36	0.23	0.14
$R7$	0.15	0.88	0.70	0.18	0.09
$R8$	0.20	0.88	0.58	0.30	0.23
$R9$	0.20	0.89	0.40	0.30	0.16

I.e., its masses and period are close to those found in HD186943 and HD90657, even though its mass ratio of 0.38 is somewhat smaller than what is observed. Systems R1 and R2 evolve into a $11M_{\odot}+24M_{\odot}$ WR+O system with a 9.8 day orbital period. I.e., period and mass ratio (0.46) agree well with the observed systems, but the stellar masses are somewhat smaller than observed (cf. Sect. 3.2). Systems N11 and N12 evolve into a WR+O system of $19M_{\odot}+35M_{\odot}$ with an orbital period of 12..14 days. In this case, both masses and the mass ratio (0.53) agree well with the observed ones, but the orbital period is slightly too large. I.e., although none of our models is a perfect match of HD186943 or HD90657 — which to find would require many more models, however, might not teach us very much — it is clear form these results that both systems can in fact be well explained through highly inefficient Case A mass transfer.

The situation is more difficult with HD211853 (GP Cep): neither the models with nor those without rotation reproduce it satisfactory. HD211853 has the shortest period (6.7 d) and largest mass ratio (0.54) of the three chosen Galactic WR+O binaries. While we can not exclude that a Case A model of the kind presented here can reproduce this systems, especially the small period makes it appear more likely that this system has gone through a contact phase: contact would reduce the orbital angular momentum, and increase the mass loss from the system, i.e. result in a
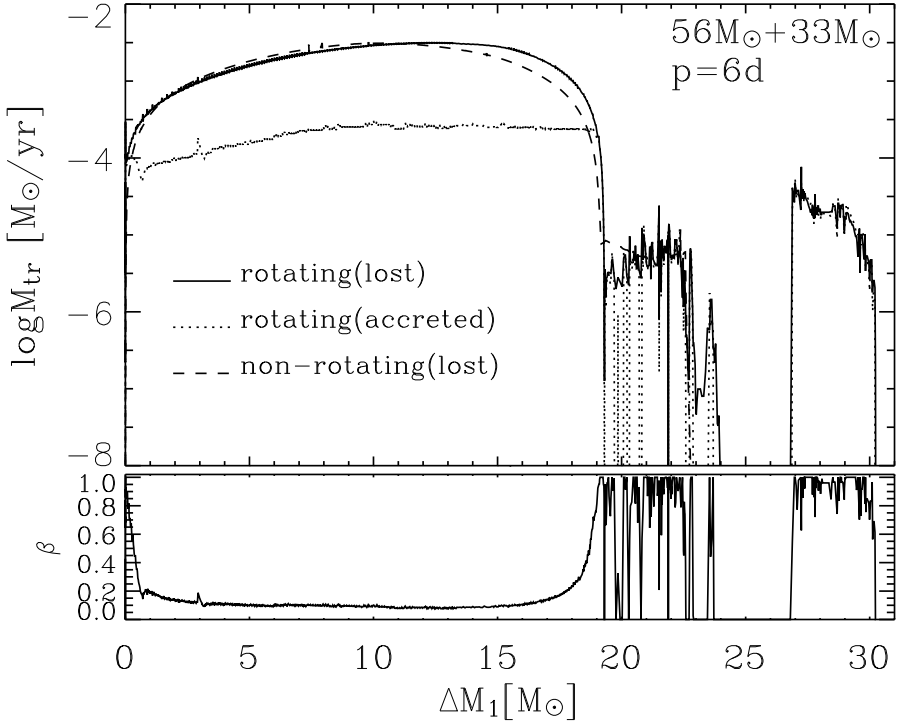
Figure 3.21: Upper plot: Mass transfer (solid line) and accretion rate (dotted line) of the rotating initial system $56M_\odot+33M_\odot$, $p = 6$ days. Dashed line represent mass transfer rate in the corresponding non-rotating binary. Lower plot: accretion efficiency of the secondary taking into account matter lost by the primary only due to mass transfer.

larger WR/O mass ratio (Wellstein et al. 2001). This reasoning is strengthened by the consideration that, in contrast to HD186943 or HD90657, the WR star in HD211853 is of spectral type WN6/WNC. I.e., as this spectroscopic signature is not interpreted in terms of a binary nature of the WR component, but rather by assuming that the WR star is in the transition phase from the WN to the WC stage (Massey & Grove 1989; Langer 1991). This implies that the WR star in HD211853 must have already lost several solar masses of helium-rich matter, which causes the orbit to widen. For example, system R6, which evolved into a $14.8M_\odot+39.0M_\odot$ WR+O system with p=8.53 days, evolves into a WC+O system after losing $\sim$5$M_\odot$ more from the Wolf-Rayet star, which increases its orbital period by $\sim$3 days. I.e., HD211853 might have entered the WR+O stage with an orbital period of about 4 days, which would put it together with the shortest period WR binaries like CX Cep or CQ Cep whose periods are 2.1 and 1.64 days respectively.

During the evolution of WR+O binary system, the primary loses mass due to WR stellar wind mass loss. WR stellar wind mass loss of the primary decreases mass ratio of the system and increases the orbital period, which means that, for example, WC+O binary system HD63099 (M_{WR}=9M$_\odot$, M_{O}=32M$_\odot$ and p=14 days) could have evolved into present state through a WN+O binary system with q=0.5.

3.8 Conclusions

In an effort to constrain the progenitor evolution of the three WN+O binaries HD186943, HD90657, and HD211853, we calculated the evolution of non-conservative Case A binary systems with primaries $M_{1,\mathrm{i}}$=41..65M$_\odot$ and initial mass ratios between 1.7 and 2 until the WN+O stage. We performed binary evolution calculations neglecting rotational processes in the two stellar components, and assuming a constant mass accretion efficiency of 10% for all three phases of the mass transfer, fast Case A, slow Case A, and Case AB. Those models could match two of the three systems reasonably well, while HD211853, which has the shortest orbital period, the largest mass ratio, and a WN/WC Wolf-Rayet component, was found to be not well explained by contact-free evolutionary models: While models with shorter initial orbital periods result in short periods during the WR+O stage, the initial WR mass is decreasing at the same time, which leads to smaller initial WR/O mass ratios.

We then computed binary evolution models including the physics of rotation in both stellar components as well as the spin-up process of the mass gainer due to angular momentum accretion. In these models, the surface of the accreting star is continuously spun-up by accretion, while at the same time angular momentum is transported from the outer layers into the stellar interior by rotationally induced mixing processes. By employing a simple model for the mass loss of rapidly rotating luminous stars – the so called Ω-limit, which was actually worked out to describe the mass loss processes in Luminous Blue Variables (Langer 1997) — accretion is drastically reduced once the star reaches critical rotation at its surface. The mass accretion rate is then controlled by the time scale of internal angular momentum transport.

Some first such model for Case A and early Case B have been computed by Wellstein (Langer et al. 2003, 2004) for a primary mass of 15M$_\odot$ and a mass ratio close to one. The result was that rather high mass accretion efficiencies ($\beta \simeq 0.7$) could be obtained for initial periods shorter than about 8 days. Here we find that, with the same physical assumptions although at higher system mass, the accretion efficiency drops to about 10% at an initial mass ratio of 1.7. As Wellstein (2001) computed one early Case A model for a 26M$_\odot$+25M$_\odot$ system which gave β=0.63, it is like the high initial mass ratio in our models which is responsible for the low accretion efficiency: Larger initial mass ratios lead to larger mass transfer rates and,

as the time scale of internal angular momentum transport in the accreting star is rather unaffected, to smaller accretion efficiencies.

Our rotating models — in which the accretion efficiency is no free parameter any more but is computed selfconsistent and time-dependent — reproduce the observed WR+O binaries quite well, i.e. as good as our models without rotation physics, where the accretion efficiency is a free parameter. Our simplified considerations in Sect. 3.3 have shown that this is unlikely attributable to the freedom in the choice of the initial parameter of the binary system, i.e. initial masses and period — at least under the assumption that contact was avoided. In case of contact, various new parameters enter the model, similar to the case of common envelope evolution. And indeed, also our rotating models can not reproduce HD211853 very well, mostly because it currently has a too short orbital period, which was likely even significantly shorter at the beginning of its WR+O stage. However, this of course only confirms the result of the simpler approaches that a contact-free approach does not work well for this system.

In summary we can say that the system mass and angular momentum loss model used here — which is the first detailed approach to tackle the long-standing angular momentum problem in mass transferring binaries — has passed the test of WR+O binaries. However, it still needs to be explored over which part of the space spanned by the initial binary parameters this model works well, and to what extent its results are sensitive to future improvements in the stellar interior physics. The inclusion of magnetic fields generated by differential rotation (Spruit 2002) will be the next step in this direction (Petrovic et al. 2004b).

Chapter 4

The impact of radiation and wind momenta on mass transfer in massive close binary systems

Abstract. We investigate to what extent the radiation and stellar wind momenta in a massive close binary system can remove part of the matter flowing from one towards the other star during a mass transfer phase. We perform radiation-hydrodynamics simulations in the co-rotating frame of a binary system made-up of two main sequence stars of $27\,\mathrm{M_\odot}$ and $26\,\mathrm{M_\odot}$ in a 4 day orbit. We study the interaction of the winds of both stars, and of their photons, with the accretion stream originating from the Roche-lobe filling component. For our simulation, we adopt a mass transfer rate of $5 \times 10^{-6}\mathrm{M_\odot}\,\mathrm{yr}^{-1}$, a mid-point in the range of values during massive binary star evolution. Our simulations show that even for such moderate mass transfer rates, the wind and radiative momenta do not alter the dynamics of the accretion stream which is observed to follow essentially ballistic trajectories. Such a conclusion is reinforced for higher mass transfer rates because of the increased stream density and the correspondingly reduced radiation force. We anticipate that the radiation and wind momenta will affect the accretion stream only when its density is comparable to the wind's, a situation wherein the mass transfer rate is vanishingly small and irrelevant for binary star evolution. Alternatively, such reduced accretion stream density could be obtained from spatial dilution in wider systems, potentially leading to non-conservative mass transfer.

authors: Luc Dessart, Norbert Langer, Jelena Petrovic
published in A&A

4.1   Introduction

Massive close binary stars may produce the most powerful explosions in the universe, the cosmic gamma ray bursts (GRBs), which can trace star formation to very high redshifts (Lloyd-Ronning et al. 2002). While the merger model for GRBs is clearly based on massive binaries (Fryer et al. 1999), even the collapsar model (MacFadyen & Woosley 1999) may require accretion of angular momentum in the GRB progenitor (Langer et al. 2003), as current single star models appear to have too little angular momentum (Heger et al. 2000a, 2003b). Further evolved observed massive binary counterparts include massive X-ray binaries — where in particular the black hole systems may again be linked to GRBs (Brown et al. 2000) —, supernovae of Type Ib and Ic (Podsiadlowski et al. 1992), Wolf-Rayet binaries (Schulte-Ladbeck 1989) and massive Algol systems (Penny et al. 2002).

To understand all these exciting objects, we need to understand the evolution of massive close binaries. However, the reliability of massive binary evolution models is hampered by a major uncertainty: What fraction of the mass transfered during a Roche-lobe overflow phase can be accreted by the secondary star?

From observations of post-mass transfer systems, there seems to be evidence for both extremes. The two O stars in the binary V 729 Cyg have a mass ratio of 3.5 but the same spectral type and visual flux (Bohannan & Conti 1976). An initial mass ratio close to 1 is required to ensure the possibility of accretion (see below). However, since during the mass transfer phase a primary star would lose just about half of its mass, a mass ratio of at most 2 could be produced were the secondary not allowed to accrete. Another system showing strong evidence for accretion is the massive X-ray binary Wray 977; it would require that stars of $M \gtrsim 40\,M_\odot$ form neutron stars to explain this system without accretion (Wellstein & Langer 1999).

Several Galactic short period WNE+O binaries, on the other hand, cannot be understood had the O star accreted substantial amounts from the WNE progenitor (Petrovic & Langer 2003). While those might have formed through common envelope evolution — for which no accretion is expected — the key X-ray binary 4U 1700-37 has such a short period that a major accretion phase can be excluded. However, as common envelope evolution would lead to a compact object much more massive than $2.4\,M_\odot$, a short initial period is most likely here (Clark et al. 2002).

From the theoretical viewpoint, accretion in massive close binaries appears difficult. Indeed, the accreted material carries a large amount of angular momentum, potentially spinning the surface of the secondary star up to critical rotation, thereby halting the accretion process (Packet 1981; Wellstein 2001; Langer et al. 2003). In particular for the case of massive binaries, where accretion appears possible from the stellar structure point of view — short period systems consisting of two main sequence stars with nearly equal masses — this process faces another threat.

Short period systems, because of their reduced orbital separation, undergo mass

transfer during the core hydrogen burning evolution of the primary (so called Case A mass transfer). As the masses of both stars are similar, so are their thermal time scales, which means that the secondary does not swell due to mass overflow on the thermal time scale of the primary, thus avoiding a contact situation (Wellstein & Langer 1999; Wellstein et al. 2001). As both stars have a similar size, the accreting star fills a significant fraction of its critical volume, leaving no space for an accretion disk, i.e. the overflowing matter may impact directly onto the accreting star, thereby minimising the angular momentum gain of the secondary (Wellstein 2001; Langer et al. 2003).

However, the price to pay for these advantages for accretion is a threat to it: A mass ratio close to one in a massive Case A binary means that the secondary is a massive and luminous main sequence star, i.e., it has an intense radiation field and a powerful stellar wind. Evolutionary studies of massive binary star systems so far have not investigated the impact of such wind and radiation momenta on the dynamics of accretion streams, but instead *adopted*, with a variable level of justification, how conservative mass transfer ought to be. This covers investigations that simply assume the amount of mass loss from the system (Huang & Taam 1990; Kondo 1974; Vanbeveren 1996) and those that account for a modulation depending on luminosity, evolutionary stage etc... (Podsiadlowski et al. 1992; Doom & de Greve 1983; de Loore & de Greve 1992; de Loore & Vanbeveren 1994). Some detailed calculations of mass transfer and accretion do exist but were limited to objects with no stellar wind and weak radiation fields (Blondin et al. 1995; Boroson et al. 2001). Here, we wish to study the mass transfer properties in massive binary systems, avoiding former educated guesses by addressing with a physical rather than phenomenological model the dynamical properties of the accretion stream in the presence of stellar winds and intense radiation fields expected in such environments.

We present radiation-hydrodynamic simulations in §2, discussing the choice of geometrical set-up, boundary conditions and the radiation force implemented. In §3, we show the results of such a model for different scenarios of wind-momentum balance between the two components. We also discuss the outcome for different accretion stream densities and cross-sections. From our simulations, we conclude in §4 that radiation and wind momenta play an insignificant role in the mass budget during the mass transfer evolution of our example system.

4.2   Description of the radiation-hydrodynamics model

The radiation-hydrodynamics simulations presented in this paper were performed with ZEUS–2D (Stone & Norman 1992), a finite difference, Eulerian code whose original magnetism and radiation modules were switched–off during the calculations. Hence, we only make use of the hydrodynamical structure of the code, im-

plementing our own radiation module independently (see below). The advection scheme used is the first order Van Leer method. We introduce some artificial viscosity to smooth out strong shocks, improving the stability of the code without affecting the main features of the simulations. The simulated fluid is assumed isothermal, so that the sound speed is everywhere equal to a unique value corresponding to a temperature of 30 000 K.

In the present work, we have slightly modified the code to work in the equatorial plane of the system, in spherical polar rather than cylindrical coordinates. Since we wish to study the trajectory of the accretion stream leaving the primary photosphere *via* the first Lagrangian point L1, the secondary is placed at the origin of the coordinate system. We calculate the fluid properties from the secondary photosphere out to a distance which corresponds to the orbital separation. In the azimuthal direction, we cover the full 2π angle as seen from the secondary star center. However, the simulated domain is truncated along the line of centers and near the primary. The surface of the latter cannot be described by a simple change of one of the coordinates, but rather follows a curve relating the coordinates (r,ϕ). Its photosphere, which acts as a boundary, has a sawtooth shape, making its treatment very delicate, as encountered by Owocki et al. (1994) and Petrenz & Puls (2000) in simulations of winds from rotating hot stars. The steep acceleration of hot star winds as predicted by radiatively-driven wind theory requires a thorough treatment of the small subsonic region confined to the photosphere, specifically because it is in this region that the mass loss rate is set (Castor et al. 1975). To keep the computation time of our simulations to a reasonable value, we decided to fix the density and the velocity at the surface of the primary, allowing the use of a lower grid resolution. The mass loss rate of the primary is then set by the user rather than being a solution of the calculation. In the case of 1D simulations of hot star winds, this would be highly unorthodox, but in our present study, the primary has a very ellipsoidal surface, possesses a zero gravity point and is likely to be gravity darkened. In other words, we believe that the proper treatment of such a hot star surface and wind is beyond the scope of this paper - in fact such an exercise defies even the current best models of hot star winds - so that our choice is not such a bad compromise (Friend & Castor 1982; Owocki et al. 1996).

Hot stars drive outflows from the photosphere out to infinity by imparting a radiative acceleration on the atmospheric material that supersedes the local gravitational acceleration. In the phenomenon of mass transfer, it is the *thermal pressure* within the outer layers of the stellar envelope that lead to an outflow in the region where the gravitational step is minimum, i.e. the vicinity of the first Lagrangian point. Thus, the dense photospheric material expands and accelerates through the L1 region and "falls" into the gravitational potential well of the secondary star. The velocity of the accretion stream through the L1 point is at most the sound speed, i.e. of the order of a few tens of km s^{-1} for hot stars, and its geometrical cross section is of the order of a

few degrees (Lubow & Shu 1975; Ritter 1988). Typical photospheric densities of hot stars are 10^{-10} g cm^{-3}, which would then correspond to a mass transfer rate of the order of few times $10^{-6} M_\odot$ yr^{-1}. Such a value will be adopted in most of the simulations discussed in §3. However, there is evidence from binary star evolutionary calculations that mass transfer occurs routinely with a much larger magnitude of the order of $10^{-3} M_\odot$ yr^{-1}. Physically, this can occur through an increase in density or cross section of the accretion stream, alternatives we investigate with our radiation-hydrodynamics model and discuss in §3.2 and §3.3.

For our simulations, we assume both mass transfer and stellar wind mass loss rates of the primary and secondary stars. To simulate the wind from the secondary, we choose a surface density such that the sound-speed inflow of material at the boundary corresponds to the mass loss rate as calculated with identical stellar and opacity parameters but with a high spatial resolution (done separately in a 1D simulation), and using reference parameters from Kudritzki et al. (1989). Each of our simulations is first performed until a stationary solution is found for both winds. Once this steady-state is reached, we turn on the mass transfer. This takes the form of a sound-speed inflow of mass from the primary surface at the L1 location, with specified density and cross-section. These parameters are chosen so that they cover the range of mass transfer rates predicted by stellar evolutionary calculations. Note that the problem we are trying to tackle here shares very little common ground with previous radiation-hydro simulations of mass transfer by Roche-lobe overflow, which focused on the case of white dwarfs, neutron stars, Algol systems, where the magnitude of the mass transfer is always feeble, i.e. $\sim 10^{-7} M_\odot$ yr^{-1}(Blondin et al. 1995; Boroson et al. 2001).

For the outer boundary, we clearly have an outflow if we treat exclusively the stellar winds. It was not clear whether such boundary type was appropriate for the simulations including mass transfer. However in all simulations performed, we find that any material reaching the outer edge of the grid possesses a velocity in excess of the escape value, ensuring that the choice of outflow for the outer boundary is adequate. Note that the staircase inflow boundary describing the surface of the primary is not perfectly handled (see Fig. 1) and leads to a spurious flow phenomenon in a few confined directions. This does not affect the gross fluid properties derived here.

We also have to treat the eventuality of the accretion stream impacting the secondary surface. The physics of the shock interface is very complex and cannot be modeled with the desired accuracy, especially with the low resolution of our simulations. We could have adopted different conditions that cover the extreme dynamical scenarios: material is allowed to freely penetrate the secondary surface, to do so at most with the sound speed or not at all (reflecting boundary). However, for simplicity, if material impacts the secondary star surface, the boundary type switches to reflecting.

For the calculation of the radiation force, we use two approaches. Either we cal-

culate the radiation force from a point star with a constant correction factor for the finite disk size, or we integrate the radiation force over the two stellar disks. We have found that the two methods lead to similar properties, for two reasons. First, we find that the radiation force on the accretion stream itself is only moderate (§3). Moreover, the binary system we study is so compact that the wind-wind-interaction region overlaps with the acceleration regions of both winds, i.e. there is no wind stagnation for which multi-ray calculation of the radiation force led to the discovery of the radiative braking phenomenon (Gayley et al. 1997). Hence, a single ray calculation of the radiation acceleration is performed according to

$$g_{rad}^L(r, \phi) = CF * \frac{k\sigma_e L_\star}{4\pi c r^2} \left[\frac{1}{\sigma_e \rho(r, \phi) v_{th}} \left(\mathbf{\vec{n}} \cdot \nabla (\mathbf{\vec{n}} \cdot \mathbf{\vec{v}})) \right) \right]^\alpha ,$$

where $\vec{n}$ is the unit vector centered either at the primary or the secondary origin and pointing towards the equatorial grid point (r, ϕ). The parameter CF represents the finite disk correction, taken to be $1/(1 + \alpha)$ for the two stars for simplicity. k and α are parameters describing the line opacity distribution, σ_e the electron scattering cross section (cm^2/g), v_{th} the thermal velocity of metal ions, c the speed of light and $\rho(r, \phi)$ $(\vec{v}(r, \phi))$ the density (velocity) at (r, ϕ) and in cgs units.

We also include the contribution from the centrifugal and Coriolis forces in the momentum equation. At the start of the computation, we calculate the centrifugal potential for all grid points, together with its gradient in the azimuthal and radial directions. It is then incorporated into the momentum equation in the same way as the pressure gradient. The Coriolis force is calculated using the coordinates of the center of mass and the gas parcel velocities with respect to it in a standard way.

4.3   Results

In this section, we discuss the results of our calculations. We investigate in particular the properties of the accretion stream in a number of simulations with different stellar wind mass loss and mass transfer rates (cf. Table. 4.2).

4.3.1   Varying radiation and wind momenta

The central question of our investigation is whether radiation and wind momenta can significantly affect the dynamics of the accretion stream generated by the Roche-lobe filling component. Therefore, we have performed various simulations adopting different primary star luminosities and mass loss rates, hence modifying the strength of the radiation field and the density of the wind emanating from it. This way, we investigate three scenarios: 1) the primary wind winning over the secondary's, 2) a

Table 4.1: Standard parameters of our simulations. Table 2 gives updates to those parameters that are modified for the calculations presented in §3

	$M_\star$ $(M_\odot yr)$	$L_\star$	$R_\star$	$\dot{M}$
Primary	$27\,M_\odot$	$1.8 \times 10^5\,L_\odot$	$15\,R_\odot$	$10^{-8}\,M_\odot\,yr^{-1}$
Secondary	$26\,M_\odot$	$1.5 \times 10^5\,L_\odot$	$11.8\,R_\odot$	$10^{-8}\,M_\odot\,yr^{-1}$
	Orbital separation	Period	ρ_{L1}	ϕ_{L1}
System	$40\,R_\odot$	$4\,d$	$10^{-8}\,g\,cm^{-3}$	3deg

Table 4.2: List of performed simulations and the respective values used for the key parameters. Sim 1–3 focus on the impact of varying wind properties (through wind and radiation momenta). Sim 4 treats the case of a bigger stream cross section and Sim 5–7 address the situation for an enhanced stream density. These changes are implemented by changing ϕ_{L1}, the half angular width of the stream as seen from the primary center, or the density at L_1. Scaling ρ_{L1} (ϕ_{L1}) by x scales the mass transfer by $x(x^2)$. Values between parentheses are to be understood as powers of ten.

	$\dot{M}_1$ $M_\odot\,yr^{-1}$	ρ_{L1} $g\,cm^{-3}$	ϕ_{L1} deg	$\dot{M}_{transfer}$ $M_\odot\,yr^{-1}$
1	1.(-6)	1.(-8)	3.	5.(-6)
2	1.(-8)	1.(-8)	3.	5.(-6)
3	5.(-9)	1.(-8)	3.	5.(-6)
4	1.(-8)	1.(-8)	10.	5.(-5)
5	1.(-8)	1.(-8)	3.	5.(-6)
6	1.(-8)	1.(-7)	3.	5.(-5)
7	1.(-8)	1.(-6)	3.	5.(-4)

wind balance between the two stars leading to the formation of a wind–wind collision zone, and 3) a situation where the secondary wind wins over the primary wind. For each of these three cases, we investigate what happens to the accretion stream using a moderate mass transfer rate ($5 \times 10^{-6}\,M_\odot\,yr^{-1}$). The results are shown in Figure 4.1.

In case 1) $\dot{M}_1$ is enhanced by a factor 100 and the luminosity of the primary by a factor of ten compared to the more realistic default values presented in Table 1. We observe in Fig. 1 that in this situation, the wind of the secondary star is completely overwhelmed. We find that the motion of the accretion stream is not impeded, nor is it modified in any significant way from a standard ballistic trajectory. For the fluid

densities concerned here, the stream momentum is orders of magnitude above that of the winds, which explains the disregard of the accretion stream with respect to the "ambient" medium. In this close binary system, this leads to a fully conservative mass transfer.

Case 2) corresponds to the situation where the wind momenta of both stars are equal ($\dot{M}_1 = \dot{M}_2$ and similar luminosity for both stars), giving rise to a wind-wind collision between the two binary components. It has been argued in the past that the collision interface, because it lies between L_1 and the secondary surface, could interfere and maybe prevent mass transfer from occurring. In our simulation, it is clear that the accretion stream is not at all affected by this colliding zone. The same argument as in case 1) applies, where essentially the density contrast favors the stream over the two winds and the colliding interface. An analogy that may help is to view such density contrasts as much bigger than that between air and water (at room temperature). So, case 2) robustly leads to conservative mass transfer.

In case 3), we make the wind of the primary artificially small by reducing $\dot{M}_1$ to half the secondary's value. This situation would apparently be unfavourable to the primary's mass transfer, but again, for similar arguments as used in case 2) and 1), the wind from the secondary is no match for the dense accretion stream.

This leads us to conclude that the radiation and wind momenta are totally irrelevant for the general dynamics of the accretion stream, even in the situation where the mass transfer rate is moderate (5×10^{-6} $M_\odot$ yr^{-1}). Hence, in such close binary systems, our simulations strongly advocate conservative mass transfer.

4.3.2   Varying the mass transfer rate

As discussed in §2, the mass transfer rate can vary enormously during the evolution of a massive binary system. We investigate in this section the various ways such a mass transfer rate could be enhanced, namely by means of an increased density or geometrical cross section. We devote less attention to the case of lower rates than adopted in the previous section because they are doomed to play a weaker role, the accretion through direct impact of the companion *wind* potentially becoming an efficient alternative.

Varying the stream cross section

As discussed in the introduction to this section, a change in stream cross-section can amplify the amount of transfered mass by at most a factor of a few. We have run a number of simulations increasing the value of this cross section up to 20 deg (sim 4). While this seems a lot, one needs to remember that given the low density in the outer envelope of the star, at the onset of mass transfer, the corresponding rate of mass loss through L1 will likely be small. We anticipate that the stellar envelope will

continue growing beyond the Roche surface, until the dense layers located deeper in the envelope near the L1 region lead to a strong increase in mass transfer and the stabalisation of the envelope. During this transition, the stream could indeed be much broader than the values suggested in Ritter (1988). Our simulations demonstrate that this case is a hybrid. A large fraction of the accretion stream impacts the secondary surface, while the rest creates a colliding interface with the secondary's outflow. This fraction of interacting material is however small and therefore leads only to a minor departure from conservative mass transfer.

Varying the stream density

We have performed simulations for L1 densities a factor ten and a hundred higher than in §3.1 (Sim 5, 6 and 7). The momentum contrasts between the stream and the winds are even larger than in §3.1, and we find that the simulations, as expected, re-enforce the conclusion already made before. Namely, for the high mass transfer rates ($\sim 10^{-3} M_\odot \, \text{yr}^{-1}$) at which most of the mass from the primary is lost during the Case A mass transfer, the winds and radiation from either component have no effect of the accretion stream.

4.4 Discussion and conclusion

We have investigated the importance of radiation and wind momenta on the dynamical behaviour of accretion streams produced by overflow of the Roche-lobe filling component in a binary system. We performed radiation-hydrodynamic simulations of a typical young, close (4 day period) and massive binary system, calculating explicitly the radiation force and wind properties for each component. We discussed situations for the different mass transfer rates encountered in evolutionary calculations for massive binary systems (Wellstein 2001), as well as the occurrence of different wind momentum balance.

The central result of our calculation is that the dynamics of mass transfer in massive close binary stars is not affected in any noticeable way by the radiation and wind momenta from each luminous component. These latter mechanisms cannot therefore be at the origin of the non-conservative mass transfer required to explain the observed mass ratios of many Wolf-Rayet binaries.

The reader may find surprising that the radiation force does not modify the dynamical behaviour of an accretion stream. Although the radiation force efficiency is complex because it depends on the local velocity gradient and therefore on the dynamics itself, its dependence on the inverse of the density is really what makes it so ineffective here. The source of confusion on the importance of the radiation force in massive close binary systems could possibly arise from the failure to realise that important mass transfer rates for the evolution of those systems are of the order of

$10^{-3} M_\odot \, \mathrm{yr}^{-1}$, corresponding to density regimes orders of magnitude beyond those of hot star winds where the radiation acceleration is admittedly crucial. One must also bear in mind that this mass transfer occurs through a restricted region of space whilst stellar winds occur in principle from all stellar surface locations. Thus, for a mass transfer and wind mass loss of identical magnitude correspond a stream density a factor $1/\sin^2(\Phi_{L1}/2)$ greater than the wind's, simply from geometrical arguments.

Finally, we anticipate that in wider binary systems, the dilution of the accretion stream through spatial expansion could lead to a progressive "switch-on" of the importance of radiation and wind momenta, when and if the stream density becomes comparable to the standard wind density of the accreting star (as derived in single-star radiation-hydrodynamics simulations). This would offer an explanation for non-conservative mass transfer in wide massive binary systems.

Acknowledgements
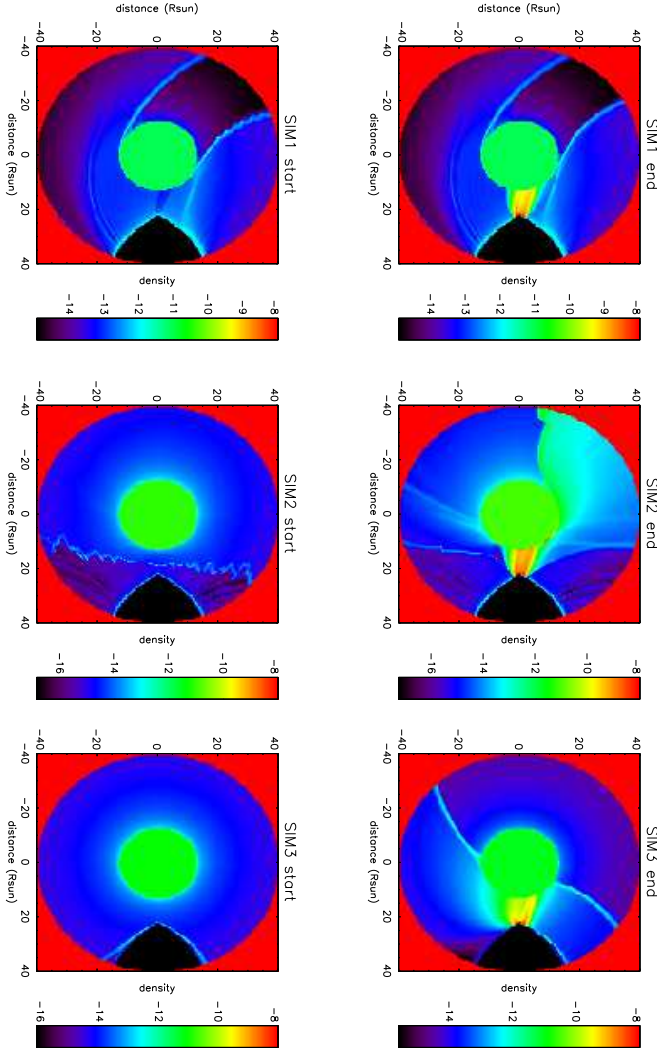
Figure 4.1: **(Left column:)** Sequence of gray scale images showing the logarithm of the density of the fluids surrounding the two stars (steady state is reached). The details for each simulation from 1 to 3 are given in Table 4.2. **(Right column:)** Same as above after mass transfer has been switched on for about 100ksec (the images do not correspond to a steady state, which will not necessarily be reached before some fraction of the system evolutionary time scale). The secondary star surface does not permit inflow in the simulations shown here.

Chapter 5

Which Massive stars are Gamma-Ray Burst Progenitors?

Abstract. The collapsar model for gamma-ray bursts requires three essential ingredients: a massive core, a removed hydrogen envelope, and a high enough core specific angular momentum. We explore up-to-date massive star evolutionary models of solar metallicity in order to find out which massive star physics is capable of producing these ingredients. In particular, we investigate the role of hydrodynamic and magnetic internal angular momentum transport and binary mass and angular momentum transfer. To pursue this, we compute evolutionary models of rotating single stars, and of binary systems which include rotational processes for both stars. Neglecting magnetic fields, we show that the cores of massive single stars can maintain a high specific angular momentum ($j \sim 10^{17} \mathrm{cm}^2 \mathrm{s}^{-1}$) when evolved with the assumption that mean molecular weight gradients suppress rotational mixing processes. In binary systems which undergo mass transfer during core hydrogen burning the mass receiving star gains large amounts of high angular momentum material, which leads to a spin-up of the core. However, we find that this does not lead to cores which rotate faster than in single stars, but merely compensates for the tidal angular momentum loss due to spin-orbit coupling, which leads to synchronous rotation before the mass transfer event. We show that some accretion stars become Wolf-Rayet stars towards core helium exhaustion and form CO-cores which are massive enough to form a black hole. We also present models which include magnetic fields produced due to differential rotation and internal angular momentum transport by magnetic torques (Spruit 2002). While magnetic single star models are known to develop rather slowly rotating cores (Heger et al. 2002) — with specific angular momenta close to those in observed young pulsars ($j \sim 10^{14} \mathrm{cm}^2 \mathrm{s}^{-1}$), we investigate the capability of magnetic torques to efficiently pump angular into the cores of accreting stars. While this mechanism is found to work, the magnetic coupling of core and envelope after the accretion star ends its core hydrogen burning leads to slower rotation $j \sim 10^{15-16} \mathrm{cm}^2 \mathrm{s}^{-1}$) than in the non-magnetic case. We conclude that our binary models without magnetic field can reproduce stellar cores with a high enough specific angular momentum ($j \geq 3 \cdot 10^{16} \mathrm{cm}^2 \mathrm{s}^{-1}$) to produce a collapsar and a GRB. However, if magnetic field is taken into consideration, GRBs at near solar metallicity need to be produced in rather exotic binary channels, or the magnetic effects are currently overestimated in our models. The latter would require a significant angular momentum loss of iron cores which form neutron stars, either during collapse and supernova explosion, or shortly thereafter.

authors: Jelena Petrovic, Norbert Langer, Sung-Chul Yoon, Alexander Heger
Submitted to A&A

5.1   Introduction

It is currently believed that the so called long gamma-ray bursts (GRBs), i.e. those which last longer than about 1 s, are produced by dying massive stars: the GRBs occur at cosmological distances and require energies compatible with the binding energies of stellar mass black holes. From studies of their host galaxies it was concluded that they occur in or close to star forming regions. Several of them are associated with a Type Ic supernova, thought to display the explosion of a massive Wolf-Rayet star. And finally, their afterglows show signatures of the shaping of the circumstellar medium by a massive progenitor star (van Marle et al. 2004). The most widely used model of GRB production in the context of black hole formation in a massive single star is the so called collapsar model (Woosley 1993a).

A collapsar is a massive ($M_{in}{\sim}35\text{-}40M_\odot$ Fryer 1999) rotating star whose core collapses to form a black hole (Woosley 1993b; MacFadyen & Woosley 1999). If the collapsing core has enough angular momentum ($j{\geq}3{\cdot}10^{16}\text{cm}^2\text{s}^{-1}$ MacFadyen & Woosley 1999) an accretion disk will be formed around the black hole. The accretion of the rest of the core at accretion rates up to $0.1M_\odot\text{s}^{-1}$ by the newly-formed black hole is thought to be capable of producing a collimated highly relativistic outflow. In case the star is devoid of its hydrogen envelope, i.e. has a radius which is less or comparable to the duration of the central accretion (about 10 s) times the speed of light, a gamma-ray burst (GRB) accompanied by a Type Ib/c supernova may be produced. This releases large amounts of energy ($\sim10^{51}\text{erg s}^{-1}$) some of which is deposited in the low density rotation axis of the star. The collapsar models for gamma-ray bursts thus needs three essential ingredients: a massive core, a removed hydrogen envelope, and a high enough core specific angular momentum.

Heger et al. (2000b) have calculated models of a $25M_\odot$ star that could form a black hole by fallback (SN explosion occurs while the core forms a neutron star, but so much matter fails to escape and falls back onto the neutron star that it turns into a black hole). This star ends its life as a red supergiant with an iron core of $1.9M_\odot$, a helium core of $8.06M_\odot$, and a low density envelope of $6.57M_\odot$. They found that this star has sufficient angular momentum to form an accretion disk around the black hole which may lead to an asymmetric, jet-driven supernovae, or in the case that the star lost its hydrogen envelope, even a GRB can result. The rotating pre-supernova models of Heger et al. (2000a) predicted, for the mass range $10...20M_\odot$, an iron core angular momentum barely sufficient for the GRB production model through collapsar, with a trend of decreasing final specific angular momentum for larger initial mass. Heger et al. (2000a) showed also that specific angular momentum of the stellar core depends significantly on the inhibiting effect of the mean molecular weight gradient on rotational mixing processes. Only if it represent a barrier for rotational mixing and transport of angular momentum, the core does not lose large amounts of angular momentum during the evolution. Finally, the rotating pre-supernova models

of (Hirschi et al. 2004) predict about twice as much final core angular momentum as the models of Heger et al. (2000a).

These calculations left out the influence of a magnetic field that can significantly alter the angular momentum transport processes in the star, for example slowing down the helium core of the star during the red supergiant phase (Spruit & Phinney 1998). Single star pre-supernova models including angular momentum transport by magnetic torques, using the improved dynamo model of Spruit (2002), have been produced by Heger et al. (2004), with a clear result: although these models predict neutron star spins in the range displayed by young pulsars, the amount of angular momentum in their cores is one to two orders of magnitude less than what is required by the collapsar model of GRB production. The conclusion therefore must be that, if the dynamo model of Spruit (2002) is qualitatively right, massive single stars can not form GRBs within the collapsar model.

However, only one of one hundred collapsing massive stars needs to produce a GRB in order to explain their frequency. It seems therefore legitimate to explore collapsars in the frame of massive close binary evolution. Wellstein (2001) and Petrovic et al. (2004a) showed that during the mass transfer phase in a binary system, the secondary (accreting) star can spin up to close to critical rotation, i.e. surface layers of this star can gain large amounts of angular momentum. This angular momentum can be transported inward and increase the rotation rate of the stellar core. In this case, one can hope that the effects of magnetic fields would be helpful in spinning the core up, and that faster rotating cores might be reached than in the non-magnetic models.

In this paper, we investigate four different types of rotating massive star models, single and binary models, as well as magnetic and non-magnetic models. After briefly explaining our numerical method and physical assumptions in Sect. 5.2, we explore non-magnetic single and binary stars in Sect. 5.3. Sect. 5.4 presents our magnetic models, first single stars then binary evolution models. Our conclusions are summarized in Sect. 5.5.

5.2   Computational method

We compute detailed evolutionary rotating models of non-magnetic $20M_\odot$ and $42M_\odot$ single stars, and of a $42M_\odot$ single star with magnetic field included. Then we calculate the evolution of a non-magnetic and a magnetic binary system with rotating components of $M_{1,in}=56M_\odot$ and $M_{2,in}=33M_\odot$ and an orbital period p_{in}=6 days. We also compute models of a rotating $33M_\odot$ star that accretes matter at the end of its main sequence evolution, for the non-magnetic and magnetic case.

We use the evolutionary code developed by Braun (1998) on the basis of an implicit hydrodynamic stellar evolution code for single stars (Langer 1991, 1998). The treatment of convection and semiconvection have been described in Langer

(1991) and Braun & Langer (1995). Changes in chemical composition are computed using a nuclear network including pp chains, the CNO-cycle, and the major helium, carbon, neon and oxygen burning reactions. More details are given in Wellstein & Langer (1999) and Wellstein et al. (2001). Calculations are made with OPAL opacities (Iglesias & Rogers 1996). For all models, a metallicity Z=0.02 is adopted. The abundance ratios of the isotopes for a given element are chosen to have the solar meteoritic abundance ratios according to Noels & Grevesse (1993). The change of the orbital period due to mass transfer and stellar wind mass loss is computed according to Podsiadlowski et al. (1992), with a specific angular momentum of the stellar wind material calculated according to Brookshaw & Tavani (1993). The influence of the centrifugal force in the rotating models is implemented according to Kippenhahn & Thomas (1970).

Stellar wind mass loss for O stars is calculated according to Kudritzki et al. (1989). For hydrogen poor stars ($X_s < 0.4$) we used a relation based on the empirical mass loss rates of Wolf-Rayet stars derived by Hamann et al. (1995):

$$log(\dot{M}_{\mathrm{WR}}/\mathrm{M}_\odot \mathrm{yr}^{-1}) = -11.95 + 1.5 log L/L_\odot - 2.85 X_s. \qquad (5.1)$$

Since Hamann & Koesterke (1998) suggested that these mass loss rates may be overestimated, we calculated evolutionary models in which the mass loss rate given by Eq. 5.1 is multiplied by $1/3$.

Also, enhanced mass loss due to rotation is included:

$$\dot{M}/\dot{M}(v_{\mathrm{rot}} = 0) = 1/(1 - \Omega)^\xi, \qquad (5.2)$$

where Ω=$v_{\mathrm{rot}}/v_{\mathrm{crit}}$ and v_{crit}^2=$GM(1 - \Gamma)/R$ with Γ=L/L_{Edd}=$\kappa L/(4\pi cGM)$ is the Eddington factor, G is gravitational constant, M is mass, R radius, κ opacity, v_{rot} rotating velocity and v_{crit} critical rotational velocity (Langer 1998).

The transport of angular momentum in our code is formulated as a diffusive process:

$$\left(\frac{\partial \omega}{\partial t}\right)_m = \frac{1}{i}\left(\frac{\partial}{\partial m}\right)_t\left[(4\pi r^2\rho)^2 i\nu\left(\frac{\partial \omega}{\partial m}\right)_t\right]$$
$$-\frac{2w}{r}\left(\frac{\partial r}{\partial t}\right)_m\frac{1}{2}\frac{dlni}{dlnr}, \qquad (5.3)$$

where ν is the turbulent viscosity and i is the specific angular momentum of a shell at mass coordinate m. A parameter f_μ=0.05 is adopted for sensitivity of the rotationally induced mixing processes to the μ-gradient (Heger et al. 2000a).

At the surface of the star, the angular momentum contained in the layers which are lost due to stellar wind gets removed from the star:

$$\dot{J} = \dot{M}j_{spec} \qquad (5.4)$$

where j_{spec} is the average angular momentum at the surface of the star and $\dot{M}$ the stellar wind mass loss rate. The turbulent viscosity ν is determined as the sum of the convective and semiconvective diffusion coefficients and those from rotationally induced instabilities (dynamical shear, Solberg-Høiland, secular shear and Goldreich-Schubert-Fricke instability and Eddington-Sweet circulation). Rotationally induced mixing processes and angular momentum transport through the stellar interior are described in detail by Heger et al. (2000a).

The code calculates the simultaneous evolution of two stellar components of a binary system and computes mass transfer within the Roche approximation (Kopal 1978). Mass loss from the Roche lobe filling component through the first Lagrangian point is given by Ritter (1988) as:

$$\dot{M} = \dot{M}_0 \exp(R - R_l)/H_p \quad (5.5)$$

with $\dot{M}_0 = \rho v_s Q/\sqrt{e}$, where H_p is the photospheric pressure scale height, ρ is the density, v_s the velocity of sound and Q the effective cross-section of the stream through the first Lagrangian point according to Meyer & Meyer-Hofmeister (1983). The time scales for synchronization and circularization of the binary orbit as well as spin-orbit coupling are given by Zahn (1977). The specific angular momentum of the accreted matter is determined by integrating the equation of motion of a test particle in the Roche potential (Wellstein 2001, accretion stream impacts directly on the secondary star).

We calculate the evolution of binary systems in detail until Case AB mass transfer starts. Then we remove the hydrogen rich envelope from the primary, until only 5% of the hydrogen is left in the envelope. This is the point where we assume that the primary shrinks and Case AB stops. On the other side, we calculate the secondary star assuming accretion with a mass transfer of $10^{-4} M_\odot \text{yr}^{-1}$. We calculate the Kelvin-Helmholtz time scale of the primary on the beginning of Case AB mass transfer:

$$t_{KH} = 2 \cdot 10^7 M_1{}^2/(L_1 R_{l1}) yr, \quad (5.6)$$

where M_1, L_1 and R_{l1} are mass, luminosity and Roche radius (in Solar units) of the primary star at the onset of Case AB mass transfer. Mass transfer rate is:

$$\dot{M}_{tr} = (M_1 - M_{He})/t_{KH} \quad (5.7)$$

where M_{He} is the mass of the helium core with $\sim$5% of hydrogen on the surface, i.e. the initial WR mass. We calculate the orbit change assuming constant mass transfer rate calculated by Eq. 5.7 and an average accretion efficiency (β) which is the same as for the fast phase of Case A, since Case AB also happens on the thermal time scale. Matter that has not been accreted on the secondary leaves the system with a specific angular momentum which corresponds to the secondary orbital angular momentum (King et al. 2001). Stellar wind mass loss is neglected.

We follow the evolution of the binary system, again in detail, until the primary finishes carbon core burning. After this we assume that the system is disrupted by the SN explosion of the primary and we model the secondary further as a single star. Stellar wind mass loss for red supergiants is given by Nieuwenhuijzen & de Jager (1990).

Magnetic fields generated by differential rotation are included according to Spruit (2002). The effective radial viscosity produced by the magnetic field is:

$$\nu_{re} = \frac{\nu_{e0}\nu_{e1}}{\nu_{e0} + \nu_{e1}} f(q), \tag{5.8}$$

where

$$\nu_{e0} = r^2 \Omega q^2 \left(\frac{\Omega}{N_\mu}\right)^4, \tag{5.9}$$

$$\nu_{e1} = r^2 \Omega max \left[\left(\frac{\Omega}{N_T}\right)^{1/2}\left(\frac{\kappa}{r^2 N_T}\right)^{1/2}, q^2 \left(\frac{\Omega}{N_T}\right)^4\right], \tag{5.10}$$

where r is the radial coordinate, Ω the rotation rate of the star, N_μ the compositional buoyancy frequency, N_T the thermal part of buoyancy frequency, q is the rotational gradient and q_{min} is minimum rotational gradient necessary for the dynamo to operate:

$$f(q) = 1 - q_{min}/q, \text{for(q} > \text{q}_{min}), \tag{5.11}$$

and

$$f(q) = 0, \text{for(q} \leq \text{q}_{min}). \tag{5.12}$$

The factor f causes the stress to vanish smoothly as the gradient of the rotation rate approaches the minimum value required for dynamo action.

Fluid motions involved in the dynamo process also imply a certain amount of mixing. The effective diffusivity is given as:

$$D_e = \frac{D_{e0}D_{e1}}{D_{e0} + D_{e1}} f(q), \tag{5.13}$$

where $f(q)$ is defined by Eq.(11) and

$$D_{e0} = r^2 \Omega q^4 \left(\frac{\Omega}{N_\mu}\right)^6, \tag{5.14}$$

$$D_{e1} = r^2 \Omega max \left[\left(\frac{\Omega}{N_T}\right)^{3/4}\left(\frac{\kappa}{r^2 N_T}\right)^{3/4}, q^2 \left(\frac{\Omega}{N_T}\right)^6\right]. \tag{5.15}$$

5.3 Models without magnetic field

5.3.1 Single stars

It was shown by Meynet & Maeder (1997) and Heger et al. (2000a) that transport of angular momentum in stellar interiors depends strongly on the efficiency of the inhibition of the rotationally induced mixing processes by μ-gradients. When rotationally induced mixing processes are not inhibited by μ-gradients, stellar rotation remains close to rigid rotation. The star loses matter from the surface which carries away angular momentum. Layers beneath the lost ones expand, and due to local angular momentum conservation, spin down. The star reestablishes rigid rotation by transporting angular momentum from the core to the surface. When the rotationally induced mixing processes are inhibited by the μ-gradient, angular momentum can not be efficiently transported between the core and the envelope. Result is differential rotation between these two stellar regions. In this paper we present models which include the inhibiting effect of μ-gradient on rotationally induced mixing processes.

We calculated the evolution of a $20M_\odot$ star until the end of core carbon burning. This star is a rigidly rotating star on the ZAMS (Fig.5.1, three dots-dashed line) with an initial surface velocity of v_{surf}=200 km s^{-1}, which is a typical value for these stars (Heger et al. 2000a). During its hydrogen core burning phase, this star loses mass due to a stellar wind ($\sim 10^{-8}M_\odot\mathrm{yr}^{-1}$). Matter lost from the stellar surface carries away angular momentum, the surface layers spin down, but there is no efficient transport of angular momentum between the core and the envelope, so the core does not spin down significantly. At the time of helium ignition (Fig.5.1,dot-dashed line), the specific angular momentum of the core is $j\sim 10^{17}\mathrm{cm}^2\mathrm{s}^{-1}$ at $3M_\odot$ (further in the paper, specific angular momentum values are always given at $3M_\odot$, since that is the mass of the final core before supernova explosion). After core hydrogen exhaustion, the star evolves into a red supergiant, its core contracts while the envelope expands. This leads to a spin-up of the core and a spin-down of the envelope. The envelope is convective and rotating almost rigidly with a very low rotational velocity (~ 0.1 km s^{-1}). The core is rigidly rotating with a maximum rotational velocity of ~ 130 km s^{-1}. The core and the envelope are separated by layers that have a large μ-gradient. This suppresses rotationally induced mixing and angular momentum is not being efficiently transported, so the core is not slowed down by the slow rotation of the envelope. At the end of helium core burning the specific angular momentum of the core is $j\sim 5\cdot 10^{16}\mathrm{cm}^2\mathrm{s}^{-1}$ (Fig.5.1, dotted line). During further evolution, i.e. core carbon burning, the stellar core does not lose any significant amounts of angular momentum.

To investigate the behaviour of higher mass stars, we modelled the evolution of a $42M_\odot$ star with the same initial surface rotational velocity v_{surf}=200 km s^{-1}. The star is a rigidly rotating star on the ZAMS with the specific angular momentum

profile shown on Fig.5.3 (dot-dashed line). As we already explained for the previous example, the star loses mass due to a stellar wind ($\sim 10^{-7} M_\odot \text{yr}^{-1}$). Since the stellar wind mass loss rate is one order of magnitude higher than for a $20 M_\odot$ star, the $42 M_\odot$ star loses more matter and angular momentum during the core hydrogen burning phase. When helium ignites in the core, the specific angular momentum at $3 M_\odot$ is $\sim 8 \cdot 10^{16} \text{cm}^2 \text{s}^{-1}$. The star becomes a $\sim 38 M_\odot$ red supergiant with central helium burning in a convective core of $\sim 12 M_\odot$ and a convective envelope of $\sim 20 M_\odot$. Due to stellar wind mass loss of $\sim 10^{-4} M_\odot \text{yr}^{-1}$, the mass of the envelope rapidly decreases and reaches $\sim 10 M_\odot$ at the end of our calculations.

We follow the evolution of this star until it burned $\sim 30\%$ of the helium in its core. The specific angular momentum of the core (at $3 M_\odot$) at that moment is $\sim 6.5 \cdot 10^{16} \text{cm}^2 \text{s}^{-1}$. If we assume that the angular momentum of the core decreases further during helium core burning with the same rate, the specific angular momentum of the core at the moment of helium exhaustion would be $\sim 3.5 \cdot 10^{16} \text{cm}^2 \text{s}^{-1}$. We see in Fig.5.1 that there is no angular momentum loss from the core during core carbon burning, so we can conclude that this star might produce a collapsar and in case that the hydrogen envelope is lost during the red the supergiant phase, a gamma-ray burst can be the result.

For a rigidly rotating body of constant density ρ_0, the total angular momentum $J(m)$ enclosed below the mass coordinate m is $J(m) = \int_0^M j(m')dm'/m^{5/3}$. In Fig.5.2 and Fig.5.4 we plotted the logarithm of $J(m)/m^{5/3}$ as a function of mass as well as the lines of $J = const$. If angular momentum is transported throughout the surface defined by a mass coordinate m, $J(m)$ drops. If no such transport occurs, $J(m)$ remains constant. If a line of constant J is followed from one evolutionary stage to another, it can be seen to what mass coordinate the angular momentum has been transported in the star during the time between the two evolutionary stages.

5.3.2   Binary systems

If a star evolves in a binary system and accretes matter from the companion, its surface angular momentum increases. If this angular momentum can be efficiently transported through the stellar interior, the star may evolve into a red supergiant that has a rapidly spinning core with sufficient specific angular momentum to produce a collapsar.

To check if accretion can add enough angular momentum to the core, we modelled the evolution of a rotating binary system with initial masses of $M_{1,in} = 56 M_\odot$ and $M_{2,in} = 33 M_\odot$ and an initial orbital period of $p_{in} = 6$ days. The binary system quickly synchronizes during the main sequence evolution. Due to this synchronization, both stars lose angular momentum and their initial surface rotational velocities are 92 km s^{-1} for the primary and 64 km s^{-1} for the secondary which is much slower than the typical values for single stars of these masses (Heger et al. 2000a).
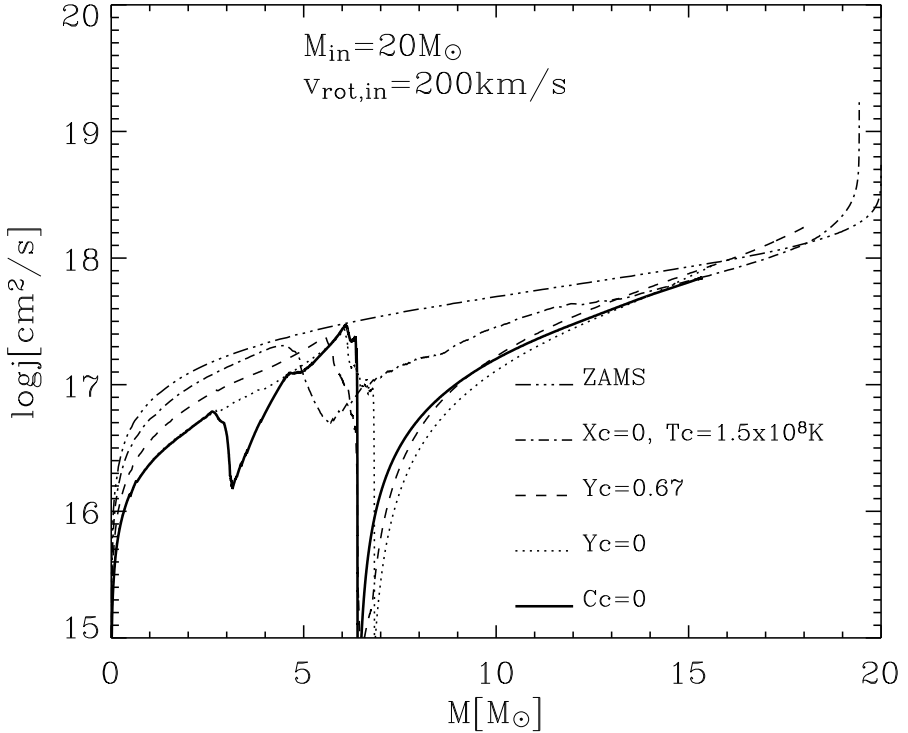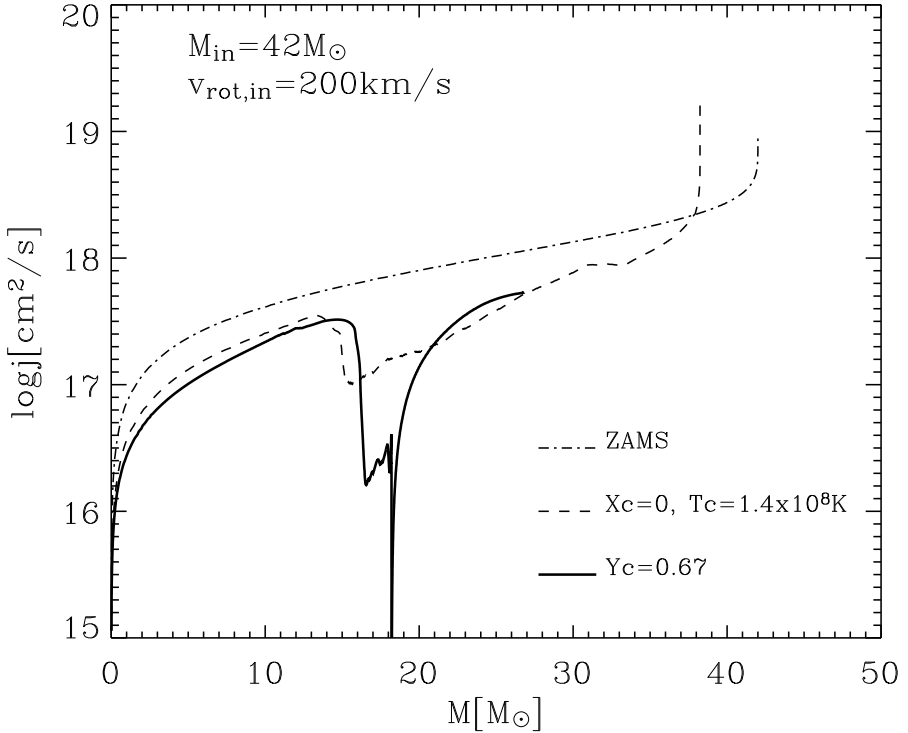
Figure 5.1: Specific angular momentum profiles of a $20M_\odot$ single star on the hydrogen ZAMS (three dots-dashed line), when helium ignites in the core, (dot-dashed line), when the central helium abundance is 67% (dashed-line), in the moment of core helium exhaustion (dotted line) and at core carbon exhaustion (solid line.)

This means that stars in binary systems lose a significant amount of angular momentum due to synchronization. The amount of lost angular momentum increases with the initial orbital period.

Evolutionary tracks of the primary and the secondary star are given in Fig.5.5 and Fig.5.6, respectively. The primary is initially the more massive star, it evolves faster and fills its Roche lobe during hydrogen core burning. The binary system enters Case A of mass transfer (dotted line, Fig. 5.5). The primary loses matter with a high mass transfer rate ($\dot{M}_{tr}^{max}\sim3.2\cdot10^{-3}M_\odot yr^{-1}$) and decrease in luminosity. During the fast phase of Case A mass transfer, the primary loses $\sim19M_\odot$ and the secondary accretes only about 15% of that matter due to the stellar wind mass loss caused by rotation close to break-up (Petrovic et al. 2004a). After the fast process of Case A mass transfer, the primary continues expanding on a nuclear time scale and transferring
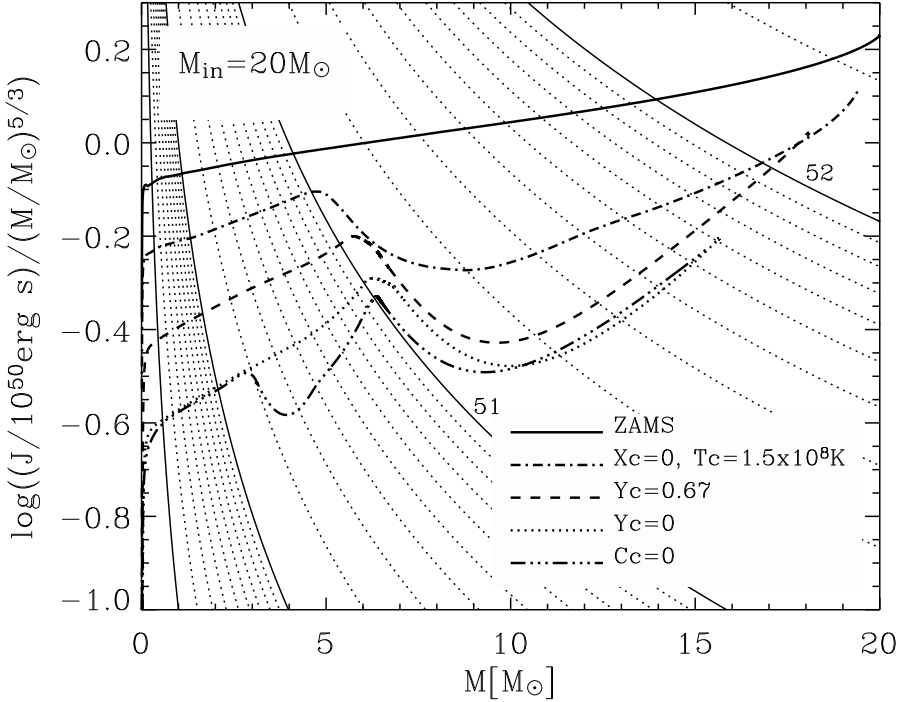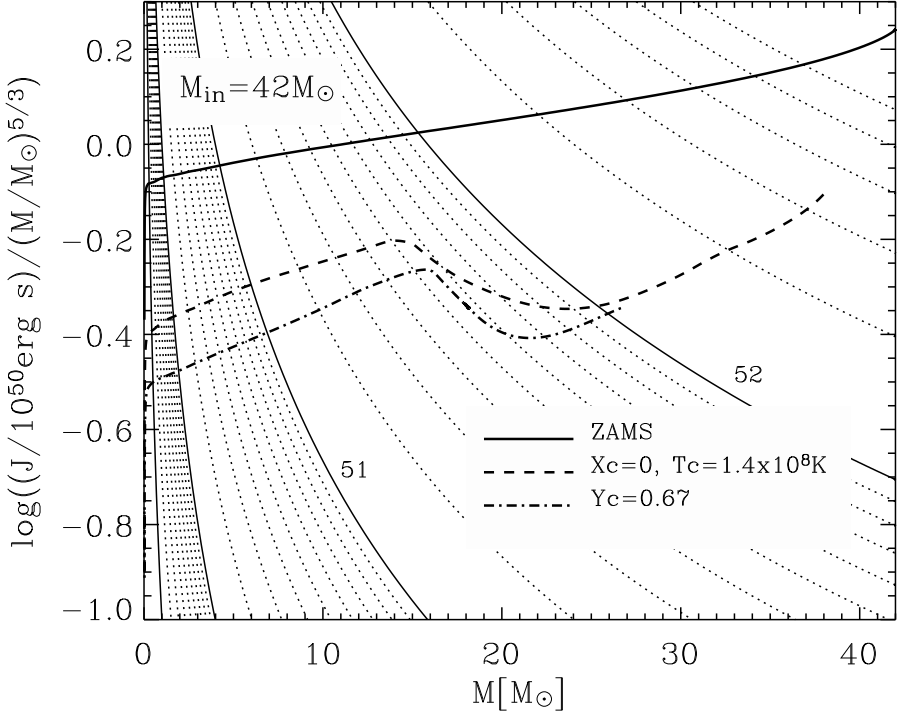
Figure 5.2: Logarithm of the integrated angular momentum $J(m) = \int_0^M j(m')dm'$ divided by $m^{5/3}$, as a function of the mass coordinate m for a $20M_\odot$ star for the same evolutionary stages as shown in Fig.5.1. The thin lines give a logarithmic scale of levels of constant J labelled with $\log(J/(\text{erg s}))$.

mass onto the secondary star with mass transfer rate of $\sim 10^{-6} M_\odot \text{yr}^{-1}$ (slow phase of Case A). At the end of core hydrogen burning the primary contracts and thus Roche lobe overflow (RLOF) stops. When the primary starts hydrogen shell burning ($M=16.6M_\odot$) it expands again, fills its Roche lobe and Case AB mass transfer starts. We assume that this mass transfer stops when the WR star has 5% of hydrogen on its surface ($M_{WR}(X_s=0.05)=14.8M_\odot$). More details about the evolution of this system up to WR+O phase can be seen in Petrovic et al. (2004a). As explained in Sect.5.2 we continue following the evolution of the binary system with a hydrogen-free WR star. The dashed line on Fig.5.5 connects the last calculated model at the onset of Case AB and the first calculated model when the primary is a hydrogen-free WR star. The initial hydrogen-free WR star is $M_{WR}=12.8M_\odot$ with an effective temperature of $\sim 1.2\cdot 10^5$K, and it loses $\sim 8M_\odot$ due to WR mass loss during core helium burning. Due to this mass loss, the luminosity of the primary decreases (dash-dotted line Fig.5.5). The primary ends carbon core burning (dot-dashed line Fig.5.5) as ~ 4.5

Figure 5.3: Specific angular momentum profiles of a $42M_\odot$ single star on the hydrogen ZAMS (dot-dashed line), when helium ignites in the center (dotted line), and when the central helium abundance is 67% (solid line).

solar mass star. The orbital period of the binary system is ~ 13.5 days when the primary explodes in a supernova.

The secondary begins its evolution as a $33M_\odot$ core hydrogen burning star. It accretes $\sim 3M_\odot$ during the fast phase and $\sim 4M_\odot$ during the slow phase of Case A mass transfer. Due to this mass gain, the luminosity of the secondary increases (Fig.5.6). As we already mentioned, the primary loses $\sim 1.8M_\odot$ during Case AB. We assume the same average accretion efficiency during this mass transfer as during the fast phase of Case A mass transfer (β=0.15), since they both take place on the thermal time scale. This means that the secondary accretes $\sim 0.25M_\odot$ and after Case AB mass transfer, it is still a core hydrogen burning star, more massive than at the beginning of its main sequence evolution ($39.25M_\odot$). After the secondary exhausted all hydrogen in the core, it contracts and increase its luminosity and effective temperature. Due to the increase of temperature in the envelope, the star ignites

Figure 5.4: Logarithm of the integrated angular momentum $J(m)=\int_0^M j(m')dm'$ divided by $m^{5/3}$, as a function of the mass coordinate m for a $42M_\odot$ star for the same evolutionary stages as shown on Fig.5.3. The thin lines give a logarithmic scale of levels of constant J labelled with $\log(J/(\mathrm{erg\ s}))$.

hydrogen in a shell, expands and cools down drastically (dash-dotted line Fig.5.6, $R \approx 2300 R_\odot$, $T_{\mathrm{eff}} \approx 3500$K). Meanwhile, the core contracts further and the core temperature increases. Helium core burning starts when $T_c \approx 1.4 \cdot 10^8$K. We stopped detailed modelling when the secondary has $\sim 67\%$ of helium left in the core.

Fig.5.7 shows the evolution of the internal structure of the secondary from the ZAMS, through Case A and Case AB mass transfer and the red supergiant phase until $Y_c = 0.67$. The secondary starts its main sequence evolution as a $33M_\odot$ star with a convective core of $\sim 20M_\odot$. Rotationally induced mixing processes are taking place in the radiative envelope of the star. The secondary then accretes $\sim 3M_\odot$ during the fast phase and $\sim 4M_\odot$ during the slow phase of Case A mass transfer. Heavier elements accreted on the surface are being relocated by thermohaline mixing process and the convective core increases its mass ($\sim 25M_\odot$). The secondary becomes a rejuvenated $\sim 39M_\odot$ core hydrogen burning star in a WR+O binary system. The
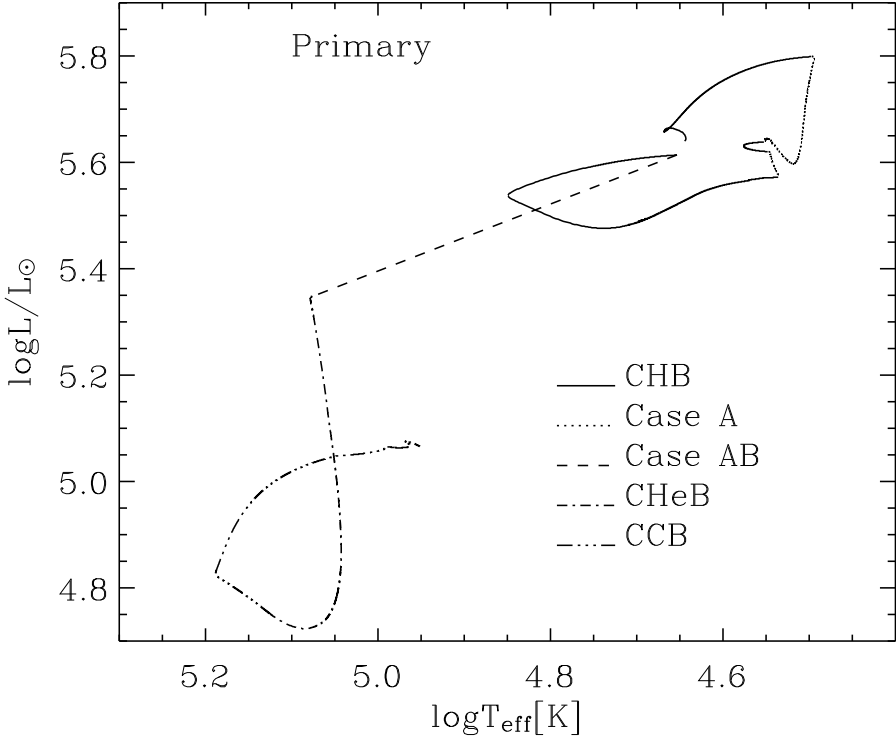
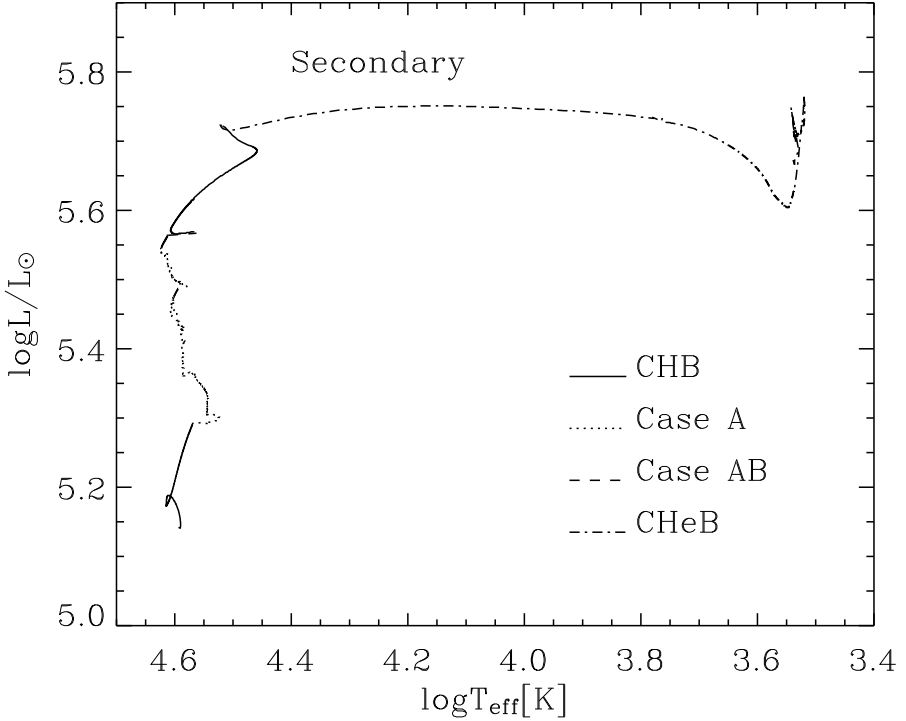Figure 5.5: Evolutionary track of the primary in HR diagram. Solid line: core hydrogen burning phase before and after Case A mass transfer. Dotted line: Case A mass transfer. Dashed line: connection between last calculated model at the onset of Case AB and first calculated model when the primary is a hydrogen-free WR star. Dash-dotted line: core helium burning phase. Dot-dashed line: core carbon burning phase.

system is likely to be disrupted by the explosion of the primary while the secondary is still a main sequence star. Details of the evolution of the internal structure of the secondary after the primary exploded are shown in Fig.5.8. After hydrogen is exhausted in the core, the secondary becomes a $\sim 37 M_\odot$ red supergiant with central helium burning in convective core of $\sim 12 M_\odot$ and a convective envelope of $\sim 20 M_\odot$. Due to stellar wind mass loss of $\sim 10^{-4} M_\odot \mathrm{yr}^{-1}$, the mass of the envelope rapidly decreases and reaches $\sim 10 M_\odot$ at the end of our calculations.

The modelled binary system starts its evolution with both components synchronized to the orbital rotation. The surface rotational velocity of the secondary star is ~ 64 km s^{-1}. When the fast Case A mass transfer starts, the secondary accretes matter from the primary with high mass transfer rates ($\sim 10^{-3} M_\odot \mathrm{yr}^{-1}$). This mat-

Figure 5.6: Evolutionary track of the secondary in the HR diagram. Solid line: core hydrogen burning phase before and after Case A and Case AB mass transfer. Dotted line: Case A mass transfer. Dash-dotted line: core helium burning phase. Dashed line: see Fig. 5.5.

ter carries angular momentum and spins up the top layers of the secondary star (Fig.5.9). The mass transfer rate during the slow phase of Case A is significantly lower ($10^{-6} M_\odot \mathrm{yr}^{-1}$) and the surface rotational velocity of the secondary increases to about $200 \, \mathrm{km \, s^{-1}}$. For Case AB we assumed a mass transfer rate of $\sim 10^{-4} M_\odot \mathrm{yr}^{-1}$ (Sect.5.2) and this spins up the surface of the secondary to $\sim 500 \, \mathrm{km \, s^{-1}}$. When the secondary spins up to close to critical rotation it starts losing more mass according to Eq. 2 . High mass loss decreases the net accretion efficiency and also removes angular momentum from the secondary star. The secondary star is also spun-down by tidal forces that tend to synchronize it with the orbital motion (Petrovic et al. 2004a). After Case AB mass transfer, the secondary will synchronize with the orbital motion in the WR+O binary system. After the SN explosion of the primary, the secondary becomes a red supergiant with a very slowly rotating envelope and its surface rotational velocity drops to less than $0.02 \, \mathrm{km \, s^{-1}}$.
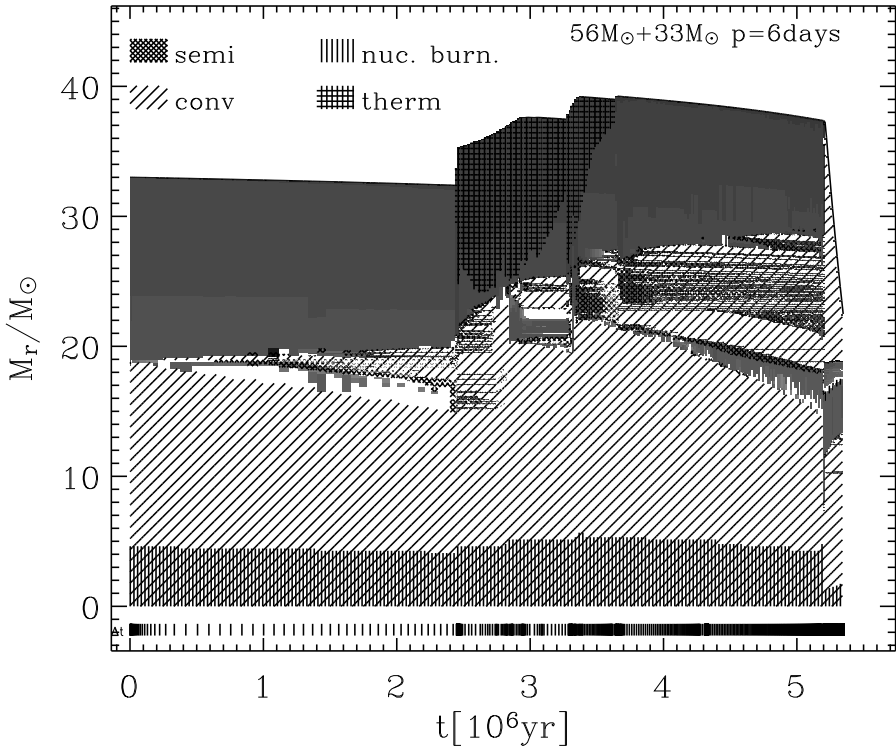
Figure 5.7: Evolution of the internal structure of a rotating $33M_\odot$ secondary from the ZAMS until red supergiant phase Y_c=0.67. Convection is indicated with diagonal hatching, semiconvection with crossed hatching and thermohaline mixing with straight crossed hatching. The hatched area at the bottom indicates nuclear burning. Gray shaded areas represent regions with rotationally induced mixing (intensity is indicated with different shades, the darker the colour, the stronger rotational mixing). The topmost solid line corresponds to the surface of the star.

Fig.5.10 shows rotational velocity profiles of the secondary star in different evolutionary phases. The surface of the secondary gains additional angular momentum during mass transfer, as we already explained. This angular momentum is transported through the stellar interior, and into the core. The result is that the stellar core spins faster on the helium ZAMS (Fig.5.10, three dots-dashed line) than at the beginning of hydrogen core burning (Fig.5.10, solid line). After this, the core is contracting and further increasing its rotational velocity, and the envelope is expanding and slowing down. When the central abundance of helium is around 67%, the maximum rotational velocity of the core is $\sim 100\ \text{km}\,\text{s}^{-1}$.

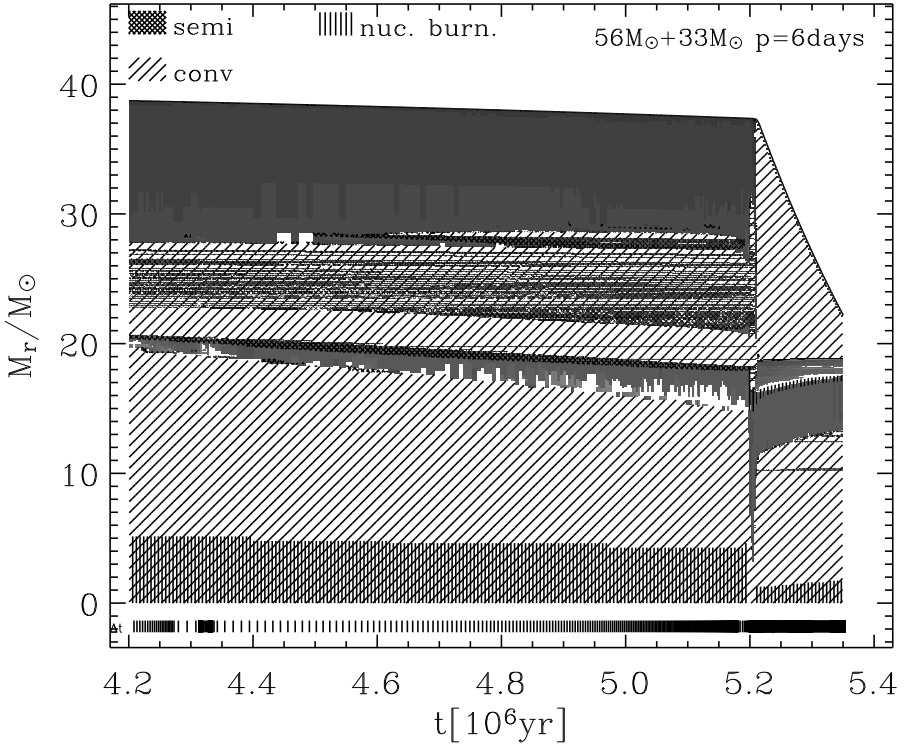Fig.5.11 shows specific angular momentum profiles of the secondary at different

Figure 5.8: Evolution of the internal structure of a rotating $33M_\odot$ secondary from SN explosion of the primary and disruption of the system. Convection is indicated with diagonal hatching, semiconvection with crossed hatching and thermohaline mixing with straight crossed hatching. The hatched area at the bottom indicates nuclear burning. Gray shaded areas represent regions with rotationally induced mixing (intensity is indicated with different shades, the darker the colour, the stronger rotational mixing). The topmost solid line corresponds to the surface of the star.

points of its evolution. The specific angular momentum of the secondary increases significantly due to fast Case A mass transfer (Fig.5.11, dotted line). After this the secondary loses angular momentum due to stellar wind mass loss, but also gains certain amount through slow Case A and Case AB mass transfer (Fig.5.11, dashed and dot-dashed line). The result is that the core has a larger specific angular momentum when central helium burning starts than at the beginning of hydrogen core burning. After core hydrogen exhaustion, the secondary evolves into a red supergiant, the core contracts and the envelope expands. This leads to a spin-up of the core and a spin-down of the envelope. The specific angular momentum of the core at $3M_\odot$ is $\sim 5.5 \cdot 10^{16} \mathrm{cm}^2 \mathrm{s}^{-1}$ (Fig.5.11, three dot-dashed line). The envelope is convective and
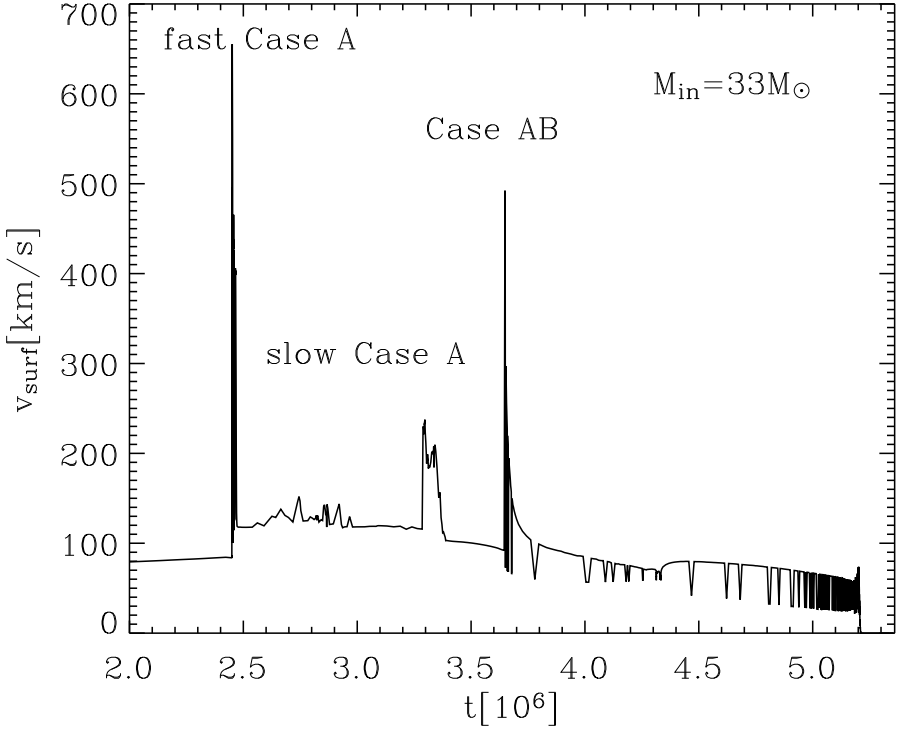
Figure 5.9: Surface rotational velocity of the secondary star. Matter transfered from the primary with high mass transfer rate $\sim 10^{-3}$-$10^{-4} M_\odot yr^{-1}$ during the fast phase of Case A and Case AB spins up the surface layers of the secondary up to 500-700 km s^{-1}. During the slow phase of Case A mass transfer rate is lower ($\sim 10^{-6} M_\odot yr^{-1}$) and surface rotational velocity increases up to $\sim$200 km s^{-1}. After Case AB mass transfer the secondary synchronizes with the orbital motion in the WR+O binary system. After the SN explosion of the primary, the secondary star evolves into a red supergiant with slowly rotating envelope of $\sim$0.02 km s^{-1}.

slowly rotating ($\sim$0.02 km s^{-1}). The core is rigidly rotating with maximum rotational velocity of $\sim$100 km s^{-1}. The core and the envelope are separated by layers that have a high μ-gradient. Angular momentum is not being efficiently transported through these layers, so the core is not slowed down by the slow rotation of the envelope. When a third of the central helium supply is exhausted, the core (at 3M$_\odot$) has a specific angular momentum of $\sim$5·10^{16}cm^{2}s^{-1}. If we assume that the angular momentum of the core decreases further during helium core burning with the same rate, specific angular momentum of the core at the moment of helium exhaustion is expected to be $\sim$4·10^{16}cm^{2}s^{-1}. As we have already seen for single stars, there is no angular momentum loss from the core during core carbon burning, so we can
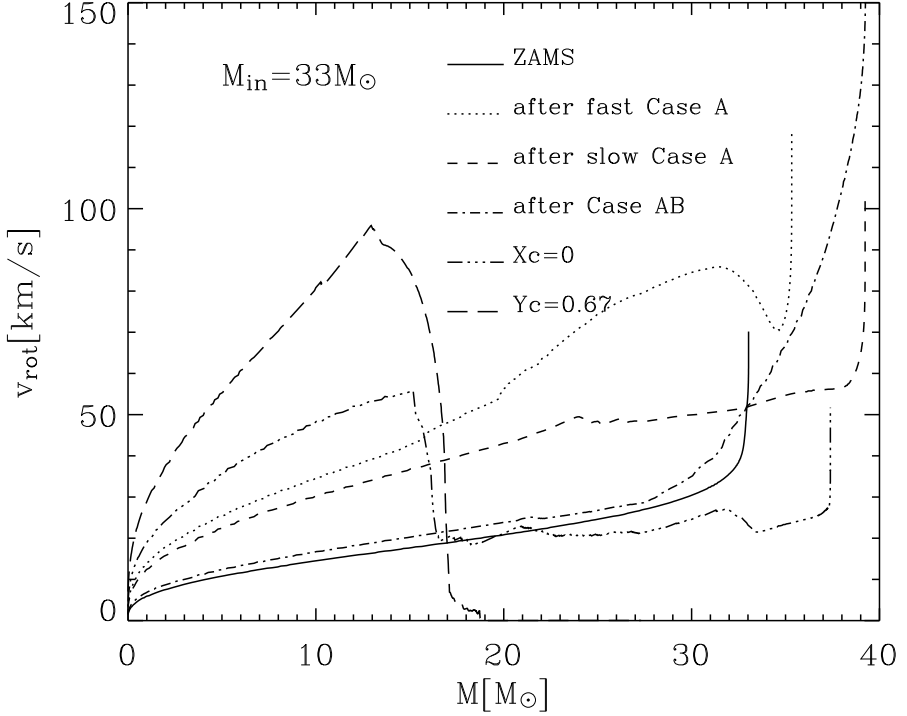
Figure 5.10: Rotational velocity profiles of the secondary star on the hydrogen ZAMS (solid line), after the fast (dotted line) and the slow (short dashed line) phase of Case A mass transfer, after Case AB mass transfer (dash-dotted line), when helium ignites in the core (three dots-dashed line) and when the central helium abundance is 67% (long dashed-line).

conclude that this star has enough angular momentum to produce a collapsar and, in the case that the hydrogen envelope is lost during red supergiant phase, a gamma-ray burst.

The gain of angular momentum of an accreting star is proportional to the amount of accreted matter. We show in Fig.5.13 specific angular momentum profiles of the secondary (X_c=0, T_c=1.4·10^8K) assuming the accretion of 0.25, 1.4 and 5$M_\odot$ during Case AB mass transfer. We see that the specific angular momentum of the core is higher if the star accreted more matter during mass transfer. The specific angular momentum of the core at 3$M_\odot$ increases from 6·10^{16}cm^{2}s^{-1} to 8·10^{16}cm^{2}s^{-1}.
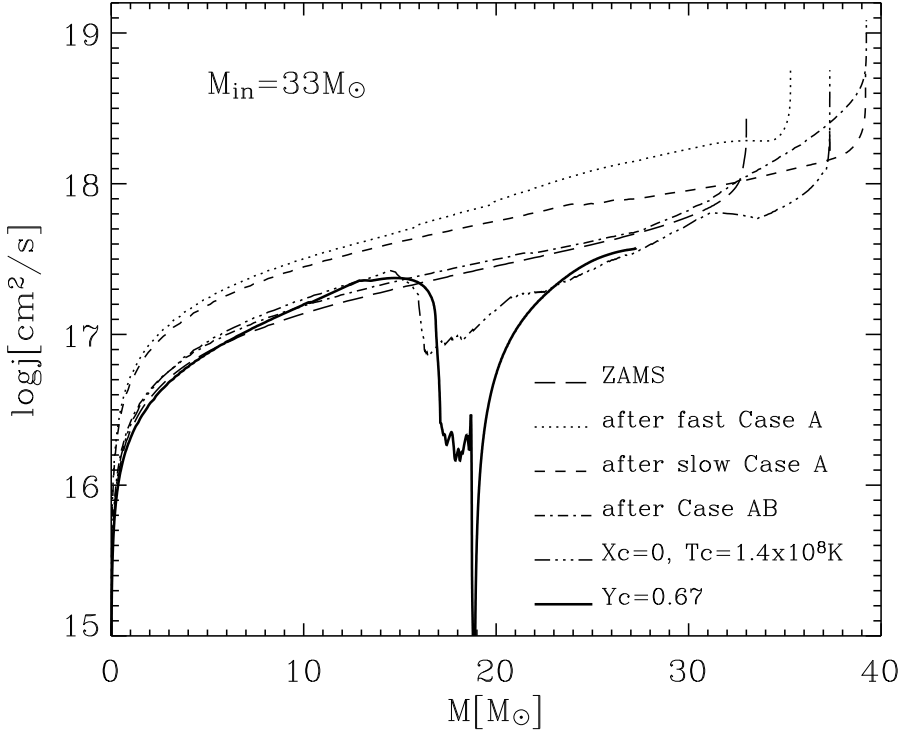
Figure 5.11: Specific angular momentum profiles of the secondary star on the hydrogen ZAMS (long dashed line), after fast (dotted line) and slow (short dashed line) Case A mass transfer, after Case AB mass transfer (dash-dotted line), when helium ignites in the core (three dots-dashed line) and when the central helium abundance is 67% (solid line).

5.4 Models with magnetic field

5.4.1 Single stars

We model the evolution of a single $42M_\odot$ star with an initial rotational surface velocity of 200 km s^{-1} and magnetic field included. Fig.5.14 shows specific angular momentum profiles in different phases of the evolution. We see that the initial (ZAMS) profiles of the star without magnetic field (Fig.5.3, dot-dashed line) and the star with magnetic field (Fig.5.14, dot-dashed line) are identical and represent solid body rotation. However, we can notice that the magnetic star loses more angular momentum from the core during the main sequence evolution as well as between hydrogen core exhaustion (Fig.5.14, dashed line) and core helium ignition (Fig.5.14, solid line).
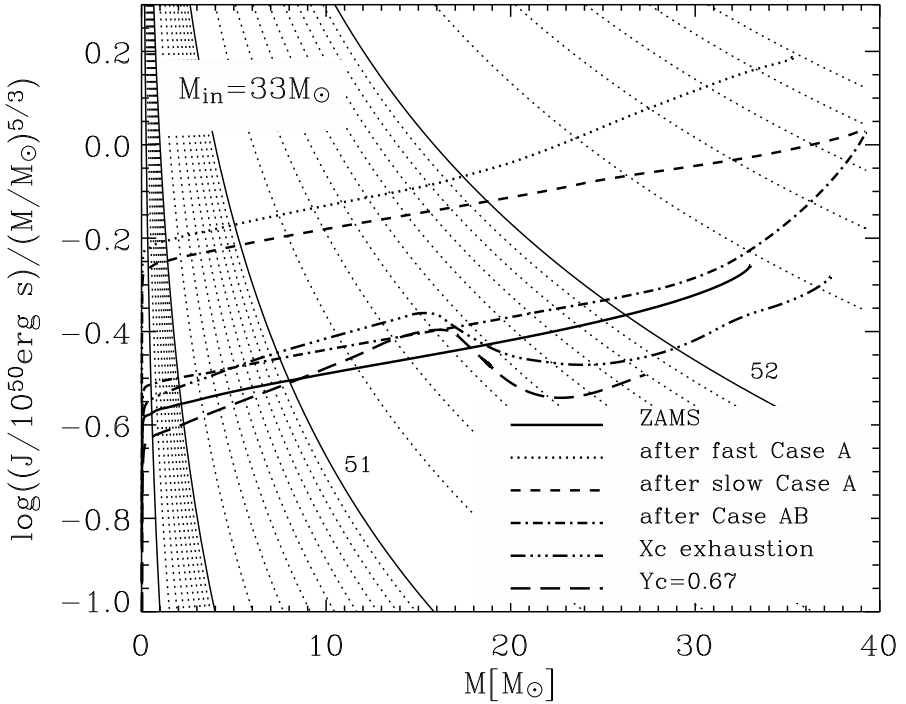
Figure 5.12: Logarithm of the integrated angular momentum $J(m)=\int_0^M j(m')dm'$ divided by $m^{5/3}$, as a function of the mass coordinate m for a $33M_\odot$ secondary star for the same evolutionary stages as shown in Fig.5.11. The thin lines give a logarithmic scale of levels of constant J labelled with $\log(J/(\mathrm{erg\ s}))$.

The star loses mass by a stellar wind. This removes angular momentum from the surface layers and slows them down. However, since the magnetic torque keeps the star close to solid body rotation during the main sequence evolution (Fig.5.15), angular momentum is being transported from the stellar interior towards the surface. The viscosity due to the magnetic field is a few orders of magnitude larger than the one for rotational mixing ($\sim 10^{10-12}\mathrm{cm}^2\mathrm{s}^{-1}$ compared with $\sim 10^{7-8}\mathrm{cm}^2\mathrm{s}^{-1}$), and it can overcome the μ-gradient barrier. Due to this, the surface of the star is being spun up and the core is being slowed down. Also, the surface layers are rotating faster than in the corresponding non-magnetic star, and the stellar wind mass loss is higher (Fig.5.16).

So, the core of a magnetic star loses significantly more angular momentum during the main sequence evolution than when magnetic fields are not included. One reason is that the μ-gradient does not represent a strong barrier for angular momentum transport. And second, because the surface layers are spun-up, the stellar wind
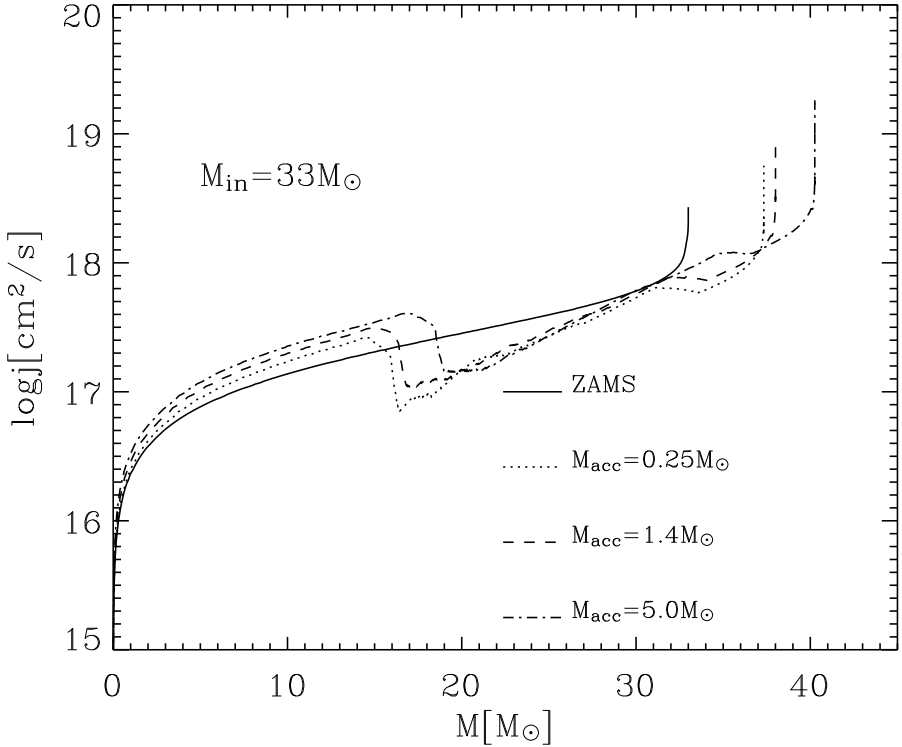
Figure 5.13: Specific angular momentum profiles of the secondary star on the hydrogen ZAMS (solid line) and when helium ignites in the core (T_c=1.4·10^8K), assuming the accretion of 0.25$M_\odot$ (dotted line) 1.4$M_\odot$ (dashed line) or 5$M_\odot$ (dot-dashed line) during Case AB mass transfer.

mass loss is larger and this requires more angular momentum from the core to keep solid body rotation of the star. Due to all this when hydrogen burning is finished (T_c=0.8·10^8K), the specific angular momentum of the core (at 3$M_\odot$) is less than 3·10^{16}cm^{2}s^{-1} (Fig.5.14, dashed line).

When the star starts expanding after core hydrogen burning is finished, magnetic torques still try to preserve solid body rotation. However, the envelope expansion is too fast and angular momentum transport is not efficient enough to keep it synchronized with the core (Fig.5.15), but since magnetic viscosity can overcome the μ-gradient, the core is slowed down and the envelope is spun up. Stellar wind mass loss is enhanced due to faster rotation and is significantly higher than in the case of the non-magnetic star (Fig.5.16). Due to all this the star loses significant amount of angular momentum between hydrogen exhaustion and helium ignition and the specific angular momentum of the core (at 3$M_\odot$) when helium core burning starts is
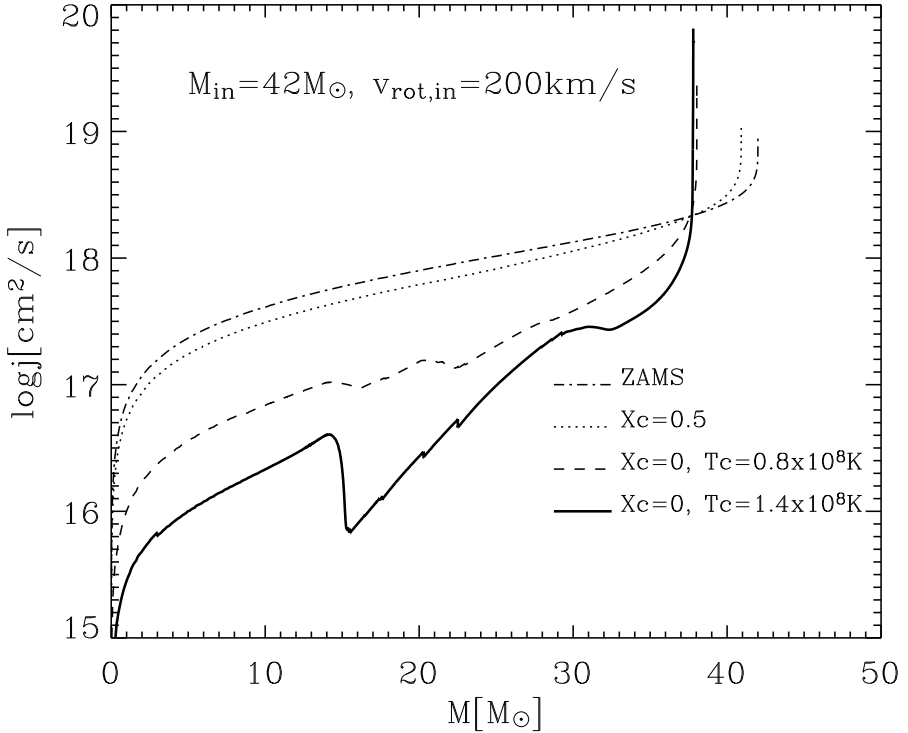
Figure 5.14: Specific angular momentum profiles of the $42M_\odot$ single star with magnetic fields on the hydrogen ZAMS (dot-dashed line), when there is 50% of hydrogen left in the center (dotted line), when hydrogen is exhausted in the core (dashed line) and when central helium burning starts (solid line).

only $5 \cdot 10^{15} \mathrm{cm}^2 \mathrm{s}^{-1}$.

5.4.2   Binary systems

We modelled the evolution of a rotating binary system with magnetic field, initial masses $M_{1,in}=56M_\odot$ and $M_{2,in}=33M_\odot$ and an initial orbital period of $p_{in}=6$ days. The binary system starts synchronized on the ZAMS with initial surface rotational velocities of $\sim$90 km s^{-1} for the primary and $\sim$60 km s^{-1} for the secondary which is, as we already mentioned for non-magnetic models, much slower than the typical values for single stars of these masses.

During the fast phase of Case A mass transfer ($\dot{M}_{tr} \sim 10^{-3} M_\odot \mathrm{yr}^{-1}$), the primary loses $\sim$20M$_\odot$ and the secondary accretes only about 4.5M$_\odot$ of that matter due to the mass loss caused by rotation close to break-up. After the fast process of Case A mass
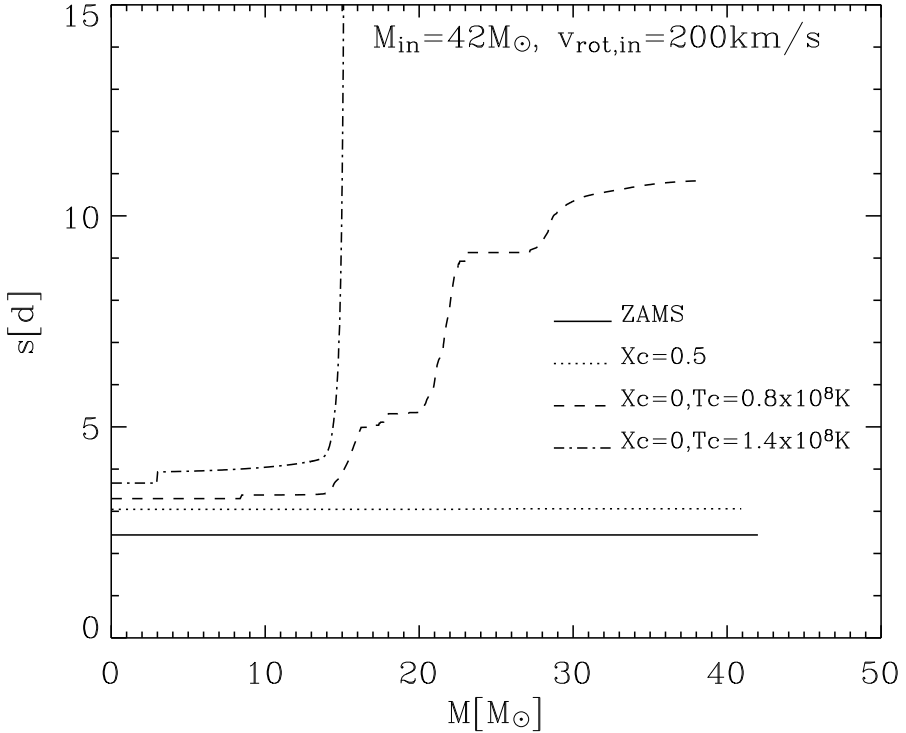
Figure 5.15: Spin period profiles of the $42M_\odot$ single star on the ZAMS (solid line), when there is 50% hydrogen left in the center (dotted line), when hydrogen is exhausted in the core (dashed line), and when central helium burning starts (dot-dashed line).

transfer, the primary continues expanding on a nuclear time scale and transferring mass onto the secondary star, but with much lower mass transfer rates (slow Case A, $\dot{M}_{tr} \sim 10^{-6} M_\odot yr^{-1}$). At the end of core hydrogen burning the primary contracts and thus RLOF stops.

Accretion increases rotational velocity of the surface of the secondary star to almost 400 km s^{-1} during the fast phase of Case A mass transfer. The mass transfer rate during slow Case A mass transfer is significantly lower ($10^{-6} M_\odot yr^{-1}$), and the surface rotational velocity of the secondary increases to about 200 km s^{-1}.

Fig.5.20 shows specific angular momentum profiles of the secondary in different phases of evolution. The specific angular momentum of the secondary increases significantly due to the fast Case A mass transfer (Fig.5.20, dotted line). Angular momentum is transported more efficiently through the stellar interior compared to the non-magnetic model, since the diffusion coefficient due to magnetic field instabilities
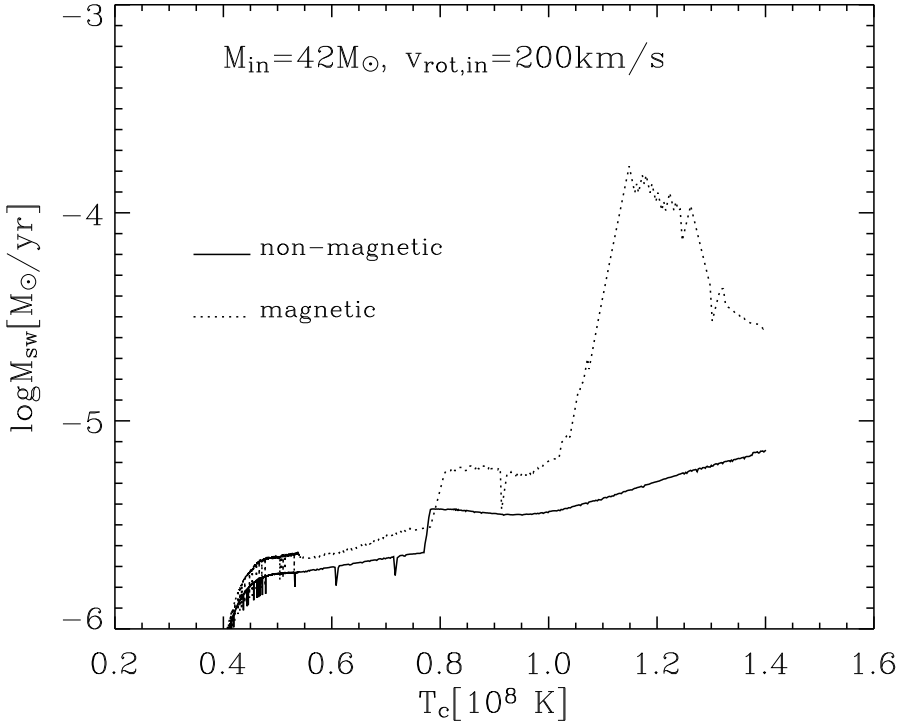
Figure 5.16: Stellar wind mass loss of the magnetic (dotted line) and non-magnetic (solid line) $42M_\odot$ star. The star with magnetic fields loses more mass due to the fact that magnetic torque tries to keep star in solid body rotation, which spins-up the surface layers and enhances mass loss.

is few orders of magnitude larger than the diffusion coefficient due to rotational instabilities (Fig.5.17). When we compare the specific angular momentum of the non-magnetic (Fig.5.11) and magnetic model (Fig.5.20), we notice that during fast Case A the angular momentum of the magnetic star increases more than that of the corresponding non-magnetic star ($2 \cdot 10^{17} \mathrm{cm^2 s^{-1}}$ for magnetic and $1.25 \cdot 10^{17} \mathrm{cm^2 s^{-1}}$ for non-magnetic star, $\sim 10^4$yrs after fast Case A, at $3M_\odot$).

The accretion stops when the secondary still has almost 50% of the hydrogen to burn in the core. Angular momentum is efficiently transported from the stellar core towards the surface and the μ-gradient can not stop it like in the case of the non-magnetic star. During further main sequence evolution, the stellar core loses significant angular momentum and when hydrogen core burning stops, the specific angular momentum at $3M_\odot$ is $2 \cdot 10^{16} \mathrm{cm^2 s^{-1}}$. Before helium ignites in the core, the specific angular momentum decreases to $6 \cdot 10^{15} \mathrm{cm^2 s^{-1}}$. The further evolution
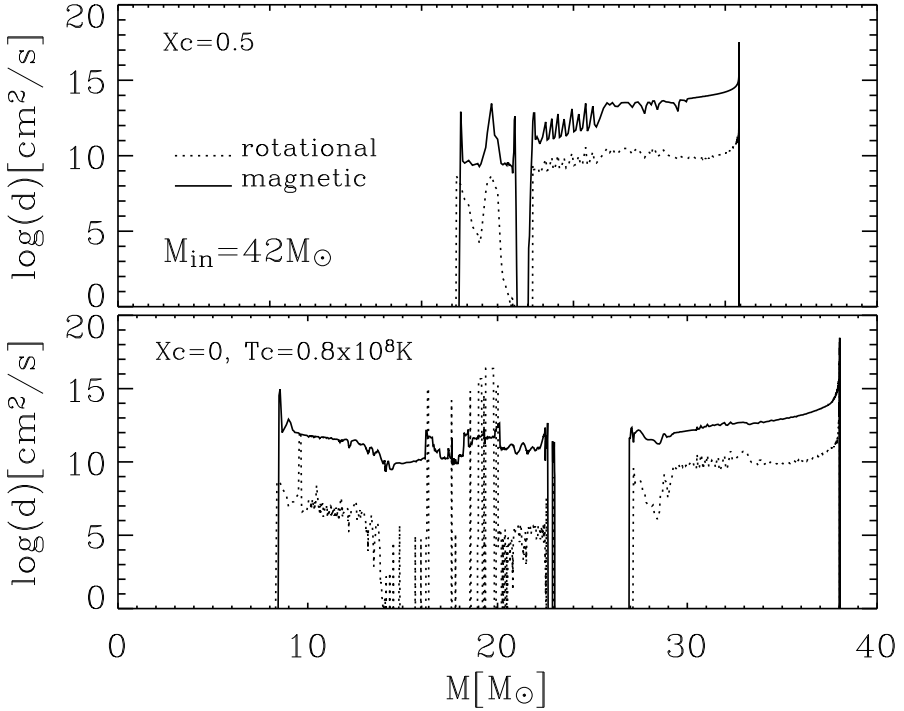
Figure 5.17: Diffusion coefficient due to magnetic field instabilities (solid line) and due to rotational instabilities (dotted line) for a rotating $42M_\odot$ star when central hydrogen abundance is 50% and when all hydrogen is exhausted in the core.

through the red supergiant phase slows down the core, since the envelope slows it down (magnetic viscosity can overcome the μ-barrier).

Apparently, if a star with magnetic fields accretes matter half way in the main sequence evolution, it has enough time to lose angular momentum before hydrogen is exhausted in the core. This is why we compute models of non-magnetic and magnetic $33M_\odot$ stars that accrete $2M_\odot$ at the end of their main sequence evolution (Y_c=0.95). The initial surface velocity of these stars is $\sim$60 km s^{-1}, since we assume that they evolve in a binary system.

When the central helium abundance reaches 95%, the core of the $33M_\odot$ star with magnetic fields has a specific angular momentum of about $2 \cdot 10^{16}$cm^{2}s^{-1} (Fig.5.24, dotted line). On the other side the core of a star without magnetic fields hardly lose any angular momentum and its specific angular momentum is $4 \cdot 10^{16}$cm^{2}s^{-1} (Fig.5.23, dotted line). After this, both stars accrete $2M_\odot$ of matter with an accretion rate of $10^{-4}M_\odot$yr^{-1}. We assume that in this case stellar wind mass loss is not en-
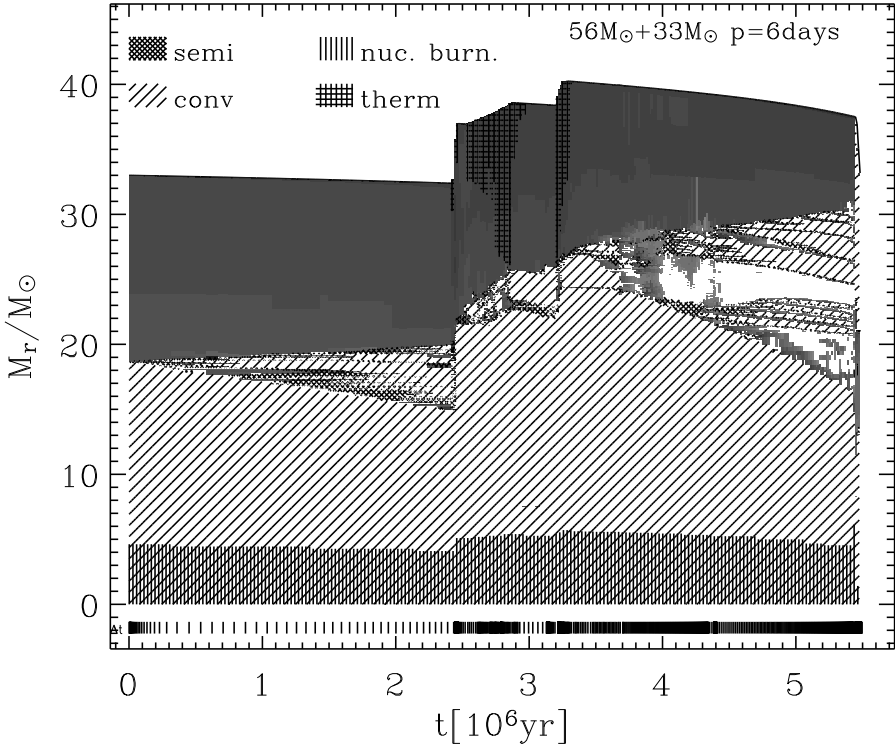
Figure 5.18: Evolution of the internal structure of a rotating $33M_\odot$ secondary star with magnetic field from the ZAMS until red supergiant phase Y_c=0.92. Convection is indicated with diagonal hatching, semiconvection with crossed hatching and thermohaline mixing with straight crossed hatching. The hatched area at the bottom indicates nuclear burning. Grey shaded areas represent regions with rotationally induced mixing (intensity is indicated with different shades, the darker the colour, the stronger rotational mixing). The topmost solid line corresponds to the surface of the star.

hanced by rotation, so there is no angular momentum loss due to this effect. Accreted matter adds angular momentum to the surface layers and this angular momentum is then transported through the stellar interior much more efficiently in the model with magnetic field. At the end of accretion (Fig.5.23 and Fig.5.24, dashed line), angular momentum has been transported further inward in the magnetic star, than in the non-magnetic. If we look at the specific angular momentum profiles 10^4yrs after the accretion ended, we can notice that the specific angular momentum of the core of the magnetic star increased to almost $3 \cdot 10^{16}$cm^{2}s^{-1} (at $3M_\odot$). On the other side, angular momentum of the non-magnetic star has been transported inward, but has still not reached the core.
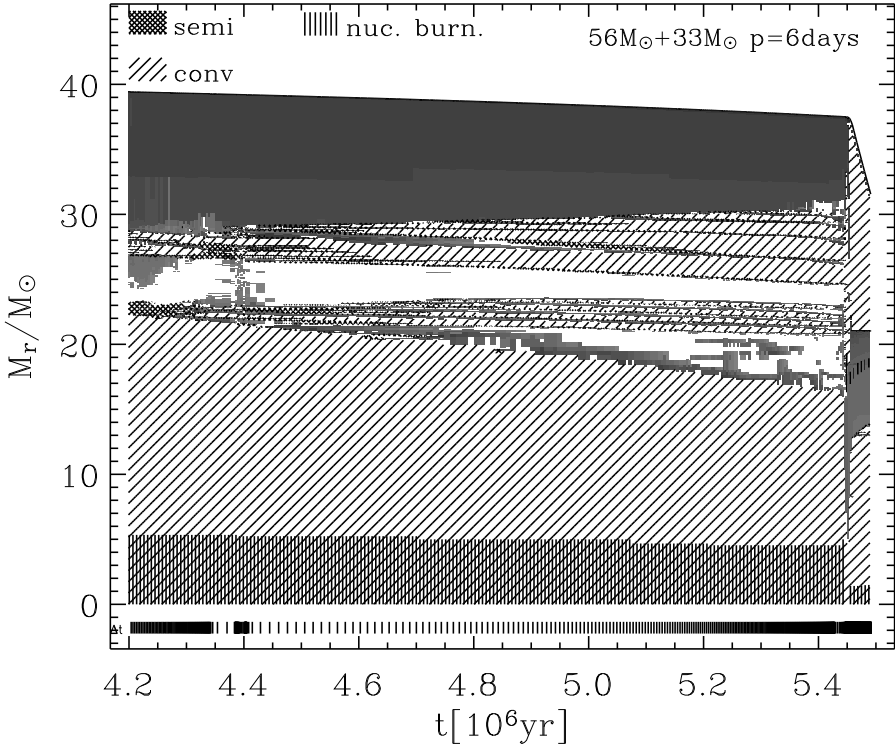
Figure 5.19: Evolution of the internal structure of a rotating $33\mathrm{M}_\odot$ secondary star with magnetic field from after the SN explosion of the primary and disruption of the system. Convection is indicated with diagonal hatching, semiconvection with crossed hatching and thermohaline mixing with straight crossed hatching. The hatched area at the bottom indicates nuclear burning. Grey shaded areas represent regions with rotationally induced mixing (intensity is indicated with different shades, the darker the colour, the stronger rotational mixing). The topmost solid line corresponds to the surface of the star.

The magnetic star continues losing angular momentum from the core during the further main sequence evolution ($\sim 10^5$yrs), and when hydrogen is exhausted in the core the specific angular momentum at $3\mathrm{M}_\odot$ is $1.6\cdot10^{16}\mathrm{cm}^2\mathrm{s}^{-1}$. Also, in the magnetic model, as we already explained, the core loses significant amounts of angular momentum between core hydrogen exhaustion and core helium ignition, and when central helium burning starts, the specific angular momentum of the core at $3\mathrm{M}_\odot$ is only $6\cdot10^{15}\mathrm{cm}^2\mathrm{s}^{-1}$.
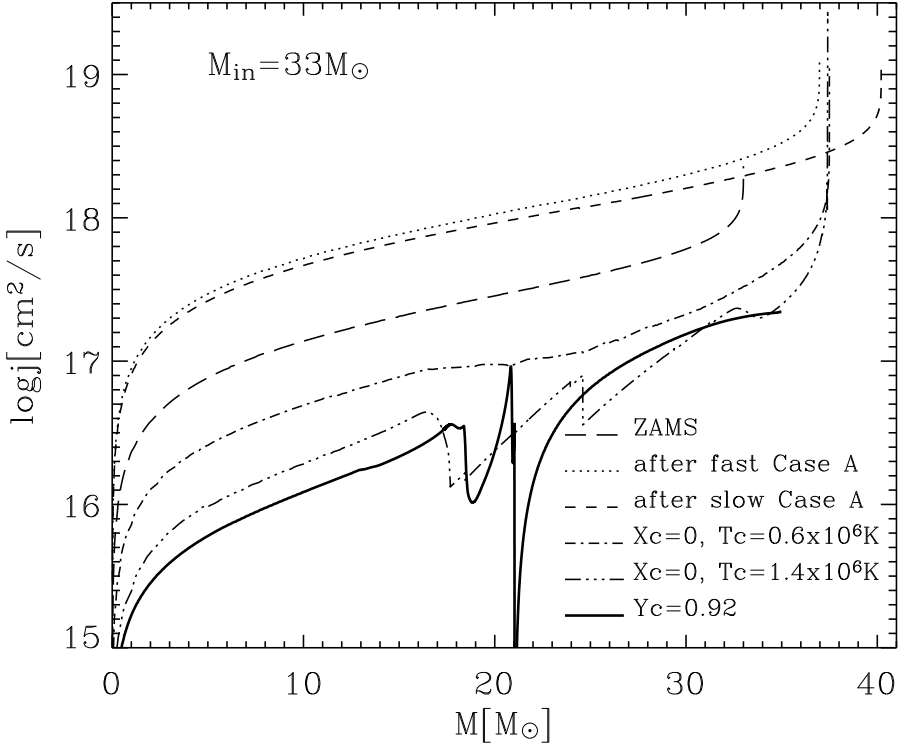
Figure 5.20: Specific angular momentum profiles of the secondary star with magnetic fields on the hydrogen ZAMS (long dashed line), after fast (dotted line) and slow (short dashed line) Case A mass transfer, when all hydrogen is exhausted in the center (dot-dashed line), when helium ignites (three dots-dashed line) and and when the central helium abundance is 92% (solid line).

5.5 Conclusions

The single star models presented above confirm that non-magnetic stars in the mass range relevant for GRB production through collapsars may retain enough core angular momentum for a GRB to form. In particular those stars which evolve into red supergiants and transform into Wolf-Rayet stars only towards the end of core helium burning can avoid a significant core angular momentum loss through Wolf-Rayet winds and may retain a specific angular momentum of up to $10^{17} \mathrm{cm}^2\mathrm{s}^{-1}$ in their iron cores. In these models, an effective core angular momentum loss during the main sequence is prevented by the suppression of rotational mixing in regions containing a mean molecular weight gradient. Angular momentum loss from the stellar core during helium burning is insignificant. Contrary to the trend found in Heger
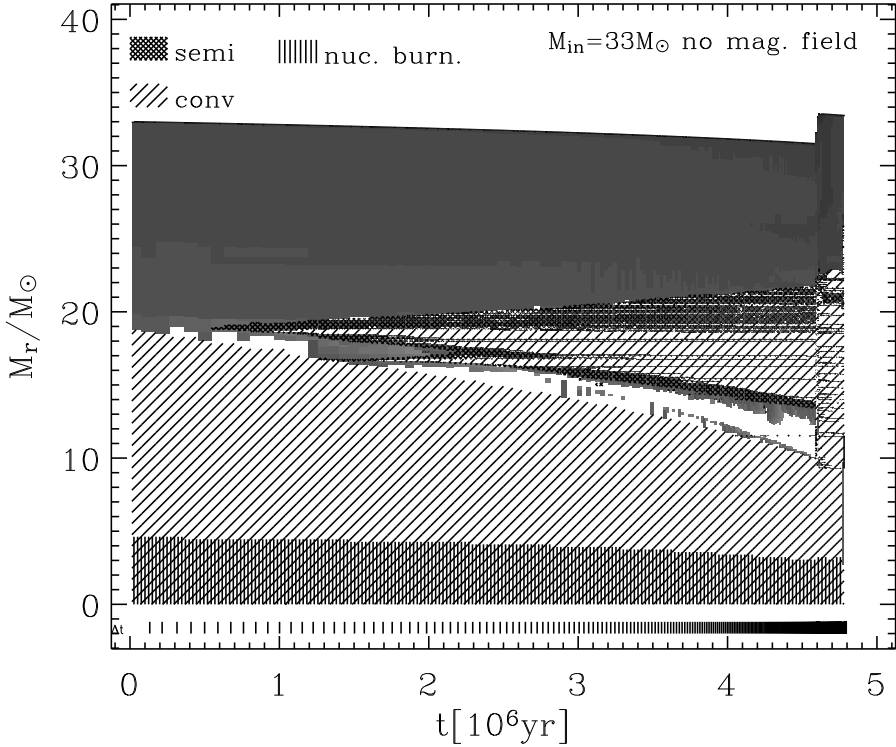
Figure 5.21: Evolution of the internal structure of a rotating $33M_\odot$ secondary star until helium ignition in the core. The star accretes $2M_\odot$ when the central helium abundance is 95%. Convection is indicated with diagonal hatching, semiconvection with crossed hatching and thermohaline mixing with straight crossed hatching. The hatched area at the bottom indicates nuclear burning. Gray shaded areas represent regions with rotationally induced mixing (intensity is indicated with different shades, the darker the colour, the stronger rotational mixing). The topmost solid line corresponds to the surface of the star.

et al. (2000a), we find that a $42M_\odot$ star may end its life with a larger specific core angular momentum than a $20M_\odot$. The reason is that, for the same initial equatorial rotation velocity, the initial specific angular momentum in the $42M_\odot$ is significantly larger due to its larger initial radius. We note that a similar trend has been found by Hirschi et al. (2004).

The magnetic field model of Spruit (2002) allows a significant angular momentum transport even in the presence of mean molecular weight gradients. Heger et al. (2004) already found the increased coupling of core and envelope to result in iron core specific angular momenta of the order of $10^{14} \text{cm}^2 \text{s}^{-1}$ for stars between 10 and $25M_\odot$. Our magnetic $42M_\odot$ single star model was only computed up to core helium
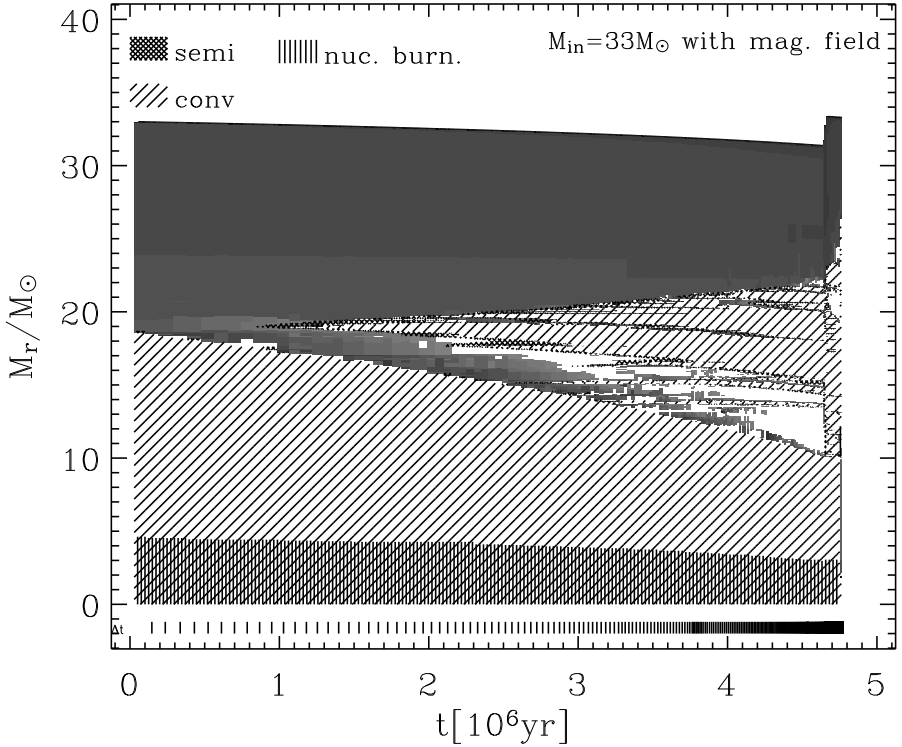
Figure 5.22: Evolution of the internal structure of a rotating $33M_\odot$ secondary star with magnetic field until helium ignition in the core. The star accretes $2M_\odot$ when the central helium abundance is 95%. Convection is indicated with diagonal hatching, semiconvection with crossed hatching and thermohaline mixing with straight crossed hatching. The hatched area at the bottom indicates nuclear burning. Gray shaded areas represent regions with rotationally induced mixing (intensity is indicated with different shades, the darker the colour, the stronger rotational mixing). The topmost solid line corresponds to the surface of the star.

ignition. However, by then the specific core angular momentum was already reduced by a factor of 30 from the initial value. Heger et al. (2004) showed that during core helium burning the core-envelope coupling reduces the core angular momentum by another order of magnitude. The final specific core angular momentum in our $42M_\odot$ star can thus be estimated to fall below $\sim 10^{15} \mathrm{cm}^2 \mathrm{s}^{-1}$, which will render effects of rotation during the core collapse insignificant.

We also model the evolution of a $56M_\odot + 33M_\odot$ binary system with an initial orbital period of 6 days. Since the binary-enhanced mass loss of the primary leads to extremely slow rotation, our attention focuses on the secondary star, which is spun-up due to accretion of mass and angular momentum. We computed two binary
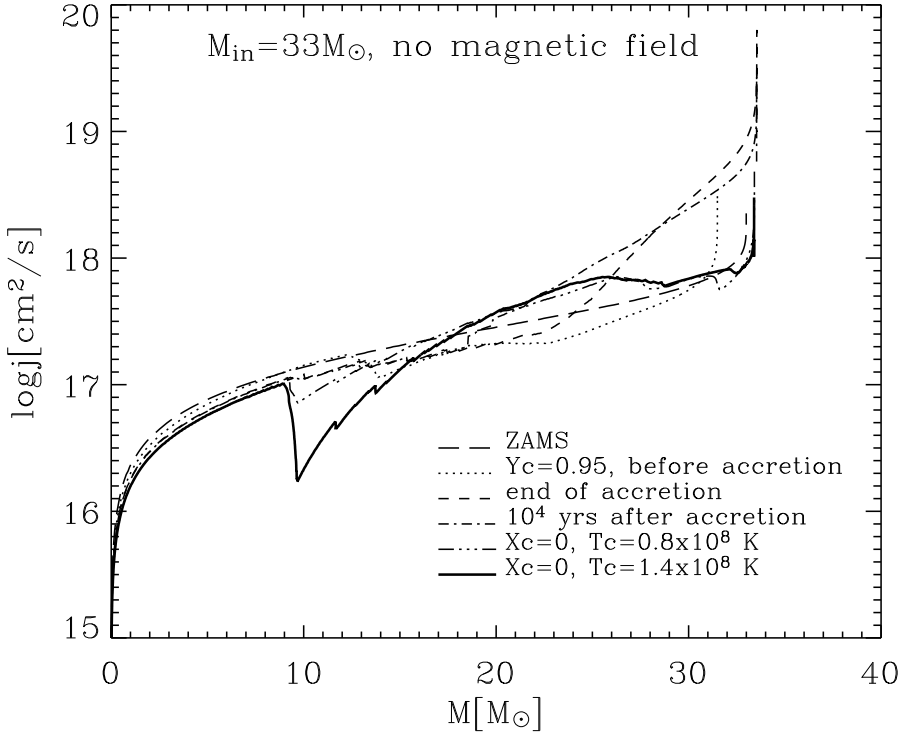
Figure 5.23: Specific angular momentum profiles of a $33M_\odot$ non-magnetic star on the ZAMS (long dashed line), when Y_c=95% (dotted line), at the end of the accretion (dashed line), 10^4yrs after the accretion (dot-dashed line), when hydrogen is exhausted in the core (three dot-dashed line) and when helium ignites in the core (solid line).

evolution sequences, with and without magnetic fields. In both sequences, the initial $33M_\odot$ star grows to about $40M_\odot$ due to accretion during is main sequence evolution, and subsequently evolves into a red supergiant. Before the mass transfer, tidal spin-orbit coupling leads to bound rotation of both stars, which leads to a specific angular momentum which is a factor of 3...5 smaller than in a corresponding single star.

The accretion leads to a significant spin-up of the star. In the non-magnetic model, the mean molecular weight gradients limit the inward flow of angular momentum, and the corresponding spin-up of the core merely compensates the tidally induced angular momentum loss. The result is a helium core which rotationally decouples from the envelope with roughly the same mass and angular momentum as in the case of a $42M_\odot$ single star, i.e. with high enough specific angular momentum to produce a GRB.
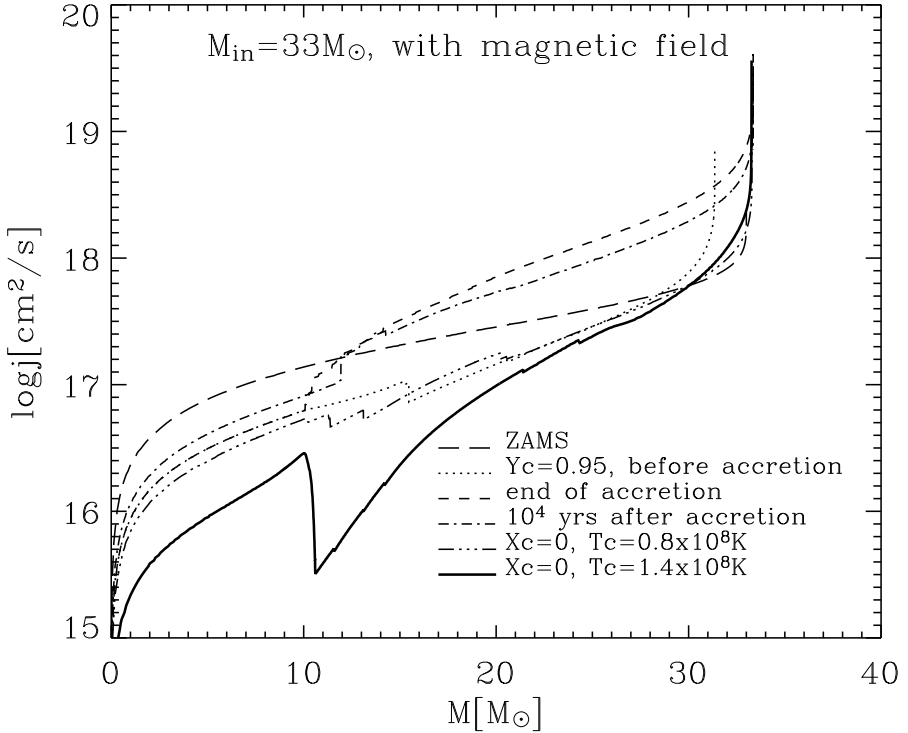
Figure 5.24: Specific angular momentum profiles of a $33M_\odot$ magnetic star on the ZAMS (long dashed line), when Y_c=95% (dotted line), at the end of the accretion (dashed line), 10^4 yrs after the accretion (dot-dashed line), when hydrogen is exhausted in the core (three dot-dashed line) and when helium ignites in the core (solid line).

In the magnetic model, the core spin-up due to accretion is stronger. It temporarily leads to a core spin rate which is factor of 2..3 above that of a ZAMS star of comparable mass. However, magnetic core-envelope coupling has reduced the specific core angular momentum by almost a factor of 100 by the time the star has stared core helium burning. Its final core angular momentum will thus be comparable to that of the magnetic $42M_\odot$ single star model discussed above: far too small to produce a GRB.

Clearly, the effect of core spin-up due to accretion on the final core angular momentum will be larger if the accretion occurs later in the evolution of the accreting star, as there will be less time to lose the thereby gained angular momentum again. Therefore, we performed the numerical experiment of accreting $2M_\odot$ of material on a $33M_\odot$ at a time when the core hydrogen concentration was down to 5% (in-

stead of about 40% in the binary evolution model). The result was again that the core-envelope coupling in the magnetic model was overwhelming and prevents this scenario to be a realistic option for GRB production.

We conclude that our binary models without magnetic field can reproduce stellar cores with a high enough specific angular momentum ($j \geq 3 \cdot 10^{16} \mathrm{cm}^2 \mathrm{s}^{-1}$) to produce a collapsar and a GRB.

However, if magnetic field is taken into consideration, GRBs at near solar metallicity need to be produced in rather exotic binary channels, or the magnetic effects are currently overestimated in our models. The first option is not implausible, since reverse mass transfer from the original secondary star onto the primary star during its Wolf-Rayet phase (Wellstein et al. 2001), or late stellar merger may lead to an efficient core spin-up. However, the realization frequency of such events, even though it is difficult to estimate, may be small. The latter would require a significant angular momentum loss of iron cores which form neutron stars, either during collapse and supernova explosion, or shortly thereafter, in order to explain the relatively slow rotation rates of young pulsars.

Chapter 6

Masivne zvezde u bliskim dvojnim sistemima

Kratak sadržaj na srpskom jeziku

Uvod Za zvezdu se kaže da je masivna, ako u toku svog života prodje kroz sve faze nuklearnih reakcija, dakle sagori vodonik, helijum, ugljenik, kiseonik itd i formira jezgro od gvoždja i nikla (početna masa zvezde veća od oko 10 Sunčevih masa). Na početku svog života, dok sagorevaju vodonik u jezgru, ovakve zvezde su klasifiko- vane kao zvezde tipa O ili B. Dalje u toku evolucije one prolaze kroz fazu Sjajna plava promenljiva zvezda (Luminous blue variables, LBVs), Crveni superdžin (Red supergiants, RSGs) i Wolf-Rayet zvezda (WR). Masivne zvezde na kraju svog života eksplodiraju kao Supernove, rasejavajući hemijske elemente koji su u njima nastali, dajući na taj način osnovu za nastanak života u kosmosu. U isto vreme, njihovo jezgro formira super-kompaktni objekat: neutronsku zvezdu ili crnu rupu.

Deo materijala zvezde koja brzo rotira u trenutku kad eksplodira kao supernova moze da oformi akrecioni disk oko novonastale crne rupe. Ovakva zvezda se naziva kolapsar. Akrecija materijala u crnu rupu dovodi do oslobadjanja velike količine en- ergije. Usled ovoga, zagrejani gas oko polova počinje da se širi u vidu relativističkog džeta (mlaza) koji ubrzava naelektrisane čestice i dolazi do emisije visoko energet- skih gama fotona. Ova pojava se naziva Gama bljesak (Gamma-ray burst).

Ako se zvezde, odredjene mase i hemijskog sastava, nalaze u bliskom dvojnom sistemu (dve zvezde koje se kreću oko zajedničkog centra mase) njihova evolucija je značajno drugačija nego ako su usamljene. Primarna komponenta (masivnija zvezda u sistemu) evoluira brže, njen radijus raste i kada dostigne radijus Roche površi, počinje transfer mase na drugu komponentu kroz prvu Lagranževu tačku. Roche površ je gravitaciona ekvipotencijalna površina oko svake zvezde. Materija koja se nalazi unutar Roche površi primarne komponente je pod uticajem gravitacije isključivo ove zvezde. Isto važi za sekundarnu, manje masivnu komponentu.

Ako se dve zvezde O tipa nalaze u bliskom dvojnom sistemu, masivnija kompo- nenta će početi transfer mase na sekundarnu komponentu nakon sto je njen radijus dostigao Roche radijus. Ovo se može desiti u različitim fazama evolucije primarne zvezde i na osnovu toga je načinjena klasifikacija različitih tipova transfera mase:
Tip A: do transfera mase dolazi dok primarna zvezda sagoreva vodonik u jezgru
Tip B: do transfera mase dolazi nakon sto je primarna komponenta zavrsila sagore- vanje vodonika u jezgru i počela sagorevanje vodonika u omotaču.
Tip C: do transfera mase dolazi nakon sto je primarna zvezda završila sagorevanje vodonika i helijuma u jezgru i počela sagorevanje helijuma u omotaču.

Kada će do transfera mase doći zavisi od početnog orbitalnog perioda (period u toku koga zvezde obidju jednom oko zajedničkog centra mase). Period raste sa povećanjem udaljenosti komponenata u dvojnom sistemu. Ako je početni orbitalni period veoma kratak, reda veličine nekoliko dana, radijus zvezde brzo dostigne Roche radijus i nastupa transfer mase Tipa A. Ako je početni orbitalni period reda veičine nekoliko nedelja doći će do transfera mase Tipa B, a za još duže periode do transfera mase Tipa C.

Dve zvezde koje započnu život kao bliski dvojni O sistem će evoluirati u dvojni sistem sa jednom Wolf-Rayet i jednom O zvezdom, tzv WR+O sistem, jer će primarna zvezda izgubiti vodonik u toku transfera mase na sekundarnu komponentu. Do sada je posmatrano oko četrdeset WR+O dvojnih sistema, ali je za samo dvadesetak odredjena masa obe komponente.

Rezultati ove teze   U drugom poglavlju ove teze je pokazano da povećana metaličnost u masivnim zvezdama sačinjenim isključivo od helijuma (WR zvezde bez vodonika) utiče na povećanje radijusa. Medjutim, ovaj efekat nestaje ako zvezdani vetar predje odredjenu kritičnu vrednost.

U poglavlju 3 se može videti da efikasnost akrecije materije u dvojnom sistemu može biti značajno smanjena usled brze rotacije sekundarne komponente. Pokazano je da odredjeni posmatrani WR+O sistemi mogu biti modelirani ako sekundarna zvezda zadrži samo 10% materije koja dolazi sa primarne komponente. S druge strane, u poglavlju 4 je pokazano da zvezdani vetar ne može efikasno da umanji akreciju materije na sekundarnu zvezdu.

U petom poglavlju je pokazano da masivne rotirajuće zvezde (oko 40 Sunčevih masa) imaju dovoljno veliki ugaoni momenat u trenutku kolapsa da formiraju akrecioni disk oko novonastale crne rupe i proizvedu gama bljesak. Medjutim, ako je magnetno polje uzeto u obzir, finalno jezgro zvezde rotira isuviše sporo i na ovaj način nije moguće proizvesti kolapsar.

Chapter 7

Over de evolutie van massieve dichte dubbelster systemen

een Nederlandse samenvatting

Introduction   Sterren beginnen hun leven door uit een dichte wolk van interstellar materie te condenseren. Aangezien de wolk onder zijn eigen zwaartekracht instort wordt de materie heter. Als de aanvankelijke massa groter is dan ongeveer 0,1 Zonnemassa's (verder $M_\odot$), zal de kerntemperatuur toenemen tot ongeveer 10^7K en zullen kernreacties beginnen, waarbij waterstof in helium word omgezet. Deze fase van elke ster zijn leven wordt hoofdreeks evolutie genoemd. Afhankelijk van de aanvankelijke massa, hebben de sterren verschillende eigenschappen tijdens hun hoofdreeks. De hoofdreeks-sterren zoals onze Zon zijn geel, matig warm met oppervlaktetemperatuur van ~6000 K en zij leven 10 miljarden jaren. Sterren minder dan de massief dan de Zon zijn koele, rode sterren en leven nog langer, terwijl de massievere sterren blauw en warm zijnen hun leven in slechts enkele miljoenen jaren kunnen beindigen. Afhankelijk van hun temperatuur en helderheid, zijn de sterren op de hoofdreeks geclassificeerd in spectrale klassen: O, B, A, F, G, K en M. De O-sterren zijn de meest massieve, blauwe en hete sterren (oppervlaktetemperatuur >25000 K) en de M-sterren zijn de minst massieve, koude (oppervlaktetemperatuur <3500 K) en rode sterren.

Nadat de kern waterstof opgebrand is, begint de ster aan te krimpen aangezien er geen kracht is om de zwaartekracht in evenwicht te houden. Hierdoor stijgt de temperatuur in de buitenlagen genoeg om waterstof aan te steken en de stellaire envelop begint zich uit te breiden. Aan de andere kant, krimpt de stellaire kern verder en wanneer de temperatuur ~10^8K, bereikt begint de kernhelium met branden. Deze fase van stellaire evolutie wordt rode reus (voor minder massieve sterren) of rode superreus (voor massievere sterren) fase genoemd.

Afhankelijk van hun initiele massa, zullen de sterren hun leven op verschillende manieren beindigen. De sterren met lage initiele massa's (minder dan 8 $M_\odot$) kunenn niet hoge genoege temperaturen in de kern bereiken om koolstof aan te steken, zodat hun kern na het helium branden krimpt tot een kleine compacte ster, genaamd een witte dwerg, terwijl de buitenlagen als planetarische nebula worden verspreid.

De meer massievere sterren ondergaan alle kernfusie stadia tot de vorming van ijzer-nikkel kern. Zij kunnen door de fase van ster wolf-Rayet (verder WR) evolueren. WR sterren hebben een uiterst heet oppervlakte ($50000K$), zeer hoge helderheid (L ~10^5-10^6 zonnehelderheid, verdere $L_\odot$), hoge massaverlies ($\dot{M}$~$10^{4-5}m_\odot yr^{-1}$) en hebben het grootste deel van hun waterstof rijke envelop verloren. Nadat alle helium in de kern opgebrand is, fuseren de koolstof en de zuurstof. Hun fusie levert producten op zoals neon, magnesium, silicium, en zwavel. Uiteindelijk, fuseren het silicium en de zwavel in de sterkern om een ijzer-nikkel kern te vormen. Terwijl de fusie van elementena lichter dan ijzer energie vrijgeeft, verbruikt de ijzerfusie energie. Er is geen kracht meer om de zwaartekracht in evenwicht te brengen en de stellaire kern stort in. Afhankelijk van de massa van een kern, stort het in tot een neutronenster (kernmassa's kleiner dan 2,5 $M_\odot$) of een zwart gat. Tezelfdertijd worden de massalagen buiten de kern uitgeworpen door een supernova(sn) explosie.

Aangezien kernfusiereacties die elementen dan ijzer zwaarder maken meer energie vereisen dan zij opleveren, komen dergelijke reacties niet in stellaire kernen, maar slechts in supernova's explosies voor. Naast het maken van elementen, verspreiden de supernova's de elementen (die door zowel de ster als supernova werden gemaakt) door interstellaire medium. Dit zijn de elementen waaruit sterren, planeten en alles ter wereld worden gemaakt– met inbegrip van ons.

Supernova Explosies massieve snel roterende sterren zouden aan de gebeurtenissen van de gammaflitsen kunnen worden verbonden. Gammaflitsen (GRBs) zijn flitsen van gamma-fotonen (energie $E >10^5$eV), die over de gehele hemel verscheidene keren per dag op zeer grote afstanden van Aarde verschijnen. Gammaflitsen geven bij hun oorsprong uiterst grote hoeveelheid energie, (ongeveer 10^{52}-10^{54}erg) vrij. Dit is de hoeveelheid energie die door 1000 sterren zoals Zon over hun volledig leven wordt vrijgegeven.

De evolutie van een ster in een binair systeem kan beduidend verschillen van n enkele gesoleerde met de zelfde massa en de chemische samenstelling . De fysieke processen die belangrijk zijn voor binaire evolutie zijn de gewijzigde gravitatie en stralingsgebied van de metgezel ster, evenals middelpuntvliedende kracht bijdrage die het gevolg is van de omwenteling van het systeem. Maar het belangrijkst is het de evolutie van de massievere component die dramatisch de evolutie van het systeem zal benvloeden. In bepaalde evolutieve fasen kan het namelijk voorkomen, dat massaoverdracht van n ster (de primaire, massadonor) aan de andere (secundaire, massaaccretor) plaatsvind , waardoor eigenschappen zoals de helderheid, de straal, de efficinte temperatuur, de overvloed enz. van beide sterren, evenals hun toekomstige evolutie veranderd worden. Het binaire systeem dat aanvankelijk uit twee massieve sterren van het O-type besgint uiteindelijk met massaoverdracht. Tijdens dit proces zal de massa donor een significante hoeveelheid waterstof van zijn envelop verliezen en dit systeem zal in een WR+O binair systeem evolueren. Verder komen meer astrofysische fenomenen voor wegens de details van binaire evolutie, met betrekking tot massaoverdracht voor (X-ray binaire systemen, supernova's Ib en Ic, γ flitsen).

Dit proefschrift De motivatie voor deze thesis is om de kennis over de evolutie van massieve sterren te verbeteren, in binaire evenals enkelvoudige systemen. In Hoofdstuk 2, onderzoeken wij de diameter van massieve, chemisch homogene modellen van een heliumster, die reeds zijn aangetoond om evolutieve modellen van waterstof-vrije WR sterren zeer nauwkeurig te vertegenwoordigen. De stralen van waterstof-vrije WN sterren in de massa varierend van 10... 30 $M_\odot$ gewoonlijk worden gevonden in de orde van 1... 2 $R_\odot$. Wij vinden dat hellum sterren met een metaalgehalte gelijk aan de Zon boven $\sim 15 M_\odot$ een uitgebreide envelopstructuur ontwikkelen als het massaverlies wordt genegeerd. Nochtans toonden wij aan dat zelfs in massieve, metaal-rijke sterren, de inflatie van de envelop wordt vermeden als de stellaire windmassa verlies een bepaalde kritieke waarde overschrijdt. Observa-

tionele afgeleide waardes van het massaverlies van WR sterren zijn bij of boven deze kritieke waarde.

In hoofdstuk 3 tonen we dat de snelheid van de massa accretie beduidend kan worden verminderd wegens omwenteling van de secundaire ster dicht bij de kritieke waarde. Wij onderzoeken de mogelijkheid dat de voorloper evolutie van WR+O systemen (HD186943, HD90657 en HD211853) was door de massaoverdracht van het Geval A met $\beta \approx 0.1$. Voor niet roterende modellen veronderstellen wij $\beta = 0.1$ die wordt gebaseerd op de schatting van de vereenvoudigde benadering. Voor roterende modellen vermindert de accretie iefficiency wanneer de secundaire ster dicht bij kritieke omwenteling roteerd. Het primaire massa bereik voor het niet-roterende modellen is 41..75$M_\odot$ en voor roterende modellen 41..65$M_\odot$. In Hoofdstuk 4 onderzoeken wij de mogelijkheid dat de stralingsdruk van de secundair ster de accretie verhindert. Wij vinden dat zelfs voor een gematigd waarde van de massaoverdracht ($5\cdot10^{-6}M_\odot\mathrm{yr}^{-1}$) de wind en de stralingsimpulsen niet de dynamica van de accretiestroom veranderen.

In hoofdstuk 5 tonen wij aan dat de enkelvoudige en dubbelsterren met massa $\sim 40M_\odot$ genoeg specifiek impulsmoment in de kern op het ogenblik van instorting hebben dat zij collapsars kunnen veroorzaken. Een collapsar is een massieve ($M_{>\mathrm{in}} \sim$35-40$M_\odot$) roterende ster waarvan de kern instort om een zwart gat te vormen. Als deze ster een groot impulsmoment op de evenaar heeft, zal een accretieschijf rond het zwarte gat worden gevormd. De accretie van de rest van de ster met hoge accretiewaardes in het pas gevormde zwarte gat geeft grote hoeveelheden energie vrij waarvan een deel in de as van de lage dichtheidsomwenteling van de ster wordt gedeponeerd. Het verwarmde gas bij de polen breidt zich in een hoogst relativistische straal uit die door de ster een tunnel graaft. Deze straal, en de drukgolf die het begeleidt, kunnen gammaflitsen veroorzaken die met een supernova van het Type Ib/c vergezeld gaat. Tijdens het proces van de massaoverdracht in een binair systeem, krijgt de oppervlakte van de accreterende ster extra impulsmoment. Dit impulsmoment wordt verder vervoerd door de stellaire binnenste en de stellaire kern, die snel genoeg begint te roteren om een accretieschijf na de instorting te vormen. Nochtans, als het magnetische veld in overweging wordt genomen, probeert de magnetische torsie om de vaste lichaamsomwenteling van de ster te handhaven en de stellaire kern vertraagt beduidend tijdens de evolutie.

Bibliography

Blondin, J. M., Richards, M. T., & Malinowski, M. L. 1995, ApJ, 445, 939

Bohannan, B. & Conti, P. S. 1976, ApJ, 204, 797

Boroson, B., Kallman, T., Blondin, J. M., & Owen, M. P. 2001, ApJ, 550, 919

Braun, A. 1998, Ph.D. Thesis

Braun, H. & Langer, N. 1995, A&A, 297, 483

Brookshaw, L. & Tavani, M. 1993, ApJ, 410, 719

Brown, G. E., Heger, A., Langer, N., et al. 2001, New Astronomy, 6, 457

Brown, G. E., Lee, C.-H., Wijers, R. A. M. J., et al. 2000, New Astronomy, 5, 191

Castor, J. I., Abbott, D. C., & Klein, R. I. 1975, ApJ, 195, 157

Chevalier, C. & Ilovaisky, S. A. 1998, A&A, 330, 201

Chiosi, C. & Maeder, A. 1986, ARA&A, 24, 329

Clark, J. S., Goodwin, S. P., Crowther, P. A., et al. 2002, A&A, 392, 909

Crowther, P. A., Dessart, L., Hillier, D. J., Abbott, J. B., & Fullerton, A. W. 2002, A&A, 392, 653

de Greve, J. P. & de Loore, C. 1992, A&AS, 96, 653

de Kool, M. 1990, ApJ, 358, 189

de Loore, C. & de Greve, J. P. 1992, A&AS, 94, 453

de Loore, C. & Vanbeveren, D. 1994, A&AS, 103, 67

Demers, H., Moffat, A. F. J., Marchenko, S. V., Gayley, K. G., & Morel, T. 2002, ApJ, 577, 409

Dessart, L., Langer, N., & Petrovic, J. 2003, A&A, 404, 991

Doom, C. & de Greve, J. P. 1983, A&A, 120, 97

Eggleton, P. P. 1971, MNRAS, 151, 351

—. 1972, MNRAS, 156, 361

—. 1983, ApJ, 268, 368

Friend, D. B. & Castor, J. I. 1982, ApJ, 261, 293

Fryer, C. L. 1999, ApJ, 522, 413

Fryer, C. L., Woosley, S. E., & Hartmann, D. H. 1999, ApJ, 526, 152

Gayley, K. G., Owocki, S. P., & Cranmer, S. R. 1997, ApJ, 475, 786

Glatzel, W. & Kiriakidis, M. 1993, MNRAS, 262, 85

Glatzel, W., Kiriakidis, M., & Fricke, K. J. 1993, MNRAS, 262, L7

Gräfener, G., Koesterke, L., & Hamann, W.-R. 2002, A&A, 387, 244

Hamann, W.-R. & Koesterke, L. 1998, A&A, 335, 1003

Hamann, W.-R., Koesterke, L., & Wessolowski, U. 1995, A&A, 299, 151

Heger, A., Fryer, C. L., Woosley, S. E., Langer, N., & Hartmann, D. H. 2003a, ApJ, 591, 288

Heger, A. & Langer, N. 1996, A&A, 315, 421

—. 2000, ApJ, 544, 1016

Heger, A., Langer, N., & Woosley, S. E. 2000a, ApJ, 528, 368

Heger, A., Woosley, S. E., & Langer, N. 2000b, New Astronomy Review, 44, 297

Heger, A., Woosley, S. E., & Langer, N. 2003b, in IAU Symposium, 357–+

Heger, A., Woosley, S. E., Langer, N., & Spruit, H. C. 2004, in IAU Symposium 215, in press

Hirschi, R., Maeder, A., & Meynet, G. 2004, A&A, in prep.

Hjorth, J., Sollerman, J., Møller, P., et al. 2003, Nature, 423, 847

Huang, R. Q. & Taam, R. E. 1990, A&A, 236, 107

Iglesias, C. A. & Rogers, F. J. 1996, ApJ, 464, 943

Ishii, M., Ueno, M., & Kato, M. 1999, PASJ, 51, 417

King, A. R., Schenker, K., Kolb, U., & Davies, M. B. 2001, MNRAS, 321, 327

Kippenhahn, R. 1969, A&A, 3, 83

Kippenhahn, R., Kohl, K., & Weigert, A. 1967, Zeitschrift fur Astrophysics, 66, 58

Kippenhahn, R. & Thomas, H.-C. 1970, in IAU Colloq. 4: Stellar Rotation, 20–+

Kondo, Y. 1974, Ap&SS, 27, 293

Kopal, Z., ed. 1978, Dynamics of Close Binary Systems

Kudritzki, R. P., Pauldrach, A., Puls, J., & Abbott, D. C. 1989, A&A, 219, 205

Lamontagne, R., Moffat, A. F. J., Drissen, L., Robert, C., & Matthews, J. M. 1996, AJ, 112, 2227

Langer, N. 1989, A&A, 210, 93

—. 1991, A&A, 252, 669

Langer, N. 1997, in ASP Conf. Ser. 120: Luminous Blue Variables: Massive Stars in Transition, 83–+

—. 1998, A&A, 329, 551

Langer, N., Deutschmann, A., Wellstein, S., & Höflich, P. 2000, A&A, 362, 1046

Langer, N., Kiriakidis, M., El Eid, M. F., Fricke, K. J., & Weiss, A. 1988, A&A, 192, 177

Langer, N., Wellstein, S., & Petrovic, J. 2003, in IAU Symposium 212, 275

Langer, N., Yoon, S.-C., & Petrovic, J. 2004, in IAU Symposium 215, in press

Lloyd-Ronning, N. M., Fryer, C. L., & Ramirez-Ruiz, E. 2002, ApJ, 574, 554

Lubow, S. H. & Shu, F. H. 1975, ApJ, 198, 383

MacFadyen, A. I. & Woosley, S. E. 1999, ApJ, 524, 262

MacFadyen, A. I., Woosley, S. E., & Heger, A. 2001, ApJ, 550, 410

Maeder, A. & Conti, P. S. 1994, ARA&A, 32, 227

Maeder, A. & Meynet, G. 2003, A&A, 411, 543

Massey, P. 1981, ApJ, 244, 157

Massey, P., DeGioia-Eastwood, K., & Waterhouse, E. 2001, AJ, 121, 1050

Massey, P. & Grove, K. 1989, ApJ, 344, 870

Meyer, F. & Meyer-Hofmeister, E. 1983, A&A, 121, 29

Meynet, G. & Maeder, A. 1997, A&A, 321, 465

—. 2000, A&A, 361, 101

—. 2003, A&A, 404, 975

Moffat, A. F. J. & Marchenko, S. V. 1996, A&A, 305, L29+

Mowlavi, N., Schaerer, D., Meynet, G., et al. 1998, A&AS, 128, 471

Niemela, V. S. & Moffat, A. F. J. 1982, ApJ, 259, 213

Nieuwenhuijzen, H. & de Jager, C. 1990, A&A, 231, 134

Noels, A. & Grevesse, N. 1993, in ASP Conf. Ser. 40: IAU Colloq. 137: Inside the Stars, 410

Nugis, T. & Lamers, H. J. G. L. M. 2000, A&A, 360, 227

—. 2002, A&A, 389, 162

Owocki, S. P., Cranmer, S. R., & Blondin, J. M. 1994, ApJ, 424, 887

Owocki, S. P., Cranmer, S. R., & Gayley, K. G. 1996, ApJ, 472, L115+

Packet, W. 1981, A&A, 102, 17

Paczyński, B. 1967, Acta Astronomica, 17, 355

—. 1971, ARA&A, 9, 183

Paczynski, B. 1991, ApJ, 370, 597

Panov, K. P. & Seggewiss, W. 1990, A&A, 227, 117

Penny, L. R., Gies, D. R., Wise, J. H., Stickland, D. J., & Lloyd, C. 2002, ApJ, 575, 1050

Petrenz, P. & Puls, J. 2000, A&A, 358, 956

Petrovic, J. & Langer, N. 2003, in IAU Symposium, 418–+

Petrovic, J. & Langer, N. 2004, in IAUC Colloq. 194, in press

Petrovic, J., Langer, N., & vanderHucht, K. 2004a, AA

Petrovic, J., Langer, N., Yoon, S.-C., & A., H. 2004b, A&A, in prep.

Podsiadlowski, P., Joss, P. C., & Hsu, J. J. L. 1992, ApJ, 391, 246

Pols, O. R., Tout, C. A., Eggleton, P. P., & Han, Z. 1995, MNRAS, 274, 964

Refsdal, S. & Weigert, A. 1969, A&A, 1, 167

Ritter, H. 1988, A&A, 202, 93

Schaerer, D., Charbonnel, C., Meynet, G., Maeder, A., & Schaller, G. 1993, A&AS, 102, 339

Schaerer, D. & Maeder, A. 1992, A&A, 263, 129

Schulte-Ladbeck, R. E. 1989, AJ, 97, 1471

Smith, L. F., Shara, M. M., & Moffat, A. F. J. 1996, MNRAS, 281, 163

Spruit, H. C. 2002, A&A, 381, 923

Spruit, H. C. & Phinney, E. S. 1998, Nature, 393, 139

Stone, J. M. & Norman, M. L. 1992, ApJS, 80, 753

Stothers, R. B. & Chin, C. 1999, ApJ, 522, 960

Taam, R. E. & Sandquist, E. L. 2000, ARA&A, 38, 113

Underhill, A. B., Yang, S., & Hill, G. M. 1988, PASP, 100, 1256

van den Heuvel, E. P. J. & Heise, J. 1972, Nature Physical Science, 239, 67

van der Hucht, K. A. 2001, New Astronomy Review, 45, 135

van Kerkwijk, M. H., Geballe, T. R., King, D. L., van der Klis, M., & van Paradijs, J. 1996, A&A, 314, 521

van Marle, A.-J., Langer, N., & Garcia-Segura, G. 2004, A&A, in prep.

Vanbeveren, D. 1982, A&A, 105, 260

—. 1991, A&A, 252, 159

Vanbeveren, D. 1996, in NATO ASIC Proc. 477: Evolutionary Processes in Binary Stars, 155–+

Vanbeveren, D. & Conti, P. S. 1980, A&A, 88, 230

Vanbeveren, D., de Greve, J. P., de Loore, C., & van Dessel, E. L. 1979, A&A, 73, 19

Vanbeveren, D., de Loore, C., & van Rensbergen, W. 1998, A&A Rev., 9, 63

Wellstein, S. 2001, Ph.D. Thesis

Wellstein, S. & Langer, N. 1999, A&A, 350, 148

Wellstein, S., Langer, N., & Braun, H. 2001, A&A, 369, 939

Woosley, S. E. Heger, A. 2004, in IAU Symposium 215, in press

Woosley, S. E. 1993a, Bulletin of the American Astronomical Society, 25, 894

—. 1993b, ApJ, 405, 273

Woosley, S. E., Langer, N., & Weaver, T. A. 1993, ApJ, 411, 823

—. 1995, ApJ, 448, 315

Yoon, S.-C. & Langer, N. 2004a, A&A, 419, 645

—. 2004b, A&A, 419, 623

Zahn, J.-P. 1977, A&A, 57, 383

Dankwoord

First, I want to thank to my parents for all the support and love they gave me. I know it was very hard for them when I left Serbia, but still they have found the strength to understand my decision and also to support me in other changes I have made in that phase of my life. Mama i tata, hvala za svu ljubav i razumevanje za sve moje odluke!

I also want to mention here Mena i deda Mile, because they are such a special loving grandparents.

I want to thank to Faculty of Mathematics and Department of Astronomy in Belgrade for making me go through so many very difficult exams after which PhD didn't seem too complicated to do. Many thanks to my master thesis supervisor Trajko Angelov for introducing me into problems of stellar structure and evolution.

I also want to express my gratitude to Norbert Langer for his supervisions and many useful discussions and comments on my work. Thanks to Onno Pols for his comments and suggestions as well as for being a friend in some tough moments.

Sterrenkundig Instituut in Utrecht was a great place to work and I spent there beautiful years for which I have to thank to all my colleagues.

And, most of all, I want to thank my husband Thijs for everything: all the love, support, understanding and strength he gave me.
Love, I could have never done this without you!

Curriculum Vitae

I was born on 24 March 1974 in Priština, Serbia, at that time a part of Socialistic Federal Republic of Yugoslavia. After graduating from gymnasium 'Uroš Predić in Pančevo in 1992 I started studying on the Department of Astronomy, Faculty of Mathematics on Belgrade University in a new smaller country called Federal Republic of Yugoslavia. I graduated astrophysics May 7th 1998 and after that I started working as a teaching assistant on the Department of astronomy in Belgrade. Somewhere at the same time, in the beginning of 1999, Serbia was bombed for three whole months without a single hour of break and I was busy starting with my master thesis: 'Influence of stellar rotation on zero-age main sequence stars', which was completed June 11th 2001. Meanwhile, in April 2000, I applied for a PhD position in Utrecht and I was accepted. I arrived to The Netherlands in October 2000 and started to work on a PhD thesis 'Evolution of a massive close binary systems'. My work in last four years is presented in this thesis and should be closed with the promotion on 27th October 2004. Meanwhile my birth country have gotten a new name: Serbia and Montenegro, and my birthtown Priština became a place I can no longer visit.